Analysis of atmospheric observations

Hoogervorst, F.T.M.

Award date:
1993

EINDHOVEN UNIVERSITY OF TECHNOLOGY

FACULTY OF ELECTRICAL ENGINEERING

TELECOMMUNICATIONS DIVISION

Analysis of atmospheric observations

by

F.T.M. Hoogervorst

Report of graduation work,
performed from March 1993 to December 1993.

Supervisors: Prof. dr. ir. G. Brussaard
Ir. J. Dijk

Abstract

Signals on an earth-satellite link are subject to attenuation due to atmospheric constituents. The three constituents of importance are oxygen, water vapour and liquid water. The densities of last two are time variant and of interest to measure.

With a radiometer, brightness noise temperatures of the atmosphere were measured at two frequencies. The three above mentioned constituents are input parameters of a propagation model with which brightness temperature and attenuation can be computed. Hence, with an inversion algorithm it is possible to determine the atmospheric quantities integrated water vapour (*IWV*) and liquid water content (*LWC*). Three of such inversion algorithms were examined. To correct for radiometer inaccuracies, correction factors were derived for the measured brightness temperatures. One of those algorithms showed most consistent results for both summer and winter season. This algorithm was based on inversion of an attenuation model. The two others were based on an inversion of brightness temperature and opacity, respectively.

Not only the radiometer introduces inaccuracies, also the propagation models used to derive the inversion algorithms are not perfect. The effect of cloud temperature is an important cause of uncertainty. Also the antenna pattern limitations have a significant effect.

To investigate further the accuracy of model inversion for the determination of *LWC*, a cloud observation setup was used. By comparing recordings of the atmosphere, made with a video camera, and the *LWC* obtained from the radiometric observations, it should be possible to check the performance of the algorithm. A limited number of simultaneous observations of clouds by camera and radiometer were made. In most cases no correlation was visible between the camera observations and the *LWC* derived from the radiometer measurements. This is mainly due to the fact that there is a low liquid water density at the edges of most clouds. If an increase in *LWC* is noticed, then in most cases the cloud is already covering the camera view and radiometer antenna beams for some time, resulting in a plain grey image.

The video recordings were digitized with a Video Blaster capture board and stored on the harddisk of a PC. Limitations of both hard- and software of the video-capturing system influence the quality of the captured video. The quality depends on the contrast and the number of colours in the recorded images of the sky view. Further, the digitizing of the video is time and harddisk-space consuming. With an additional computer program it is possible to overlay the digitized image with an image defining the radiometer antenna beams.

Despite of negative initial results, more observations should take place. Only then a reliable conclusion can be made about the potential of a comparison of video observations with liquid water content observations derived from radiometer measurements.

Acknowledgements

First of all, I would like to thank Professor Brussaard and Ir. Dijk for supervising and supporting my graduation work. Also thanks to the staff members of EC for their cooperation.
But no results are reached without the many coffee-breaks with the folks of floor 11, during which inspiring nonsense conversations were a great moral support. Last but not least, I owe Caecilia a great debt to have patience with me as being my roommate at EC.

The following poem was a moral support during the times I spent observing the atmosphere:

Clouds are pictures in the sky
They stir the soul, they please the eye
They bless the thirsty earth with rain,
which nurtures life from cell to brain -
But no! They're demons, dark and dire,
hurling hail, wind, flood, and fire
killing, scarring, cruel masters
Of destruction and disasters
Clouds have such diverstiy -
Now blessed, now cursed,
the best, the worst
But where would life without them be?

Vollie Cotton[1)]

1) From: Cotton, R.C. and R.A. Anthes, *Storm and cloud dynamics*. San Diego: Academic Press, 1989, International Geophysics series: 44.

Contents

List of symbols and abbreviations

Symbols

a_i	coefficient for attenuation calculation due to water vapour of frequency channel i
a_L	retrieval coefficient for liquid water of 20 [GHz] channel
a_{L1},a_{L2},a_{L3}	retrieval coefficients for liquid water out of brightness temperature, resp. of 20 [GHz], 30 [GHz] and a constant
a_{V1},a_{V2},a_{V3}	retrieval coefficients for water vapour out of brightness temperature, resp. of 20 [GHz], 30 [GHz] and a constant
a_w	specific weight of water
A_i	atmospheric attenuation of frequency channel i
A_i^*	corrected attenuation when applying ΔT of frequency channel i
b_i	coefficient for attenuation calculation due to liquid water of frequency channel i
b_L	retrieval coefficient for liquid water of 30 [GHz] channel
c	coefficient relating ΔT_{20} and ΔT_{30}
c_i	coefficient for attenuation calculation a constant of frequency channel i
c_L	retrieval coefficient for liquid water, a constant
c_L^*	corrected c_L when applying ΔT
d	distance, coefficient relating ΔT_{20} and ΔT_{30},
d_{liq}	liquid water density
$e(h)$	partial water vapour pressure at height h
E	dry air entrainment factor
f	frequency
h	antenna pattern factor, height of grid, height above the ground
h_b,h_{base}	height of base of cloud above ground
h_t,h_{top}	height of top of cloud above ground
h_i	antenna pattern factor of frequency channel i
h_{sc}	water vapour scaling height
H_i	altitude of i^{th} layer
i	index referring to a frequency channel, general index
IWV	integrated water vapour
IWV_{est}	estimated integrated water vapour
IWV_{inv}	retrieved integrated water vapour
k	radiometer scaling factor
l	radiometer scaling factor
$l(h)$	liquid water density at height h
L_i	temperature gradient of i^{th} layer
LWC	liquid water content
LWC_{est}	estimated liquid water content
P_i	pressure of i^{th} layer
P_o	pressure at ground level
s	spatial coordinate
T_{20},T_{30}	brightness temperature of 20 [GHz], 30 [GHz] channel

$T(s)$	atmospheric temperature at spatial coordinate s
T_{ant}	antenna noise temperature
$T_b(s)$	brightness temperature at spatial coordinate s
T_{bi}	brightness temperature of frequency channel i
T_b^{ext}	brightness temperature due to extraterrestrial sources
$T_{bg,i}$	cosmic background radiation of frequency channel i
T_{eff}	effective temperature
T_g, T_o	surface/ground temperature
T_i	temperature of i^{th} layer
v_o	water vapour density at ground level
$v(h)$	water vapour density at height h
V_{out}	radiometer output voltage
w	width of grid
W_{cloud}	saturating mixing ratio
$\alpha(f)$	retrieval coefficient for opacity due to water vapour of frequency f
$\alpha(s)$	absorption coefficient at spatial coordinate s
α_{IWV}	integrated water vapour absorption coefficient
α_{LWC}	liquid water absorption coefficient
α_{O2}	oxygen absorption coefficient
α_L, α_V	retrieval coefficient for liquid water, water vapour due to opacity for frequency 1
$\beta(f)$	retrieval coefficient for opacity due to liquid water of frequency f
β_L, β_V	retrieval coefficient for liquid water, water vapour due to opacity for frequency 2
$\gamma(f)$	retrieval coefficient for opacity a constant of frequency f
γ_L, γ_V	retrieval coefficient for liquid water, water vapour due to opacity a constant
ΔLWC	correction for LWC when applying ΔT
$\Delta T, \Delta T_i$	correction factor for measured brightness temperature, of frequency channel i
ΔT_{ave}	correction factor for measured brightness temperature averaged for multiple events
θ_{3dB}	3dB antenna beam width
$\theta_{c,h}$, $\theta_{c,v}$	respectively horizontal and vertical camera lens beam width angles
θ_e	elevation angle
ρ_0 , ρ_{top}	water vapour density at ground level, at top of cloud
σ	standard deviation
τ, τ_s	opacity/ optical depth at infinity, at spatial coordinate s
$\tau^*(f)$	corrected opacity when applying ΔT of frequency f

Abbreviations

AVI	Audio Video Interleave (video file format)
CCIR	International Radio Consultative Committee
DAPPER	Data Analysis and Preprocessing for Propagation Effects Research
EUT	Eindhoven University of Technology
GMT	Greenwich Mean Time
HPGL	Hewlett Packard Graphics Language
KNMI	Royal Netherlands Meteorological Institute
MPM	Millimeterwave Propagation Model
NCAR	National Center for Atmospheric Research
WMO	World Meteorological Organization

Chapter one
Introduction

Signals in space communication are subject to propagation effects like attenuation and delay. These effects are dependent on the atmospheric composition. For the observed frequencies, the 20 [GHz] and 30 [GHz] channels, oxygen, water vapour and liquid water are the main components. If these three quantities are known, prediction of attenuation in earth-satellite links is possible. Hence, power control can be performed more efficient.

Of the three atmospheric components oxygen is the simplest one. For a given frequency its influence is rather constant, independent of the weather. The two others however, are changing by time and weather circumstances, so continuous determination is required.

There are several methods to measure water vapour. Just using ground meteorological data is possible, but suffers from the fact that it has rather low correlation between local humidity and the integrated water vapour. Radiosonde measurements have poor accuracy and can not be done continuously. Infrared spectral hygrometers do not work when the sun is absent, during night or when clouds cover the sun. A radiometer does not have these disadvantages.

It is difficult to perform accurate measurements of the liquid water content. Radiosondes are not suitable to measure liquid water. A better method is aircraft sounding, but for continuous measurement this is not a practical solution. For these reasons predicting liquid water by means of a radiometer is of great interest.

A radiometer measures the brightness temperature, or sky noise temperature, which is related to the attenuation on the propagation path. There are several inversion algorithms to retrieve both water vapour and liquid water using the brightness temperature or attenuation. The DAPPER algorithm is one of them and [*Franssen*] described the EUT-algorithm and some others. But most of these algorithms suffer from prediction of negative liquid water content. To prove the performance of the algorithms, observation of the sky and acquiring data of the occurrence of clouds may give more information.

In this report a method to verify the performance of a yet to be specified inversion algorithm is presented. Chapter two gives a short review of the EUT inversion algorithm. In chapter three of this report the problem of negative liquid water content will be examined. Chapter four treats some cloud information. Chapters five and six describes observation equipment and experiments.

Chapter two
Inversion algorithms

To understand the following part of this report well it is useful to summarize the theory of inverting radiometric data. Most inversion algorithms rely on the fact that absorption due to water vapour at the propagation path has its maxima around the 22 [GHz] spectral line. As well absorption at 30 [GHz] is more sensitive to liquid water than water vapour. By modelling the radiative transfer it is possible to derive a relation between atmospheric absorption, brightness temperature and the two absorbers of interest, water vapour and liquid water.

Several inversion algorithms have been presented by [*Franssen*] to derive the total integrated water vapour (*IWV*) and the liquid water content (*LWC*) in the atmosphere from measured attenuation or brightness temperatures for a frequency pair. Methods designed by *Gibbins*, *Johansson*, *Battistelli* and a reference algorithm, referred to as EUT-algorithm, were compared. It was not possible to make any conclusions on what algorithm gives the best results, because the presented algorithms were designed to suit special databases. These were based on retrieved data of radiometers operating at different frequency pairs or some empirical database. The frequencies used by the EUT-radiometer are 20 [GHz] and [29.8] GHz. *Gibbins* and the EUT algorithms inverse the attenuation or brightness temperature to both *IWV* and *LWC* in a straight forward manner. These two algorithms were highlighted in [*Franssen*].

Because the EUT algorithm was derived for no special frequency pair much effort was made on this method. Actual radiometric data was used to see how this inversion algorithm performs. Also theoretical data was used to compare the *Gibbins* and EUT inversion methods. This database was produced by using the millimeter wave propagation model 1989 (MPM'89) of [*Liebe*] with the CCIR standard atmosphere.

2.1 Radiative transfer

The radiative transfer equation relating brightness temperature with properties of the atmosphere yields

$$T_b(0) = T_b^{ext} \cdot e^{-\tau_\infty} + \int_0^\infty T(s) \cdot \alpha(s) \cdot e^{-\tau_s} ds \qquad (2.1)$$

assuming a non-scattering atmosphere in local thermodynamic equilibrium. In this equation T_b^{ext} is the contribution to the brightness temperature due to extraterrestrial sources, e.g. cosmic background radiation. $T(s)$ is the atmospheric physical temperature at the spatial coordinate s and

$\alpha(s)$ is the absorption coefficient of the atmosphere. τ_s is the optical depth or opacity at the spatial coordinate s (with the simplified notation $\tau_{(0,\infty)} \rightarrow \tau_\infty$ and $\tau_{(o,s)} \rightarrow \tau_s$) defined as

$$\tau_s = \int_0^s \alpha(s')\, ds' \qquad [Np] \tag{2.2}$$

(τ_s [dB] = 4.343•τ_s [Np]).

The absorption coefficient is built up of water vapour, liquid water and oxygen absorption:

$$\alpha(s) = \alpha_{IWV}(s) + \alpha_{LWC}(s) + \alpha_{O_2}(s) \quad . \tag{2.3}$$

With an effective temperature, also referred to as mean radiation temperature, defined as

$$T_{eff} = \frac{\int_0^\infty T(s)\,\alpha(s)\,e^{-\tau_s} ds}{\int_0^\infty \alpha(s)\,e^{-\tau_s} ds} \qquad [K] \tag{2.4}$$

the radiative transfer (2.1) is written as

$$T_b(s) = T_b^{ext} e^{-\tau_\infty} + T_{eff}(1 - e^{-\tau_\infty}) \qquad [K] \ . \tag{2.5}$$

T_{eff} can be estimated by surface meteorological measurements. Often the meteorological circumstances varying profile $T(s)$ is replaced by a single constant. This is commonly valid for $T_b(0)$ smaller than approximately 200 [K]. Hence, from (2.5) an useful expression for converting T_b to opacity is derived:

$$\tau = 4.343 \cdot \ln\left(\frac{T_{eff} - T_b^{ext}}{T_{eff} - T_b(0)}\right) \qquad [dB] \ . \tag{2.6}$$

With T_{eff} it is possible to convert brightness temperatures to attenuation. It is also used to correct the measured brightness temperatures for cosmic background radiation. Three approximations for the effective medium temperature are used, besides assuming a constant T_{eff}.

First, [*Wu*] used for the 20.0 [GHz] channel the relation between the effective temperature and the surface temperature T_g with a standard deviation of smaller than 3.5 K in T_{eff} yielding

$$T_{eff} = 0.950 \cdot T_g \qquad [K] \ , \tag{2.7}$$

and for the 31.4 [GHz] channel

$$T_{eff} = 0.940 \cdot T_g \qquad [K] \ . \tag{2.8}$$

He showed that a 10 [K] error in T_{eff} only resulted in an error smaller than 1 [K] in the brightness temperature. So regardless of what expression is used no large inaccuracies will be made.

We have used eq. (2.5) on some empirical data computed with MPM'89 to obtain T_{eff}. In our approximation, described in [*Franssen*], a mean value for T_{eff} is derived for an appropriate range of T_g. This is done for both summer and winter period separately:

$$\begin{aligned} \textit{Winter:}\ & Teff(f=20.0GHz) = 262.84 \quad [K] \\ & Teff(f=29.8GHz) = 261.79 \quad [K] \\ \textit{Summer:}\ & Teff(f=20.0GHz) = 270.65 \quad [K] \\ & Teff(f=29.8GHz) = 270.95 \quad [K] \end{aligned} \tag{2.9}$$

Third, *Gibbins* use a linear expression like (2.7). *Gibbins* derived an inversion algorithm for the radiometric frequencies 21.25 and 31.5 [GHz]. With MPM '89 regression analysis to the ground temperature T_g [K] yielded

$$\begin{aligned} T_{eff}(f=21.25GHz) &= -13.82+T_g \quad [K] \\ T_{eff}(f=31.50GHz) &= -14.23+T_g \quad [K] \end{aligned} \tag{2.10}$$

This approach of T_{eff} is somewhat different than in [*Wu*], resulting in an ideal match to T_g with only an offset to the surface temperature. If e.g. T_g=290 [K] the difference in T_{eff} between *Wu* and *Gibbins* yields $|\Delta T_{eff}|$<3 [K].

Correction for cosmic background radiation can be achieved by subtracting

$$T_{bg,i} = 2.7 \cdot e^{-0.230585 \cdot A_i} \tag{2.11}$$

from the brightness temperature. In this formula A_i denotes the atmospheric attenuation [dB] and is calculated utilizing

$$A_i = 10 \log\left(\frac{T_{eff,i} - T_{b,i}(0)}{T_{eff,i} - T_b^{ext}(0)}\right) \quad , \tag{2.12}$$

for both channels separately. $T_{b,i}(0)$ is the brightness temperature at ground level and $T_b^{ext}(0)$ the brightness temperature due to cosmic background radiation at ground level. $T_b^{ext}(0)$ is normally taken as 2.7 [K]. The index i is referring to either frequency 21.25 [GHz] or frequency 31.50 [GHz]. Correction for cosmic background radiation will be done for all radiometric data, although it will be not mentioned throughout this report anymore.

2.2 EUT inversion algorithm

As is clear from eq. (2.1) there is no linear relationship between the integrated water vapour *IWV* and the liquid water content *LWC* on the propagation path and the brightness temperature. But a linear relation is assumed. In this way an inversion algorithm can be derived:

$$IWV = a_V \cdot T_{20} + b_V \cdot T_{30} + c_V \quad [cm]$$
$$LWC = a_L \cdot T_{20} + b_L \cdot T_{30} + c_L \quad [cm] \quad . \tag{2.13}$$

T_{20} is the brightness temperature at 20.0 [GHz], T_{30} the one at 29.8 [GHz]. Fitting both expressions to an empirical database, computed with MPM '89, gives coefficients as in Tables 2.1 and 2.2.

Table 2.1: Coefficients for EUT water vapour inversion algorithm (2.13).

Season	a_V	b_V	c_V
Winter	0.1595	-0.1077	2.2425
Summer	0.2188	-0.1320	1.1360

Table 2.2: Coefficients for EUT liquid water inversion algorithm (2.13).

Season	a_L	b_L	c_L
Winter	$3.59 \cdot 10^{-3}$	$8.98 \cdot 10^{-4}$	-0.1555
Summer	$-1.02 \cdot 10^{-4}$	$3.73 \cdot 10^{-3}$	-0.1414

For 'good' weather conditions, clear sky or clouds covering less than half the sky, [*Elgered*] did similar radiometric observations and inversions at the frequency pair 21.0/31.4 [GHz]. This resulted in

$$IWV = 0.764 \cdot T_{20} - 0.304 \cdot T_{30} - 0.70 \quad [mm] \; . \tag{2.14}$$

[*Guiraud*] uses for the liquid water content at frequencies 20.6/31.6 [GHz] the expression

$$LWC = -1.14 \cdot 10^{-3} \cdot T_{20} + 2.84 \cdot 10^{-3} \cdot T_{30} - 0.0180 \quad [cm] \; . \tag{2.15}$$

If *IWV* of (2.13) using the coefficients of Table 2.1 is compared with (2.14) it is obvious that, as already mentioned, T_{20} is sensitive to water vapour and T_{30} sensitive to liquid water and therefore having a lower magnitude. *Elgered* found a negative value for coefficient c_L of the water vapour, while for the EUT-radiometric data a positive was found. The coefficient of the T_{20} for *LWC* in eq. (2.13) has positive sign, while in (2.15) it is negative. It is larger than the coefficient of T_{30} too. This is rather conspicuous.

Next, actual inversion of radiometric data has to be made to see how the algorithm (2.13) performs.

Chapter three
Inverting EUT-radiometric data

Results of inverting radiometric data from the EUT radiometer by [*Franssen*] appeared to be not correct. The problem of the presented inversion algorithm was that a negative *LWC* occurs for large periods of time.

To examine this problem of negative *LWC*, it is divided in three parts. First, the radiometer can cause deviations due to imperfect calibration. Second, the coefficients of the inversion algorithm may be not correct. And third, the inversion algorithm itself can cause problems. Next these three possibilities will be examined while comparisons with other models will be made.

3.1 Radiometer inaccuracies

3.1.1 EUT-inversion algorithm

To examine the possible influence of radiometer inaccuracies a ΔT is introduced as a radiometer inaccuracy. Because the 30 [GHz] channel is sensitive to liquid water, and this amount should be increased, ΔT is added to this channel. For the 20 [GHz] channel ΔT is subtracted:

$$LWC = a_L \cdot (T_{20} - \Delta T) + b_L \cdot (T_{30} + \Delta T) + c_L \quad , \tag{3.1}$$

with the coefficients a_L, b_L, c_L as given in Table 2.2 Hence, applying a ΔT in the EUT-algorithm is nothing more than using an additional bias shift ΔLWC:

$$\Delta LWC = (b_L - a_L) \cdot \Delta T \quad . \tag{3.2}$$

If appropriate ΔT's for both winter and summer period are found, it is easy to use a 'corrected' coefficient c^*_L in (2.12):

$$c^*_L = c_L + (b_L - a_L) \cdot \Delta T \quad . \tag{3.3}$$

Although Franssen stated that ΔT=5 [K] would be sufficient, it is found that for many occasions this may be not true. Averaging over the examined days of the winter period a ΔT_{ave}= -13.67 [K] is found, with a standard deviation σ= 8.8 [K]. During the summer period it yields 4.98 [K] respectively 4.3 [K].

The sign of ΔT for the winter period is opposite of that what was expected. This is due to the fact that a_L is larger than b_L. Further, for the winter period a larger ΔT is noticed. Both ΔT and the standard deviation σ are double of that of the summer, due to different coefficients for both the winter and summer period.

The algorithm presented by *Franssen* is not the only one. Another important algorithm is that of the DAPPER program. DAPPER (Data Analysis and Preprocessing for Propagation Effects Research) is a standard software tool for OPEX (Olympus Propagation Experiment). Another inversion algorithm was presented by *Lavergnat*. Both algorithms are briefly described in the following paragraphs.

3.1.2 The DAPPER algorithm

The DAPPER program calculates the attenuation [dB] along the propagation path with the following formula:

$$\begin{aligned} A_1 &= a_1 \cdot V + b_1 \cdot L + c_1 \\ A_2 &= a_2 \cdot V + b_2 \cdot L + c_2 \end{aligned} \quad , \tag{3.4}$$

index 1 referring to the 20 [GHz] channel, and index 2 to the 30 [GHz] channel. V [kg/m^2] and L [kg/m^2] are the integrated water vapour and liquid water content along the propagation path. Coefficients a_i, b_i and c_i are given in Table 3.1.

Table 3.1: Coefficients of the DAPPER program at Olympus frequency channels.

i	a_i	b_i	c_i
20 [GHz]	0.012	0.36	0.14
30 [GHz]	0.01	0.82	0.24

From equation (3.4) an inversion algorithm can be derived to retrieve V and L out of A_1 and A_2:

$$\begin{aligned} V &= \left(\frac{b_2}{a_1 b_2 - a_2 b_1}\right) \cdot A_1 - \left(\frac{b_1}{a_1 b_2 - a_2 b_1}\right) \cdot A_2 - \left(\frac{c_1 b_2 - c_2 b_1}{a_1 b_2 - a_2 b_1}\right) \\ L &= \left(\frac{a_2}{a_2 b_1 - a_1 b_2}\right) \cdot A_1 - \left(\frac{a_1}{a_2 b_1 - a_1 b_2}\right) \cdot A_2 - \left(\frac{c_1 a_2 - c_2 a_1}{a_2 b_1 - a_1 b_2}\right) \end{aligned} \quad , \tag{3.5}$$

or with the expressions in the brackets abbreviated

$$\begin{aligned} V &= a_V \cdot A_1 + b_V \cdot A_2 + c_V \\ L &= a_L \cdot A_1 + b_L \cdot A_2 + c_L \end{aligned} \tag{3.6}$$

with the coefficients as in Table 3.2.

Table 3.2: Coefficients for the DAPPER inversion algorithm.

x	a_x	b_x	c_x
V	131.41	-57.69	-4.55
L	-1.60	1.92	-0.24

If the radiometer cause an uncertainty in the measured brightness temperature T_i, than attenuation A_i will have it too. Hence,

$$L + \Delta L = a_L \cdot A_1^* + b_L \cdot A_2^* + c_L \quad \geq 0 \tag{3.7}$$

should be applied, where A_i^* is defined as

$$A_i^* = 10 \cdot \log\left(\frac{T_{eff,i} - T_b^{ext}}{T_{eff,i} - (T_{b,i}(0) \mp \Delta T)} \right) \quad [dB] \quad . \tag{3.8}$$

The minus-sign preceding ΔT in (3.8) is for the 20 [GHz] channel, the plus-sign the 30 [GHz]. With computer analysis the minimum required ΔT for a specified period, e.g. one day or a season, can be determined at which (3.7) applies.

For the winter period an average of ΔT_{ave}= 10.09 [K] (σ=2.10 [K]) occurs, while for the summer period this is ΔT_{ave}= 10.17 [K] (σ=1.44 [K]). Note that these values are the same for both periods. The overall average amounts ΔT_{ave}= 10.12 [K] with an standard deviation σ= 1.84 [K]. This means that for all investigated days a quite similar ΔT can be used. The radiometer does have some calibration error, but a radiometer inaccuracy of 10 [K] is very unlikely. Unlikely too is that the processing software causes a large deviation.

If only for the 30 [GHz] channel a correction with ΔT is made one might expect that ΔT will be the double. For the winter period a ΔT_{ave}= 18.34 [K] is required and for the summer period ΔT_{ave}= 18.69 [K]. Averaging over the whole year yields ΔT_{ave}=18.46 [K] with σ= 3.40 [K]. The increase in both ΔT_{ave} and σ is of the same magnitude.

3.1.3 *Lavergnat*'s algorithm

[*Lavergnat*] uses opacity to retrieve *IWV* and *LWC*. Given the relation between opacity $\tau_{0,\infty}(f)$ and *IWV* and *LWC* for frequency *f*:

$$4.343 \cdot \tau_{0,\infty}(f) = \alpha(f) \cdot IWV + \beta(f) \cdot LWC + \gamma(f) \quad [dB] \quad . \tag{3.9}$$

The inversion algorithm is:

$$\begin{aligned} IWV &= \alpha_V \cdot (4.343 \cdot \tau_{0,\infty}(f_1)) + \beta_V \cdot (4.343 \cdot \tau_{0,\infty}(f_2)) + \gamma_V \quad [kg/m^2] \\ LWC &= \alpha_L \cdot (4.343 \cdot \tau_{0,\infty}(f_1)) + \beta_L \cdot (4.343 \cdot \tau_{0,\infty}(f_2)) + \gamma_L \quad [kg/m^3] \ , \end{aligned} \tag{3.10}$$

where the coefficients α_x , β_x , γ_x (x=V,L) yield

$$\alpha_V = \frac{\beta(f_2)}{\alpha(f_1)\cdot\beta(f_2) - \alpha(f_2)\cdot\beta(f_1)}$$

$$\beta_V = \frac{\beta(f_1)}{\alpha(f_1)\cdot\beta(f_2) - \alpha(f_2)\cdot\beta(f_1)} \qquad (3.11)$$

$$\gamma_V = \frac{\gamma(f_1)\cdot\beta(f_2) - \gamma(f_2)\cdot\beta(f_1)}{\alpha(f_1)\cdot\beta(f_2) - \alpha(f_2)\cdot\beta(f_1)}$$

and

$$\alpha_L = \frac{\alpha(f_2)}{\alpha(f_2)\cdot\beta(f_1) - \alpha(f_1)\cdot\beta(f_2)}$$

$$\beta_L = \frac{\alpha(f_1)}{\alpha(f_2)\cdot\beta(f_1) - \alpha(f_1)\cdot\beta(f_2)} \qquad (3.12)$$

$$\gamma_L = \frac{\gamma(f_1)\cdot\alpha(f_2) - \gamma(f_2)\cdot\alpha(f_1)}{\alpha(f_2)\cdot\beta(f_1) - \alpha(f_1)\cdot\beta(f_2)} \quad .$$

For the Olympus beacon frequencies coefficients $\alpha(f)$, $\beta(f)$ and $\gamma(f)$ are given in Table 3.3.

Table 3.3: Coefficients for Lavergnat's algorithm (3.9).

f	$\alpha(f)$	$\beta(f)$	$\gamma(f)$
19.7 [GHz]	0.0097	0.395	0.102
29.6 [GHz]	0.002	0.848	0.204

And with (3.11) and (3.12) the inversion coefficients are defined (Table 3.4).

Table 3.4: Coefficients for Lavergnat's inversion algorithm (3.10).

α_V	114.05	α_L	-0.269
β_V	53.12	β_L	1.305
γ_V	0.796	γ_L	-0.2387

A similar expression as (3.7) can be derived for *Lavergnat*'s algorithm with

$$\tau^*_{0,\infty}(f) = -\ln\left(\frac{T_{eff,i} - (T_{b,i}(0) \mp \Delta T)}{T_{eff,i} - T_b^{ext}}\right) \quad [Np] \; . \qquad (3.13)$$

So, at the same way as for DAPPER a ΔT is obtained.

It is found that according to *Lavergnat*'s algorithm for the summer period no ΔT is required, *LWC* is for all the examined days positive. Averaging for all days in the winter a ΔT_{ave}= 4.66 [K] is required

with a standard deviation σ= 3.80 [K]. A significantly large standard deviation compared with ΔT_{ave}. It is almost as large as ΔT itself.

Applying ΔT only to the 30 [GHz] channel gives ΔT_{ave}= 4.61 [K] and σ= 4.68 [K]. Now σ even exceeds ΔT. It proves that *Lavergnat*'s inversion algorithm is not consistent.

3.2 Accuracy of the inversion algorithm coefficients

As already mentioned,it seems that the coefficient for the inversion of liquid water are not correct, a_{L1} is larger than a_{L2} for the winter period. Physically this means that the inversion algorithm for the liquid water content is more sensitive to the 20.0 [GHz] channel than the 29.8 [GHz] channel. According to the theory of absorption due to liquid water this can not be true. Next some possible causes will be presented.

3.2.1 Accuracy of absorption model

Most inversion methods use an empirical database of brightness temperatures to determine the coefficients of the algorithm. To compute these brightness temperatures some atmospheric absorption model is used. Like *Franssen* did with the MPM '89 model of *Liebe*.

[*Westwater*, 1990] compared *Liebe*'s MPM model with a model of *Waters* and actual measured brightness temperatures for clear sky conditions at frequencies 20.6 and 31.65 [GHz]. *Waters* model gave more accurate results than the MPM'89 for those frequencies. At 90.0 [GHz] the reverse was noted. For different locations and seasons the MPM model showed a rms-error of maximum 4.16 [K] for the 20.0 [GHz] channel and 1.83 [K] for the 31.65. The brightness temperature was calculated using radiosonde data with height distribution profiles of temperature, pressure and water vapour. The absolute accuracy of the radiometer was estimated to be better than 1 [K] while the radiosonde had precisions of ±0.71 [mbar] in pressure, ±0.84 °C in temperature and ±3.4 °C in dew-point temperature.

But much of these estimations of accuracy depends on the operation of the radiosondes used. Two types of radiosondes were used and differences as large as was shown between the two models were demonstrated. So it can be concluded that MPM'89 does show some inaccuracy. Estimation of the influence of this on the coefficients is difficult to make. But it seems that the propagation model can not cause the large ΔT as used for the three algorithms.

3.2.2 Cloud temperature

In the report of *Franssen* it is stated that is was suggested by *Derr* that a cloud temperature of -12°C should be used. In the article of *Derr*, however, no suggestions for cloud temperatures are made. *Derr* only used a threshold of -12°C between the temperature at the top of the cloud and the mean cloud temperature to determine if moderately thick cirrus was present above the stratus layer or not. On the condition that clouds are present, with high water vapour densities using cloud temperatures of -12°C and 0°C can give deviations of 20 [K] in brightness temperature. So using an appropriate cloud temperature is necessary. However no detailed information of cloud temperatures is present during measurements.

3.2.3 Scale height of water vapour

In the propagation model one of the input parameters is the scale height h_{sc} for the water vapour. this

is a measure for the decay of the water vapour density with increasing height (see eq. (A.7) in Appendix A). Normally h_{sc} variates around 2 [km]. This is the value used to determine the coefficients. If we suppose that it should be 2.2 [km], this will only give a slight decrease in brightness temperature of about maximum 5 [K] for the 20.0 [GHz] channel and 3 [K] for the 29.8 [GHz] channel under clear-sky conditions. Significantly smaller values of < 1 [K] occur if liquid water is present on the propagation path. So it is likely that the scale height is of not great importance.

3.2.4 Temperature gradient

For the temperature profile the CCIR standard atmosphere is used (App. A). To examine the influence of the temperature profile on the brightness temperature, the temperature gradient for 0 to 11 [km] is changed from -6.5 in -5 [K/km]. No significant change in brightness temperature is noticed (< 2 [K]).

Because of best fitting regression between *IWV*, *LWC* and both brightness temperatures to obtain the coefficients of the inversion algorithms, it is impossible to find the extent of the discussed inaccuracies. Different items contribute and are averaged out.

3.3 Inaccuracies in the inversion algorithm

3.3.1 Errors in computer program

A CCIR atmospheric absorption model [CCIR, 1990] was used to compute attenuation and brightness temperature. The contribution of the dry air continuum according to the CCIR-model (eq. (2.40) in the report of *Franssen*) contains a factor 10^{-11}. It was proved by *Franssen* that this should be 10^{-12}, but during further calculations he still used a factor 10^{-11}.

In the inversion algorithm program a time variable and the ground temperature were accidently exchanged resulting in some deviation of the inverted water vapour and liquid water.
Not of influence on the performance of the inversion algorithm in general but annoying is next. If $T_{b1} > T_{eff,1}$ then $(T_{eff,1}-2.7)/(T_{eff,1}-T_{b1})$ becomes negative, hence log((..)/(..)) imaginary. This happens especially on two of the examined days in the summer where brightness temperatures exceed for some times 270 [K]. This kind of datapoints should not be used and has to marked as not valid. As a secondary effect with these high values of measured brightness temperatures the inversion algorithms are not accurate anymore.

Almost at the end of the observation period, as will be treated in chapter six, another error in a computer program was found. In App. A.4, eq. (A.10), in the exponent a factor 240.97 occurs. But in the program a factor 270.97 was used. What the consequence will be for the results is not known yet. Additional analysis should make this clear. But note that it is in the exponent, and therefore it may significant.

3.3.2 Validity range of inversion algorithm

In [*Franssen*] the validation range for the coefficients in Tables 2.1 and 2.2 for equation (2.12) was:

$$\begin{aligned} &\{T_o \mid 0..25\ °C\} \\ &\{v_o \mid 2.5..15\ g/m^3\} \\ &\{P_o \mid 983.25..1043.25\ mbar\} \end{aligned} \tag{3.14}$$

For the summer period the range of T_o may be valid, but this is certainly not true for winter period. In *Eindhoven (NL)* the ground temperature is in the winter often below 0°C. At night it can even be -10°C. A maximum temperature of +20°C will suit for most occasions.

The pressure range covers all values that normally occur in winter and summer at our site.

New validation regions are defined. And instead of using MPM '89 now CCIR '91 is used to be able to compare our results with other Olympus propagation experiments (§3.1.2). Using the CCIR '91 model will not give dramatically different results. Both models are rather the same. Only for high frequencies, $f > 300$ [GHz], large deviations between both models occur [*Franssen*].

Results in *Franssen* allow a maximum relative humidity of 85% and a minimum of 0%. But in practice this low value will never occur. So a minimum of 20% relative humidity is more appropriate.

New ranges are defined for both summer and winter periods separately:

$$\begin{aligned} \textit{Summer:}&\{T_o \mid 5..35\ °C\} \\ &\{v_o \mid 2.5..15\ g/m^3\} \\ &\{P_o \mid 983.25..1043.25\ mbar\} \\ \textit{Winter:}&\{T_o \mid -10..+20\ °C\} \\ &\{v_o \mid 1..15\ g/m^3\} \\ &\{P_o \mid 983.25..1043.25\ mbar\} \end{aligned} \tag{3.15}$$

3.3.3 Effective temperature

For the inversion an effective temperature T_{eff}, or mean radiation temperature, is required (see eq. (2.5)). But the problem is that T_{eff} is not known because it depends on the vertical distributions of the temperature. Most times an estimate is made using the surface temperature ([*Lavergnat*], [*Wu*], [*Westwater* '78]), other times T_{eff} is estimated by applying (2.4) and the data used to determine the coefficients of the inversion algorithms ([*Franssen*]).

To examine the performance of the algorithm using different T_{eff}, a deviation of ±10 [K] is used in our algorithm. For $LWC \leq 1$ [cm] it caused a $\Delta LWC \leq 4.5 \cdot 10^{-4}$ [cm]. So the influence of a not well estimated T_{eff} is negligible.

3.3.4 Antenna pattern factor

To convert antenna noise temperature to brightness temperature the following expression is used:

$$T_b = \frac{T_{ant}}{h} - \left(\frac{1-h}{h}\right) \cdot T_g \quad [K] \quad . \tag{3.16}$$

Where T_b is the brightness temperature, T_{ant} the antenna noise temperature and T_g the ground noise temperature. Eq. (3.16) is of course applied to both channels. It is obvious that if antenna pattern factor h is not well estimated, it will give significant deviation. For the EUT radiometer h is empirically determined. But influences of the antenna surrounding were only partly taken into account. So some surroundings do contribute to the antennas noise temperature. By changing h similar effects are achieved as using a ΔT.

The antenna gain is dependent on frequency. The higher the frequency the smaller θ_{3dB} is, giving a higher antenna gain factor. Decreasing h for the 20 [GHz] channel and increasing h for the 30 [GHz] channel will give encouraging results. Say, h_{20} is decreased from 0.93 to 0.89 and not changing h_{30} results in a decrease of 10 [K] of the 20 [GHz] channel for common values of T_g and T_{ant}. So a part of the problem can be assigned to not well determined antenna factors.

3.4 Applying new coefficients for ΔT

With the new defined validation region (3.15) new coefficients are derived for eq. (2.12) (Tables 3.5 and 3.6).

Table 3.5: New coefficients for water vapour inversion algorithm.

Season	a_V	b_V	c_V
Winter	1.1307e-1	-7.6284e-2	4.5995e-1
Summer	1.1237e-1	-6.3871e-2	-1.0836e-1

Table 3.6: New coefficients for liquid water inversion algorithm.

Season	a_L	b_L	c_L
Winter	-6.1834e-4	1.8090e-3	-7.2460e-2
Summer	-1.1360e-3	2.3181e-3	-6.8640e-2

When these coefficients are used to determine ΔT with eq. (3.1), an average of 25.97 [K] is found for the winter period with an standard deviation of 4.36 [K]. While for the summer an average of 14.77 [K] is found with an standard deviation of 2.22 [K]. If only the 30 [GHz] is adjusted with ΔT an average of 34.85 [K] with standard deviation 5.85 [K] is found. And for the summer period 22.01 [K] respectively 3.31 [K].

There is a significantly larger ΔT required than with the old coefficients, but the standard deviation is much smaller. It is remarkable that with coefficients optimized for the season of the year, a higher ΔT is found. We expected that the opposite would happen.

But one has to be in mind that even with the best optimized coefficients still large deviations occur. During the determination of the coefficients assumptions are made for the temperature and water

vapour profiles, which are in practice different and not known. Other influences were already discussed in §3.2.

3.5 Second method of determining ΔT

The method of determining ΔT described in the previous paragraphs dealt with only the liquid water inversion algorithm. However, more information can be obtained by including the water vapour inversion algorithm. Because of the poor (not consistent) results of *Lavergnat*'s algorithm, this one was skipped in further research.

First, as before, for a certain period, a day, the minimum in the inverted LWC , LWC_{min} with the accompanying brightness temperatures ($T_{20,min}$ and $T_{30,min}$) and attenuation are determined. Now, for each observed day the minimum required ΔT_{20} and ΔT_{30} are obtained to satisfy

EUT-algorithm:

$$LWC_{\min} = a_L \cdot (T_{20} + \Delta T_{20}) + b_L \cdot (T_{30} + \Delta T_{30}) + c_L \geq 0 \qquad \textbf{(3.17)}$$

DAPPER-algorithm:

$$LWC_{\min} = a_L \cdot (A_{20} + \Delta A_{20}) + b_L \cdot (A_{30} + \Delta A_{30}) + c_L \geq 0$$

This is done by varying ΔT_{20} and solving eq. (3.17), for the EUT- respectively the DAPPER inversion algorithms, for ΔT_{30} . Afterall, with LWC_{min} , $T_{20,min}$ and $T_{30,min}$ determined the only two remaining variables are ΔT_{20} and ΔT_{30} . If ΔT_{30} is plotted versus ΔT_{20} the curve is a straight line, see Figures 3.1 and 3.2 where in a plot ΔT_{30} versus ΔT_{20} for several days are drawn. For the DAPPER algorithm this is what might be expected regarding the linear relation (3.4). Because it was assumed that the relation between brightness temperature and liquid water is linear eq. (3.17) and hence the relation between ΔT_{20} and ΔT_{30} is linear aswell.

A relation of the form

$$\Delta T_{30} = c \cdot \Delta T_{20} + d \qquad \textbf{(3.18)}$$

can be obtained from the plots. For both seasons, winter and summer, this is done for both our own EUT-algorithm as the DAPPER algorithm, see Appendix C. for an overview of all days. For determining a final result, c and d are averaged per season. Coefficient c is almost always constant, while coefficient d is variating (Table 3.7). As a result $T_{20,min}$ and $T_{30,min}$ are averaged too (Table 3.8). The median rather than the mean is taken best, so outliers are of less influence.

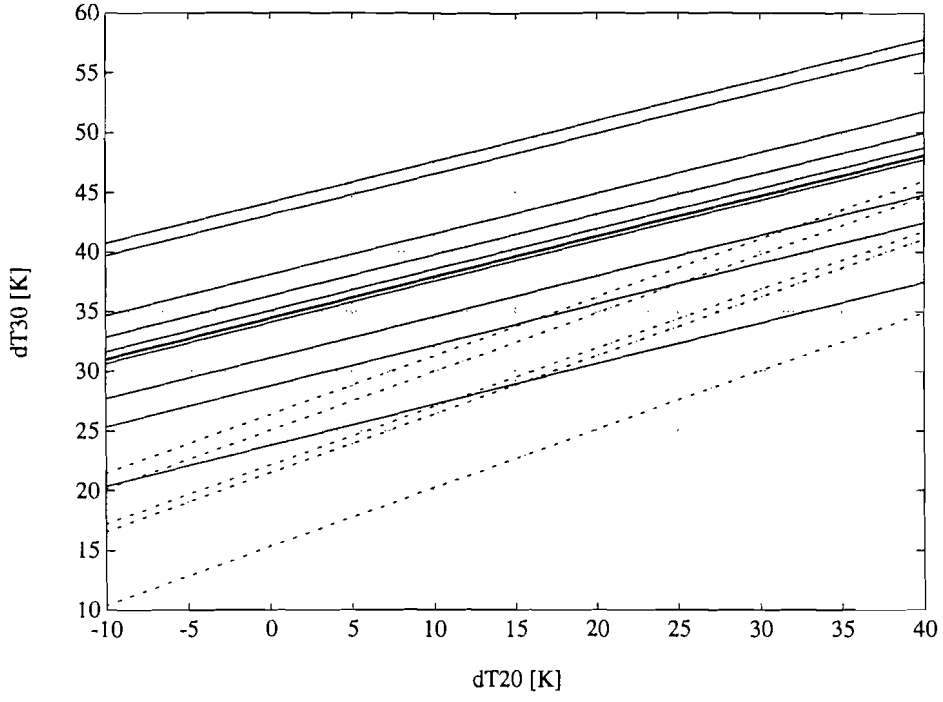

Figure 3.1: ΔT_{30} versus ΔT_{20} for EUT algorithm (solid: winter; dashed: summer).

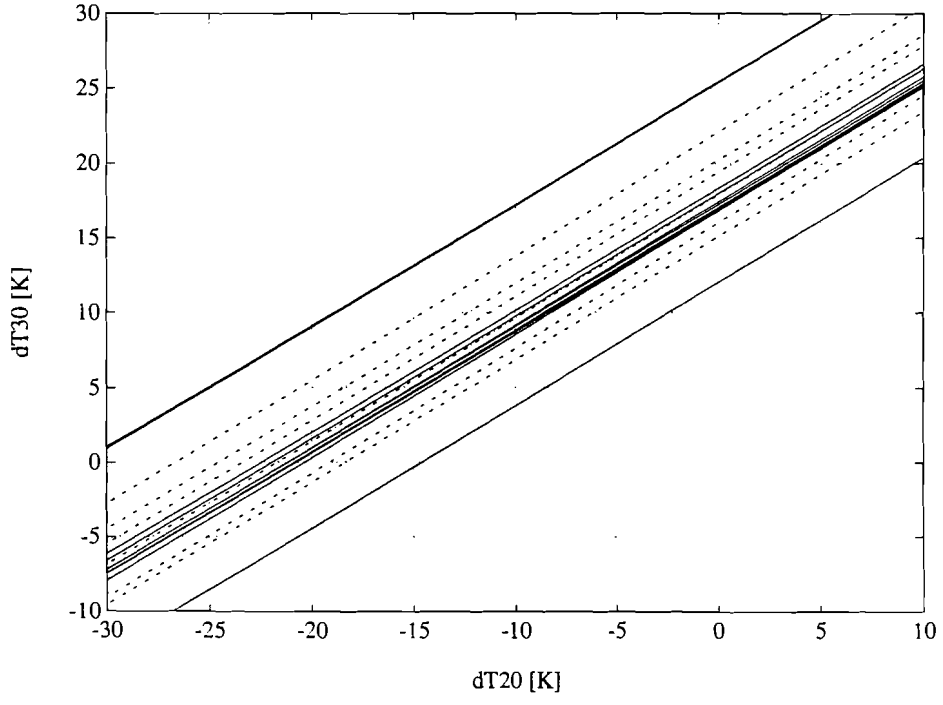

Figure 3.2: ΔT_{20} versus ΔT_{30} for DAPPER algorithm (solid: winter; dashed: summer).

Table 3.7: Statistics of coefficients c and d for EUT- and DAPPER algorithm.

EUT				
	Winter		Summer	
$(i=c,d)$	c	d	c	d
$\tilde{\imath}_{50}$	0.3418	34.4928	0.4901	21.8076
$\tilde{\imath}_{10}$	0.3418	24.2755	0.4901	15.3102
$\tilde{\imath}_{90}$	0.3418	42.5985	0.4901	26.3716
$\bar{\imath}$	0.3418	34.8464	0.4901	21.9684
σ_i	0.0000	5.8464	0.0000	3.8385
DAPPER				
	Winter		Summer	
$(i=c,d)$	c	d	c	d
$\tilde{\imath}_{50}$	0.8182	17.2832	0.8300	18.9631
$\tilde{\imath}_{10}$	0.8141	12.5357	0.8241	15.1196
$\tilde{\imath}_{90}$	0.8246	24.6887	0.8398	22.1156
$\bar{\imath}$	0.8199	18.3491	0.8304	18.4876
σ_i	0.0042	3.8672	0.0056	2.6339

For the EUT-algorithm c and d differ for both seasons, but for the DAPPER algorithm the winter and summer coefficients are almost the same.

Table 3.8: Statistics of $T_{20,min}$ and $T_{30,min}$.

		EUT		DAPPER	
	$i=T_{20},T_{30}$	T_{20} [K]	T_{30} [K]	T_{20} [K]	T_{30} [K]
Winter	$\tilde{\imath}_{50}$	31.55	16.11	33.80	17.18
	$\tilde{\imath}_{10}$	23.76	5.17	26.45	7.32
	$\tilde{\imath}_{90}$	36.57	22.60	44.68	31.50
	$\bar{\imath}$	31.09	15.83	36.64	19.32
	σ_i	5.38	7.46	7.24	8.37
Summer	$\tilde{\imath}_{50}$	54.53	32.75	56.33	34.27
	$\tilde{\imath}_{10}$	45.75	25.66	46.33	28.22
	$\tilde{\imath}_{90}$	60.01	43.71	71.79	51.24
	$\bar{\imath}$	53.02	33.62	56.71	36.15
	σ_i	5.92	6.01	9.11	8.12

As an application coefficients as calculated by *Franssen* are used in the DAPPER algorithm. *Franssen* based his calculations for the coefficients for an attenuation-based inversion algorithm on newer atmosphere models (MPM '89) than the one for DAPPER (CCIR '86).

Table 3.9: Coefficients for DAPPER algorithm (3.6) according to Franssen.

	a_V	b_V	c_V
Winter	12.53	-6.18	-0.24
Summer	12.35	-5.80	-0.29

Table 3.10: Coefficients for DAPPER algorithm (3.6) according to Franssen.

	a_L	b_L	c_L
Winter	-0.09	0.14	-0.019
Summer	-0.12	0.18	-0.026

Table 3.11: Statistics of coefficients *c* and *d* for equation (3.16) using *Franssen*'s coefficients.

	Winter		Summer	
(i=c,d)	*c*	*d*	*c*	*d*
$\tilde{i}_{50}$	0.6601	13.2901	0.6790	11.1639
$\tilde{i}_{10}$	0.6522	6.6937	0.6711	6.6168
$\tilde{i}_{90}$	0.6714	20.6194	0.6926	14.6919
$\bar{i}$	0.6617	14.0024	0.6797	11.1146
σ_i	0.0073	4.4453	0.0082	3.0078

To obtain ΔT_{20} and ΔT_{30} , first estimations of *IWV* are made applying eq. (A.7), which can be approximated by

$$IWV_{est} \simeq \frac{0.2 \cdot v_0}{\sin(\theta_e)} \quad [cm] \quad , \tag{3.19}$$

where a correction for elevation angle θ_e is made, where water vapour density v_o is in [g/m^3]. Averaging over all days of a season gives a prospect of *IWV* which is a constant independent of ΔT_{20} , having a certain standard deviation σ_{est}.

For a certain range of ΔT_{20} , with both inversion algorithms *IWV* is determined, using the median brightness temperatures as given in Table 3.8. IWV_{inv} is not a constant, but it is varying as a function of ΔT_{20} . Both IWV_{est} as IWV_{inv} are plotted versus ΔT_{20} . If σ_{est} is not large, it can be stated that the crosspoint of the two curves is the required ΔT_{20} . And hence ΔT_{30} is determined too. And even if σ_{est} is large, still a good estimation of ΔT_{20} can be made. Because of the nature of the measured variables, depending on much parameters, 10%-of-time and 90%-of-time values are obtained too. In Figures 3.3 through 3.8 plots for all three cases are given.

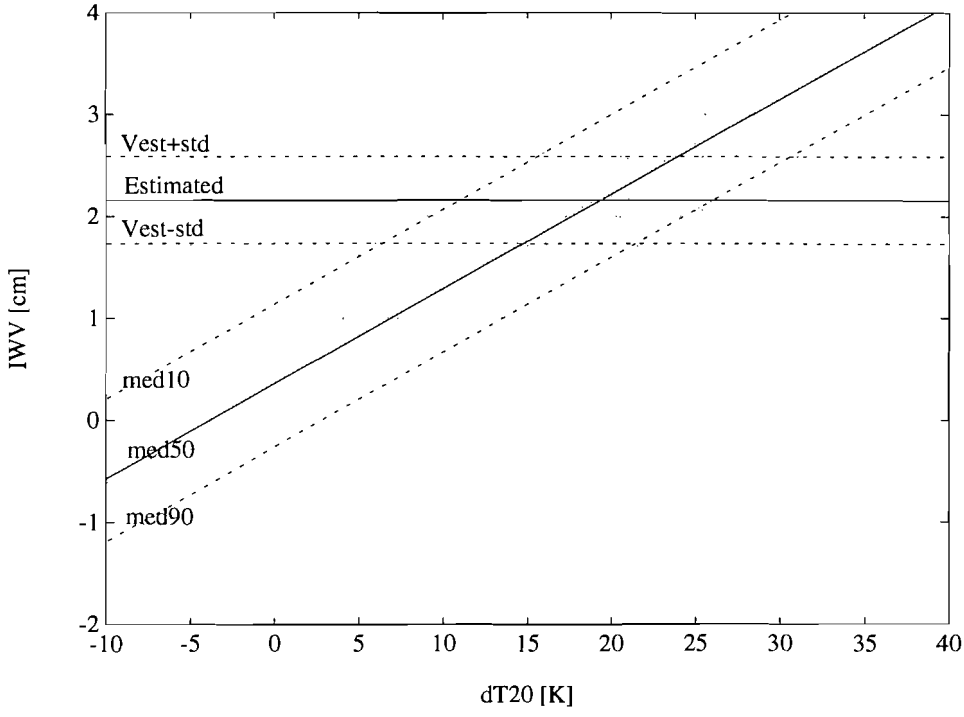

Figure 3.3: *IWV* versus ΔT_{20} for winter period as observed for a number of days, EUT-algorithm

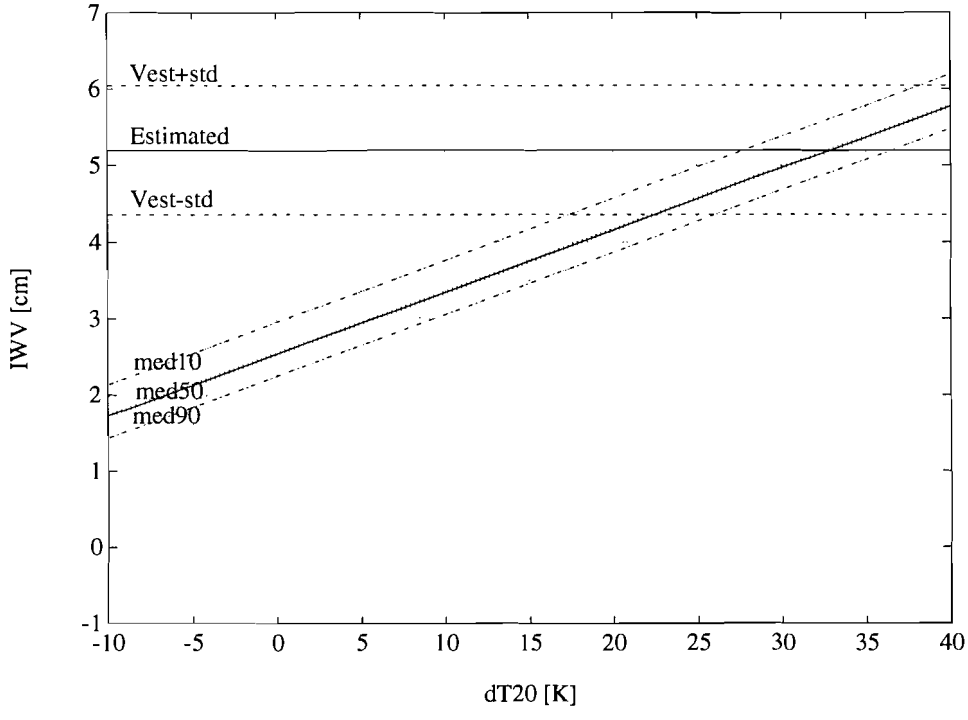

Figure 3.4: *IWV* versus ΔT_{20} for summer period as observed for a number of days, EUT-algorithm.

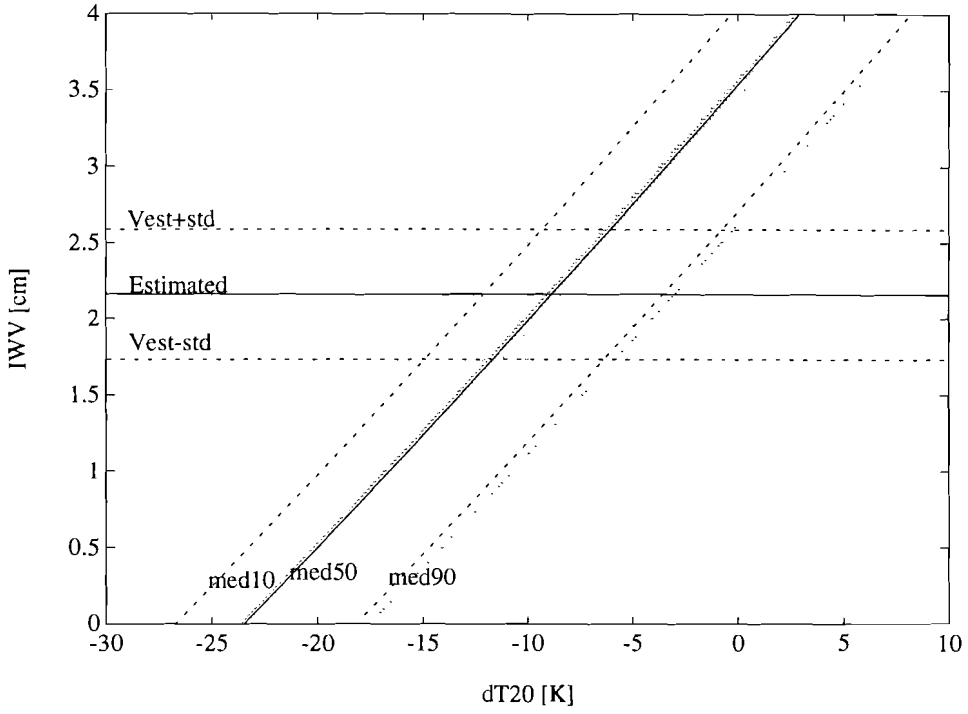

Figure 3.5: *IWV* versus ΔT_{20} for winter period as observed for a number of days, DAPPER algorithm.

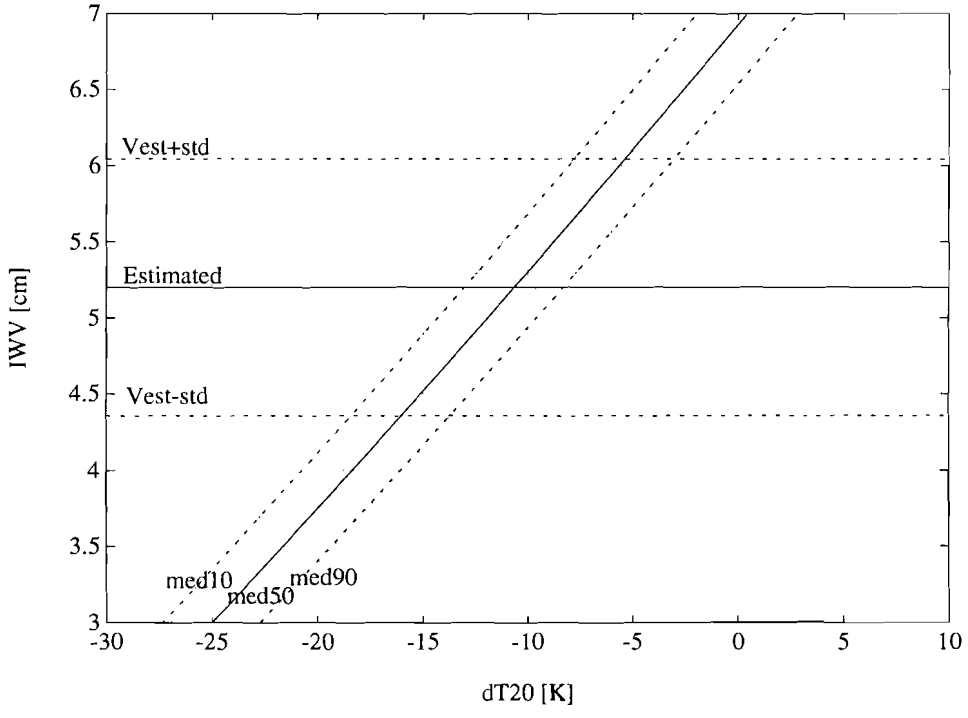

Figure 3.6: *IWV* versus ΔT_{20} for summer period as observed for a number of days, DAPPER algorithm.

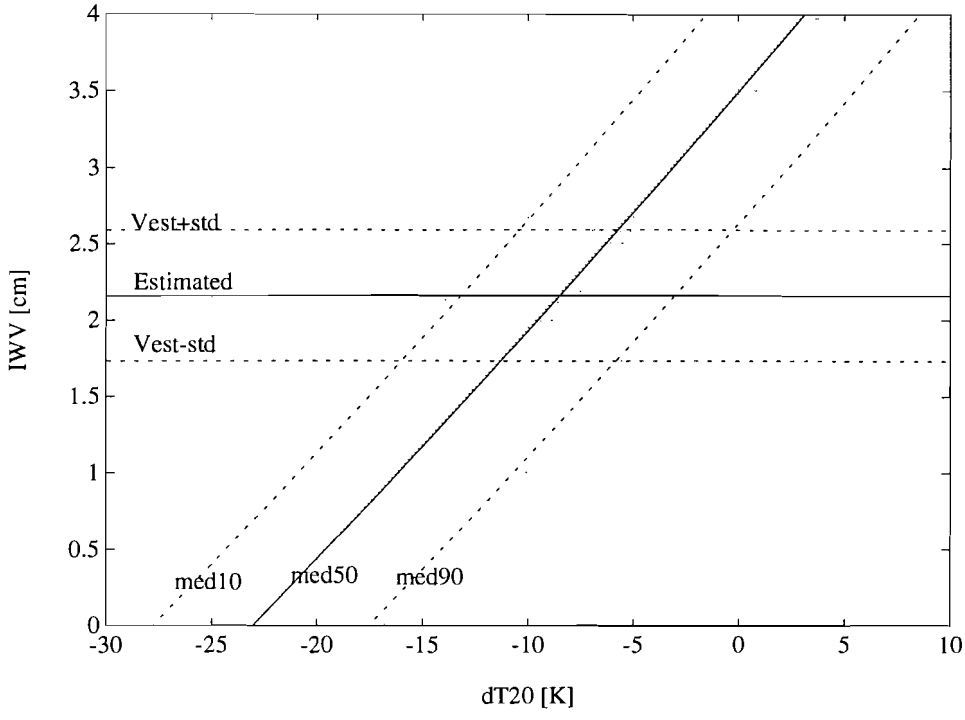

Figure 3.7: *IWV* versus ΔT_{20} for winter as observed for a number of days, DAPPER algorithm with *Franssen*'s coefficients.

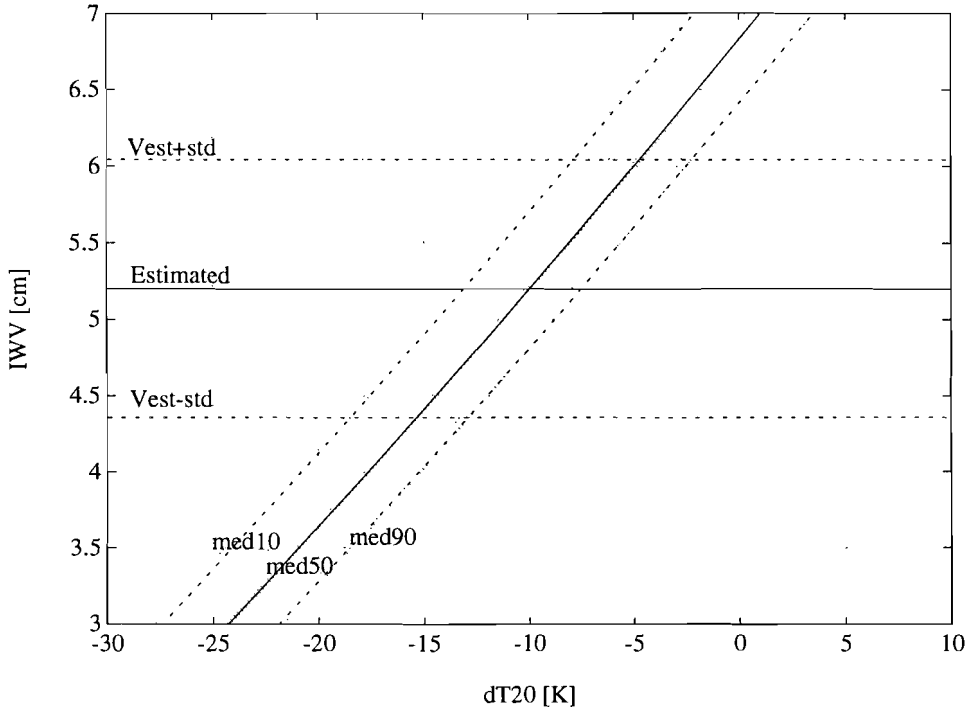

Figure 3.8: *IWV* versus ΔT_{20} for summer period as observed for a number of days, DAPPER algorithm with *Franssen*'s coefficients.

As final result ΔT_{20} and ΔT_{30} as given in Tables 3.12 through 3.14 are found.

Table 3.12: Statistics of ΔT_{20} and ΔT_{30} for EUT-algorithm.

	Winter		Summer	
$i=T_{20}, T_{30}$	ΔT_{20}	ΔT_{30} [1)]	ΔT_{20}	ΔT_{30}
$\tilde{i}_{50}$	19.18	41.05	32.60	37.78
$\tilde{i}_{10}$	10.89	38.21	27.38	35.23
$\tilde{i}_{90}$	25.79	43.31	36.23	39.56
$\bar{i}$	19.51	41.16	32.89	37.93
σ_i	4.81	-	3.02	-

[1)] Calculated using median values of c and d in eq. (3.16).

Table 3.13: Statistics of ΔT_{20} and ΔT_{30} for DAPPER algorithm.

	Winter		Summer	
$i=T_{20}, T_{30}$	ΔT_{20}	ΔT_{30} [1)]	ΔT_{20}	ΔT_{30}
$\tilde{i}_{50}$	-8.97	9.95	-10.76	9.77
$\tilde{i}_{10}$	-12.17	7.32	-13.14	7.79
$\tilde{i}_{90}$	-3.75	14.22	-8.44	11.68
$\bar{i}$	-8.18	10.59	-10.90	9.64
σ_i	2.77	-	1.81	-

[1)] Calculated using median values of c and d in eq. (3.16).

Table 3.14: Statistics of ΔT_{20} and ΔT_{30} for DAPPER algorithm with *Franssen*'s coefficients.

	Winter		Summer	
$i=T_{20}, T_{30}$	ΔT_{20}	ΔT_{30} [1)]	ΔT_{20}	ΔT_{30}
$\tilde{i}_{50}$	-8.59	7.62	-10.01	4.37
$\tilde{i}_{10}$	-13.36	4.47	-13.21	2.19
$\tilde{i}_{90}$	-3.15	11.21	-7.63	5.99
$\bar{i}$	-8.09	18.63	-10.14	4.28
σ_i	3.34	-	2.17	-

[1)] Calculated using median values of c and d in eq. (3.16).

Comparing DAPPER and *Franssen* makes clear that there is no large difference in ΔT_{20} and ΔT_{30} using one of both coefficients. The median and the mean as well as the 10%- and 90%-of-time values are quite the same for ΔT_{20}. For ΔT_{30} the 10%- and 90%-of-time values differ, in advantage of *Franssen*'s. The EUT-algorithm however is an other case. Only for a positive ΔT_{20} IWV_{inv} and IWV_{est} are of the same magnitude. Hence ΔT_{30} is large. The interval between the 10%- and 90%-of-time is larger too

with respect to the other two. So the EUT-algorithm does not give a consistent result which can be used as a correction for radiometer error. The DAPPER algorithm does, regardless of which coefficients are used.

If the radiometer data is inverted to obtain *LWC* and *IWV*, while applying the correction with median values of ΔT_i (i=20,30) at both channels, diagrams as in Figures 3.9 through 3.14 are found. The *LWC* is now more in line with the expectations and physics. As an secondary effect, IWV_{inv} is more in line with the estimated *IWV* based on ground meteorological data. This might be expected by including an optimization for water vapour to obtain ΔT_{20} and ΔT_{30} . But remember that this was done with average values of *IWV* over the whole season. So like in Figure 3.12, for individual events deviations may occur.

As shown by Figure 3.12, still negative *LWC* may be noticed, but these amounts are small. And only for short time periods this occurs. Inaccuracies as discussed in §3.3 are to blame for it.

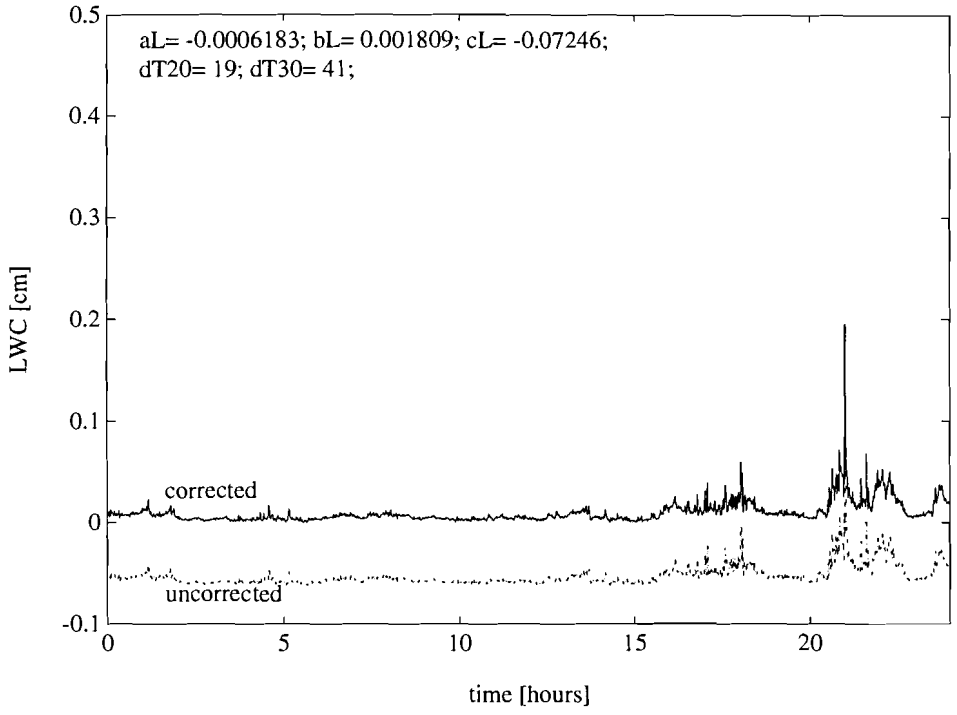

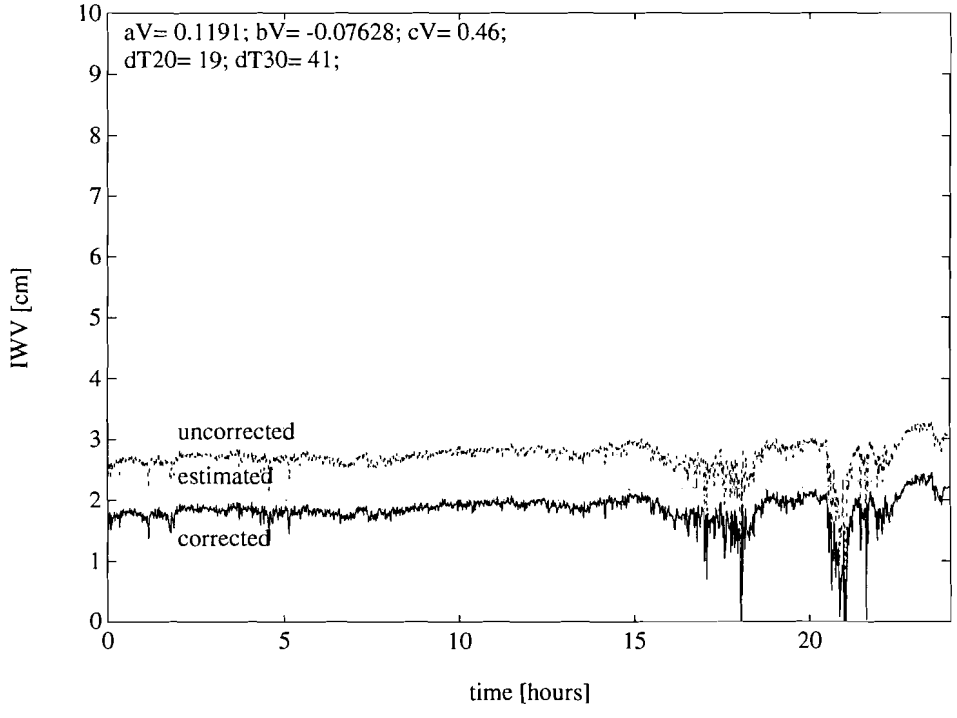

Figure 3.9: *LWC* (top) and *IWV* (bottom) for January 03, 1992 with EUT-algorithm.

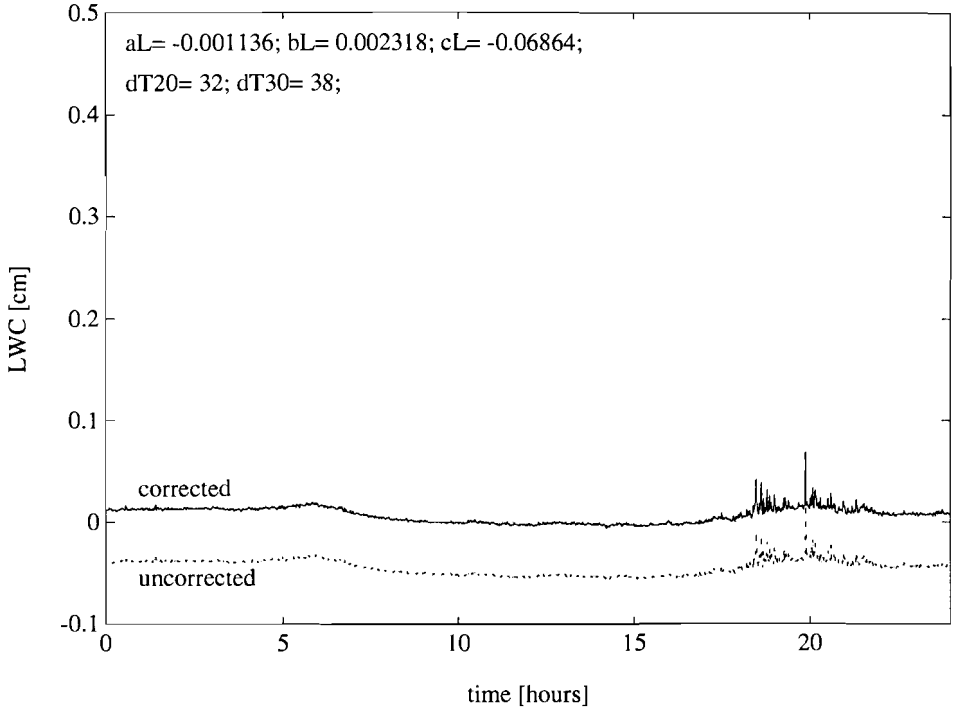

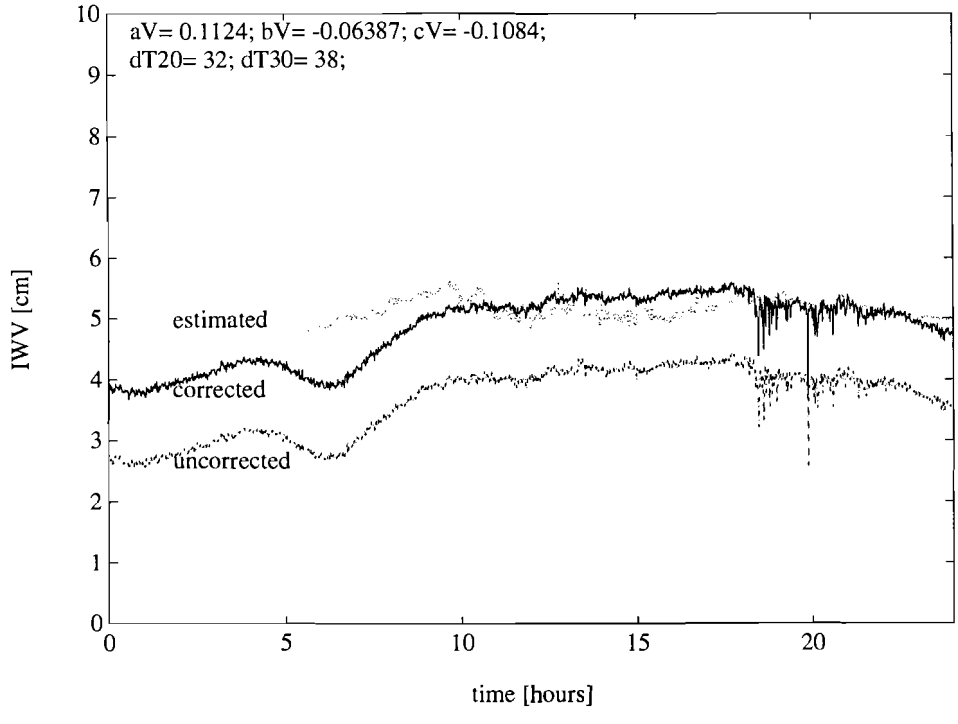

Figure 3.10: *LWC* (top) and *IWV* (bottom) for July 29, 1991 with EUT-algorithm.

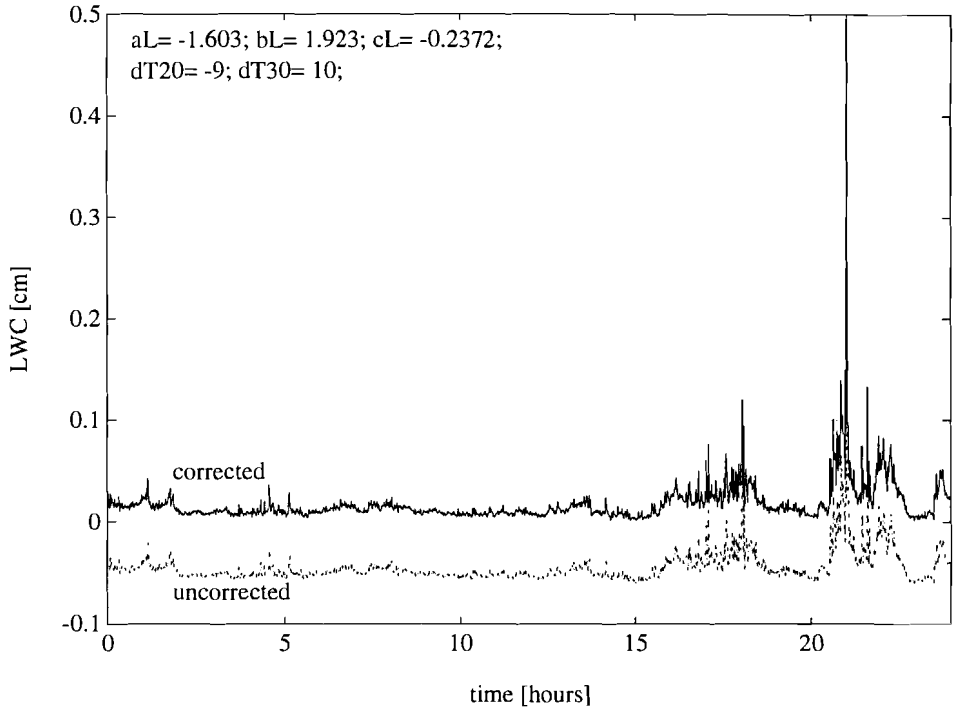

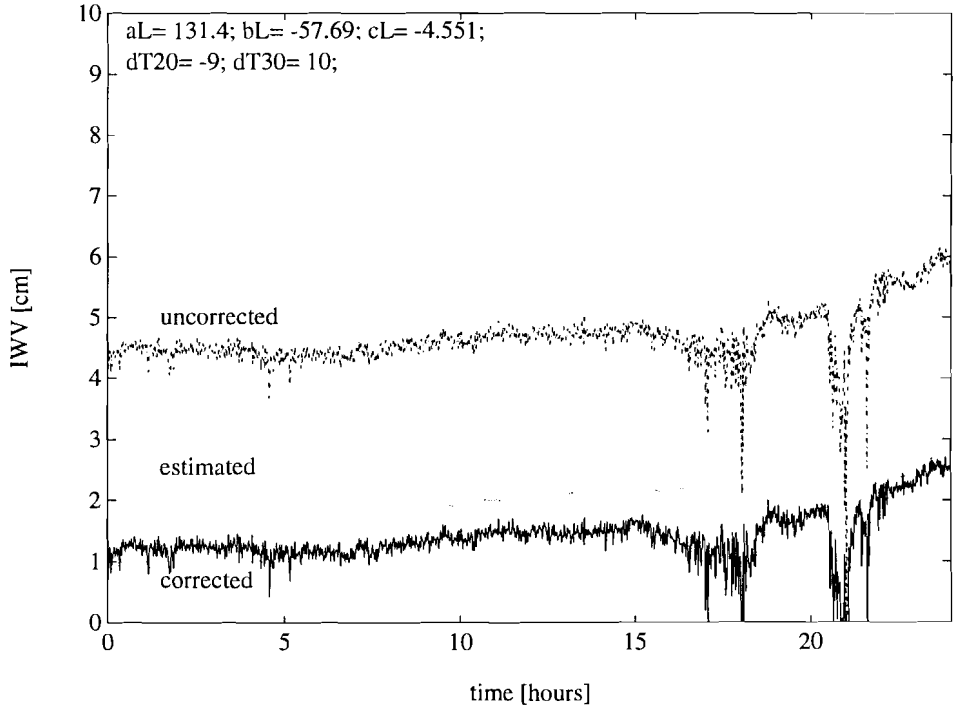

Figure 3.11: *LWC* (top) and *IWV* (bottom) for January 03, 1992 with DAPPER algorithm.

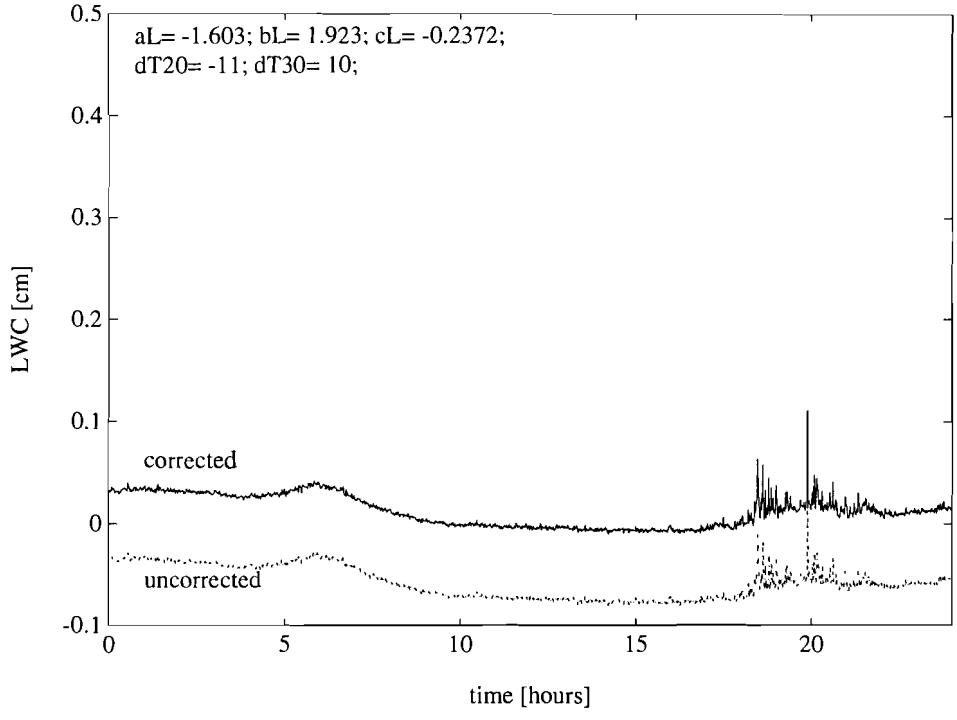

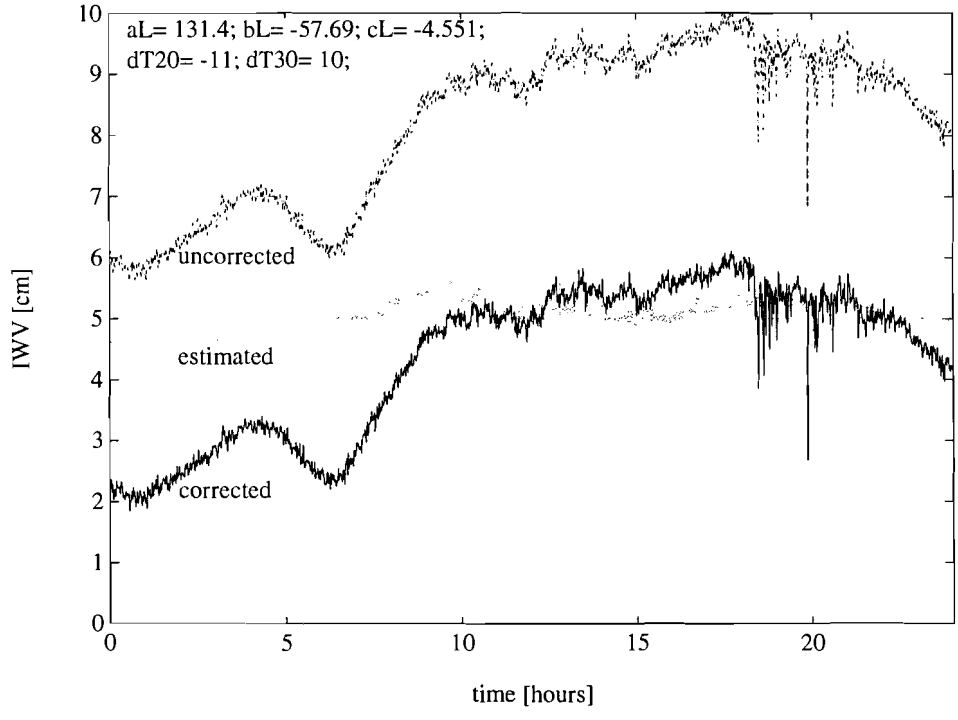

Figure 3.12: *LWC* (top) and *IWV* (bottom) for July 29, 1991 with DAPPER algorithm.

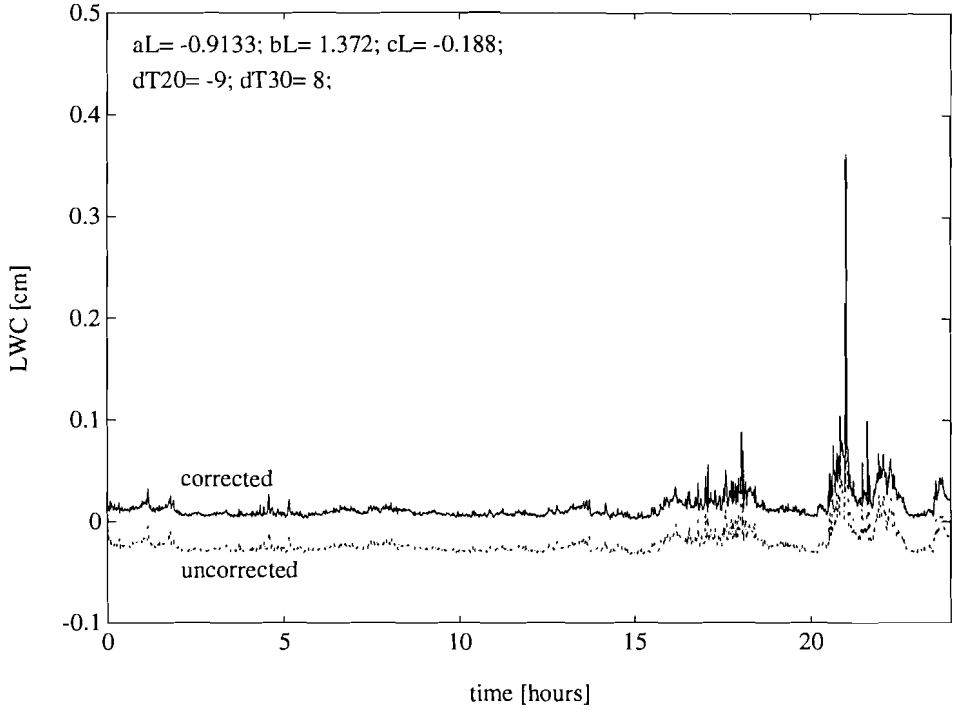

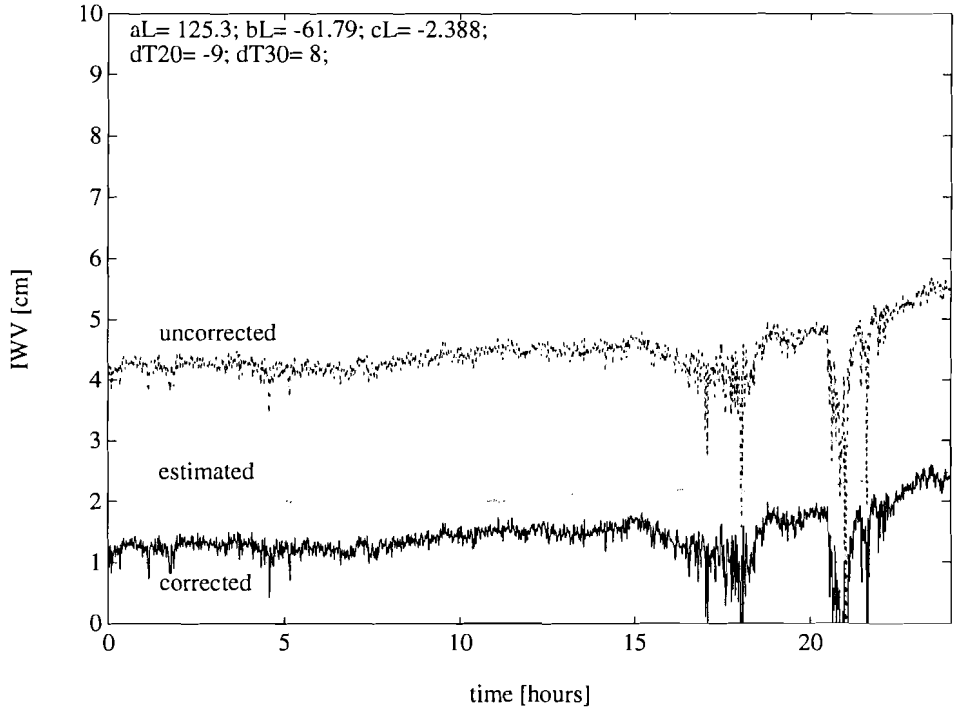

Figure 3.13: *LWC* (top) and *IWV* (bottom) for January 03, 1992 with DAPPER with *Franssen*'s coefficients.

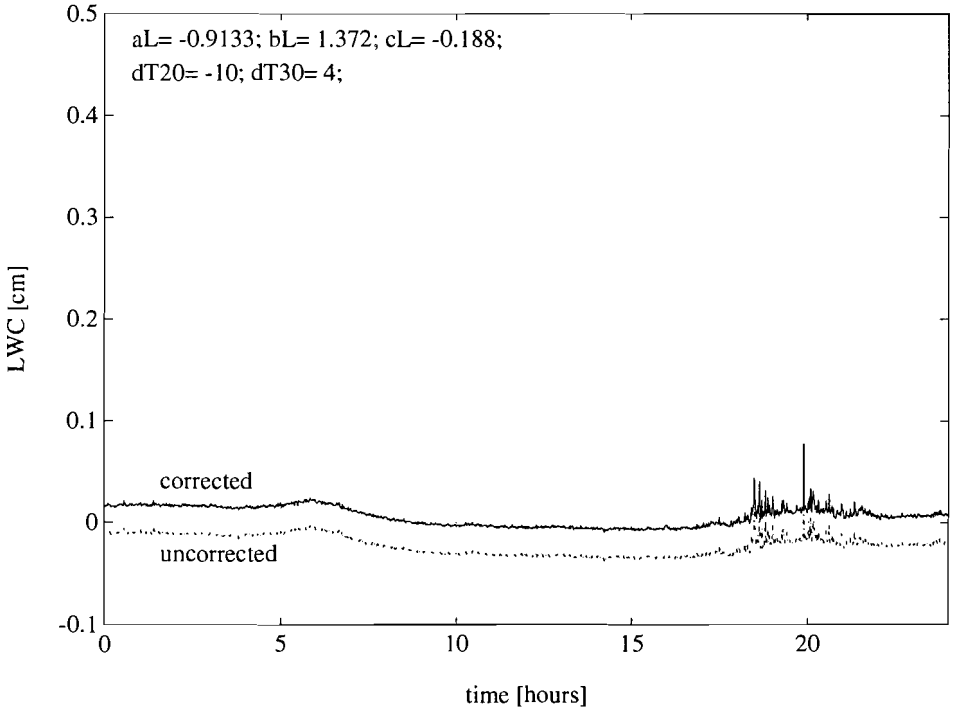

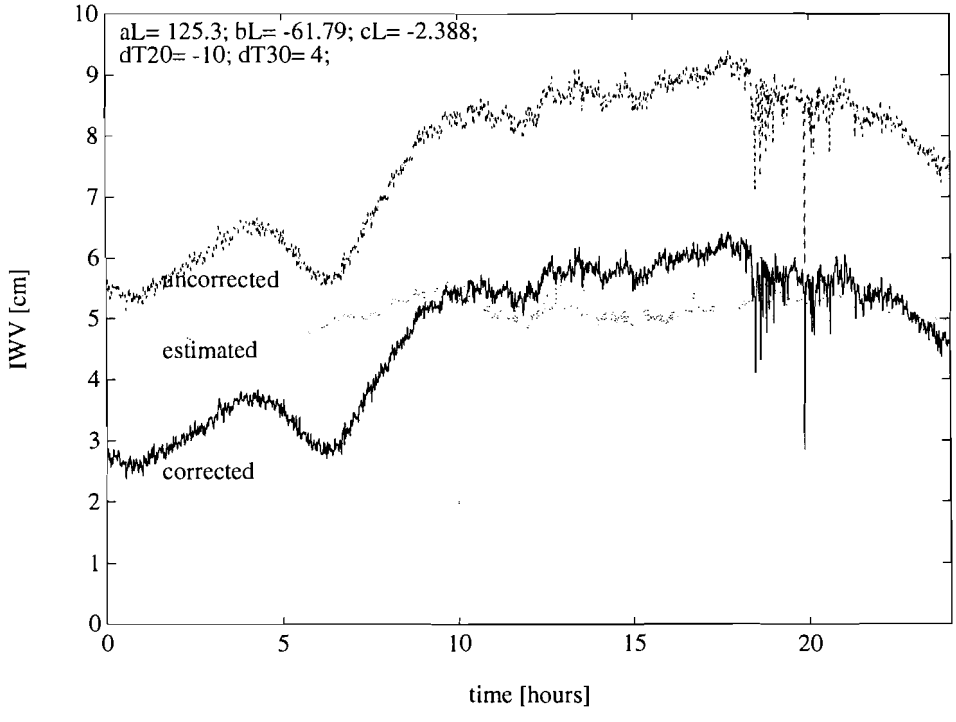

Figure 3.14: *LWC* (top) and *IWV* (bottom) for July 29, 1991 with DAPPER with *Franssen*'s coefficients.

3.6 Conclusions

First a 'balanced' correction with ΔT on the brightness temperature was made to see if this might be a good solution for the problem of negative *LWC*. Different ΔT's were necessary for the EUT-algorithm for both seasons and both frequencies. Unbalance was also found for *Lavergnat*'s algorithm. Better performance did have the DAPPER algorithm.

Next some possible sources of inaccuracies in the whole system, both theory and practice, were reviewed. Some do have significant influence on the inversion algorithms. But these inaccuracies can not cause the large ΔT necessary to correct the measurements. Only a part of it can be explained with this. Optimizing the coefficients of the EUT inversion algorithm for the season of year did not enhance the performance of the algorithm.

Subsequently integrated water vapour was included to determine a more consistent result for ΔT. Only for the original DAPPER algorithm a satisfying result was found. Applying DAPPER with *Franssen*'s coefficients gave worse, not consistent, result. Inverting radiometric data while using ΔT_{20} and ΔT_{30} gave *LWC* more in line with physics. So best results are achieved by the following inversion algorithm (DAPPER):

$$\begin{aligned} IWV &= 13.141 \cdot (A_{20} - 9) - 5.769 \cdot (A_{30} + 10) - 0.455 \quad [cm] \\ LWC &= -0.160 \cdot (A_{20} - 9) + 0.192 \cdot (A_{30} + 10) - 0.024 \quad [cm] \end{aligned} \quad . \tag{3.20}$$

In eq. (3.20) conversion from V,L [kg/m^2] to *IWV*, *LWC* [cm] is implied.

Chapter four
Cloud classification

4.1 Liquid water content

Clouds are formed if the relative humidity approaches or is hunderd percent. This phenomenon is refered to as saturation. The relative humidity depends on meteorological variables as temperature, pressure and so on, as in App. A can be read.

Water clouds can exists at high temperatures, +10 [°C], as well as at temperatures below the freezing point, down to -12 [°C]. At temperatures below freezing point ice crystals are growing and the cloud may be composed of a mix of water droplets and ice crystals. Ice crystals however, do not contribute to brightness temperature or attenuation. They only affect the polarization of the electromagnetic waves. Clouds containing only ice crystals normally exists at high altitudes and are mainly cirrus type clouds.

Other types of clouds, however, do have a liquid water content which is not always negligible. An overview of some general characteristics of these clouds is given in Table 4.1. In the first column the type of cloud is given. In the second the liquid water density and in the third and fourth the base and top heights. The values are valid for mid-latitude sites, but are usefull as indication of what can be expected. It is noted that there is a high variation in the nature of clouds. Densities up to 10 [g/m^3] may occur. In Table 4.1 for three types of clouds two examples of their characteristics are given. This indicates the nature of the clouds. With e.g. the liquid water density different vertical extents occur.

Cumulus type of clouds can have large vertical extent, e.g. 7-10 [km]. Generally these clouds have a high liquid water content. Often three species of cumulus are distinguished. For both cumulus humilis and cumulus mediocris a typical value of liquid water density (*LWD*) of 0.3 [g/m^3] is found. The density of these clouds rarely exceed 1.0 [g/m^3]. For the cumulus congestus the *LWD* varies between 0.5 and 2.5 [g/m^3] while it has a large vertical extent (from [*Cotton*]).

A type cloud not listed in Table 4.1 is cumulonimbus. Cumulonimbus can have a vertical extent even up to 12 [km], where as the *LWD* usually varies between 1.5 and 4.5 [g/m^3]. This large vertical extent is caused by an intense turbulence inside these type of cloud. Stratus clouds have a *LWD* of 0.25 [g/m^3] with a maximum of approximately 0.6 [g/m^3]. In App. B a detailed description of the various cloud types is given. Also a way to determine which clouds are present in the sky at a time are given in App. B.3.

The presented characteristics of clouds are quite general, in fact each cloud is unique, depending on time varying meteorologically circumstances. As a consequence most meteorologists gives different general values for the liquid water densities and base and top heights.

Table 4.1: Overview of various types of clouds[1].

	d_{liq} [2] [g/m^3]	h_{base} [m]	h_{top} [m]	ΔLWC [cm]	ΔT_{30} [K]
Cumulus	1.00	660	2700	0.20	112
Altostratus	0.41	2400	2900	0.02	11
Stratocumulus-1	0.55	660	1320	0.04	40
Stratocumulus-2	0.30	160	660	0.02	8
Stratus-1	0.42	160	660	0.02	12
Stratus-2	0.29	330	1000	0.02	10
Stratus-Stratocumulus	0.15	660	2000	0.02	11
Nimbostratus	0.65	660	2700	0.13	73
Cumulus-Cumulus-congestus	0.57	660	3400	0.16	86

[*Slobin*] used the saturating mixing ratio (grams of water per kilogram of dry air) and water vapour density at the top of the cloud to determine the *LWD* of the clouds:

$$LWD = \left(W_{cloud,base} - W_{cloud,top}\right) \cdot E \cdot 0.6 \cdot \rho_{top} \quad [g/m^3] \quad . \tag{4.1}$$

With *LWD* defined as the liquid water density, W_{cloud} the saturating mixing ratio in [g/kg], E the dry air entrainment of the cloud and ρ_{top} in [kg/m^3]. The dry air entrainment is 0.4 for stratus type clouds and 0.2 for cumulus type clouds. It is a measure for the penetration of dry air into the cloud.

It was assumed that the clouds were formed locally by saturating rising parcels of air containing water vapour. The water vapour content at the point where the relative humidity reaches hundred percent is determined from the saturation mixing ratio. As the air continues to rise, the saturation mixing ratio decreases due to decreasing temperature. The difference in mixing ratios between top and base is then the amount of water vapour that has condensed out as liquid water. Both saturating mixing ratio and ρ_{top} were obtained from a large number of radiosonde measurements. In this way Table 4.1 was formed.

4.2 Cloud properties

One of the major disadvantages of both the MPM- and CCIR-models to compute brightness temperature, is that they require a cloud temperature as input parameter as discussed in paragraph 3.2.2. They assume a uniform temperature throughout the whole cloud, which certainly does not match with practice. Figure 4.1 illustrates a temperature profile while a stratocumulus cloud is present. The presence of a cloud is clearly marked by a temperature inversion at 480 [m]. The (cloud-) temperature varies by height. This plot is made by aircraft sounding. A radiometer tend to smoothen considerably a structure as is shown in the Figure.

---

1) Extracted from [Slobin].

2) d_{liq} : liquid water density

As is proved in paragraph 3.2.2, cloud temperature is of significant influence on the brightness temperature. The plot in Figure 4.1 shows also a cloud base altitude lower than as in Table 4.1 is indicated.

Due to turbulence, in particular in cumulus type clouds, the top of the cloud is likely to be very lumpy and hence large fluctuations in liquid water will exist. So cloud top radiative emittance and absorption differ considerable from that found in a more homogeneous cloud.

There is some kind of critical *LWD* above which clouds produce precipitation. Generally this is as the liquid water density is in excess of 0.5 g/m^3. Of course other factors such as wether the air mass is continental and wether the cloud is supercooled, also control the critical *LWD* for initiating precipitation.

As a secondary effect, precipitation-size drops can contribute significantly to the liquid water-content. They can affect cloud absorption appreciably. So it can be stated that the liquid water content depends on a large number of parameters which are not known. And measurements of these parameters is not possible from earth surface. Compared with above mentioned points it seems that the cloud models in the MPM- and CCIR-models are actually too simple. Estimating *LWD* or *LWC* by observing clouds from ground (both visually and with radiometers) is therefore difficult. So it is likely that only some correlation between radiometer measurements of the *LWC* and atmospheric observations can be demonstrated. If more information can be extracted than it is an advantage.

Because of the high *LWC* clouds almost, but not yet, in state of precipitation are of interest. These clouds have a significant respons on the radiometer measurement system. But events showing precipitation should be excluded.

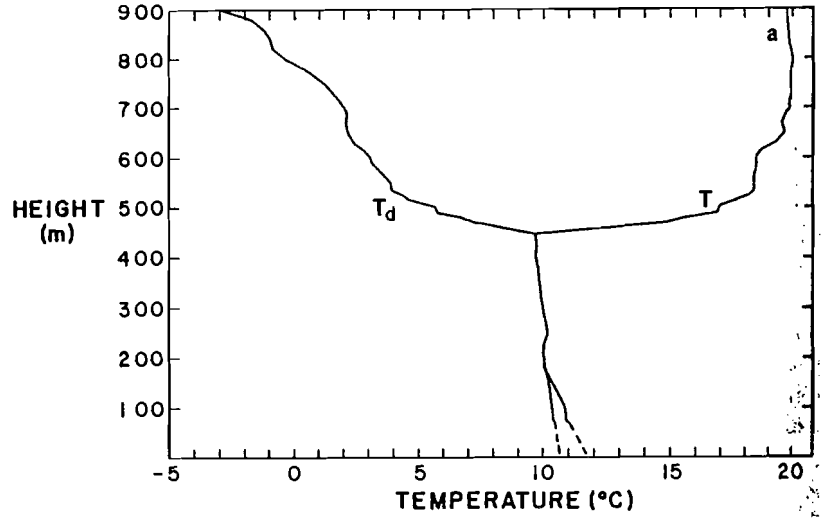

Figure 4.1: Temperature (T) and dew point (T_d) height profile from a NCAR Electra aircraft sounding at 37.8° N, 125.0° W, between 15:22 and 15:26 GMT. Sea surface temperature is equal to surface air temperature. Subcloud layer has a dry adiabatic lapse rate, the cloud layer a moist adiabatic lapse rate of 0.5°C/100m (from [*Cotton*]).

4.3 Additional cloud information

With ground observations it is impossible to determine if there occur multiple layers of clouds. Impossible to determine too is the vertical extent of the cloud. And at the EUT satellite ground station cloud base heights can not be measured. Therefore these data, used in App. D in the eventlist, are based on those administrated by the Dutch meteorological services, the KNMI.

Over distances of 50 - 70 [km] a cloud will not have a large varying base height, for the same type of cloud and under the same weather circumstances. So basing cloud information on these administrated by the KNMI is possible. But Eindhoven (NL) has an airfield at which base heights of clouds and their coverage are registrated. This airfield is approximately at 7 [km] distance. So this data is reliable for us. Although yet the cloud base height is not used in the analysis, later it may be.

Chapter five
Cloud observation equipment

5.1 The radiometer antenna

An overview of the radiometer antenna system is given in [*Dijk*]. Most important points for our purpose is the antenna beam widths.

The EUT radiometer antenna has different beam widths for the two frequencies of interest. For the radiometer frequencies the θ_{3dB}-values yield those given in Table 5.1.

Table 5.1: θ_{3dB} for the radiometer antenna.

	20 [GHz]	29.8 [GHz]
θ_{3dB}	0.7°	0.5°

5.2 The video camera

Optical observations of the atmosphere are recorded by a camera. Overlaying the image of the camera with a picture which outlines the θ_{3dB} gives the part of the cloud that is in the antenna beams. To know what part of the video image is in the θ_{3dB} outline, the beamwidth of the camera lens is required. In Figure 5.1 the observation equipment setup is given and in Figure 5.2 a measurement setup for the camera lens beam width is given.

As imager a video camera with recording possibilities (a camcorder[1)]) is used. Both monitoring and recording are possible. The video output can be connected with a PC which contains a video capture board. Single and multiple frames and continuous video can be stored in the PC. Image processing software may be used to edit stored images or to print single frames.

So first the camera lens beam width should be figured out. As an object for the beamwidth measurement a grid with squares of five [cm] is used. At this way h and w can easily be determined. The zoom and focus options of the camcorder are adjusted to maximum distance and zoom. It is assumed that the center of the video image is aligned with the radiometer direction. A check with the grids proved that this is accurate within one centimeter of the grid. With the equations

1) This is a Philips Explorer camcorder, type VKR9000.

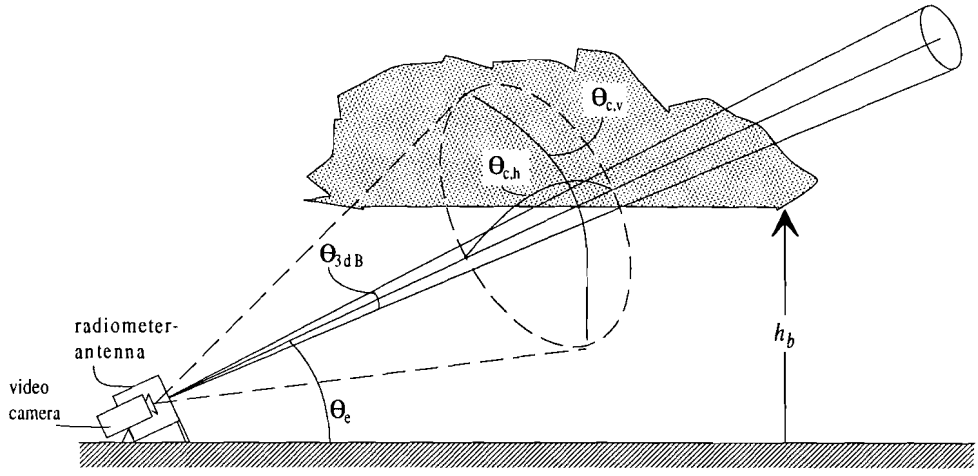

Figure 5.1: Schematic of observation equipment. Note that the vertical and horizontal camera lens beam angles, $\theta_{c,v}$ resp. $\theta_{c,h}$, are not necessarily equal.

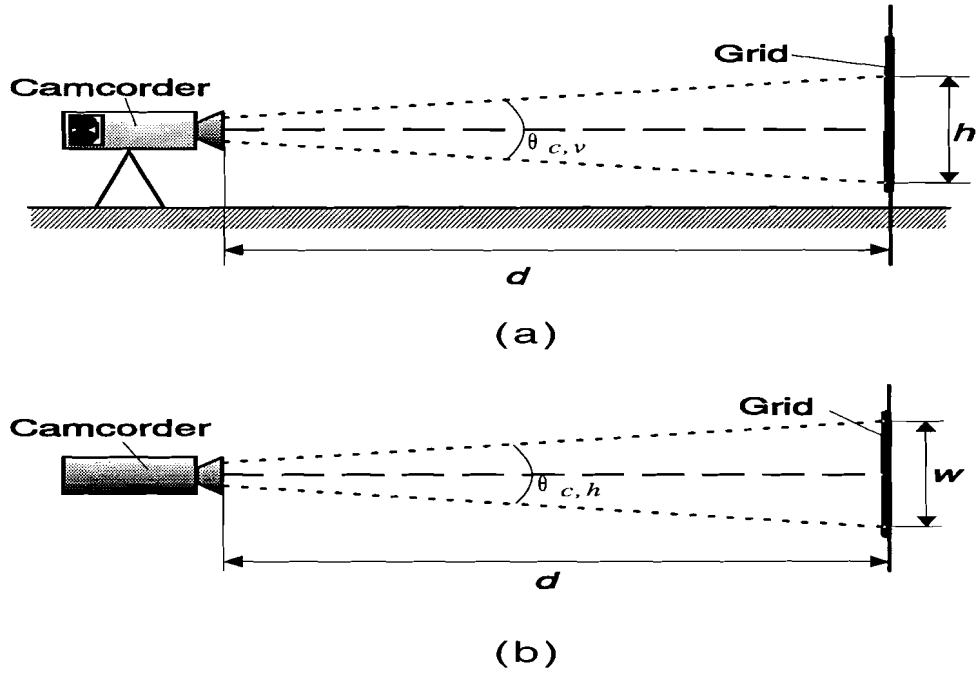

Figure 5.2: Beam width of view of video camera; (a) Side view; (b) Top view.

$$\tan\left(\frac{\theta_{c,v}}{2}\right) = \frac{h}{2 \cdot d}$$
$$\tan\left(\frac{\theta_{c,h}}{2}\right) = \frac{w}{2 \cdot d} \qquad (5.1)$$

the angles $\theta_{c,v}$ and $\theta_{c,h}$ are determined. Distances are d= 24.7 [m], h= 2.0 [m] and w= 2.7 [m]. So the angle are $\theta_{c,v}$= 3.80° and $\theta_{c,h}$= 5.20° by maximum zoom.

With these two quantities and those in Table 5.1, an overlay as given in Figure 5.3 can be made for the recorded image of the clouds.

Before recording any cloud, some preparations on the camera have to be made:

Of course elevation and azimuth angle have to be aligned with that of the radiometer
Set focus on manual, and manually set zoom and focus to maximum
Set white balance to daylight (☼)
Check the date- and time-indication, should be GMT-time

Now the camera is ready to record. But care must be taken during noon. Around noon it is possible that the sun will shine right into the camera lens. This may cause the CCD chip registrating the video image to become defect. If the sun is shining right into the lens recording should be stopped and the lens covered.

Another case but related to the one just described is that during some time intervals bright areas in the image occur. This is because at those times the sun is almost in the camera lens beam. Under these circumstances it may be difficult to distinguish anything in the image. Placing the camera in the shadow of the radiometer or some kind of shield prevents this.

There is mainly one disadvantage of using a camcorder. The maximum recording time of the video tapes are short, only 45 min. for VHS-C video tapes. Of course a video recorder can be connected to the camcorder to increase the total recording time. This can be done if the observation setup is proved to be succesfull.

5.3 Software setup

Video recorded on tape is captured by software and stored on harddisk for further editing. To be able to capture video, a special interface card for the PC is required. For this purposes a Video Blaster Capture board has been used. Provided with this hardware are some software programs. Of these programs Video for Windows and Action! are of interest for our purposes.

5.3.1 Hardware requirements for the software.

The video capture board and the software demand some minimum performance of the PC. First a 486DX mainboard, 33MHz or faster, is necessary to maintain constant frame rate during capturing. Otherwise frames will be dropped. A lot of physical memory is useful, but because of restrictions of the Video Blaster it is not allowed to be larger than 15Mb. We have used 8Mb which appeared to be sufficient.

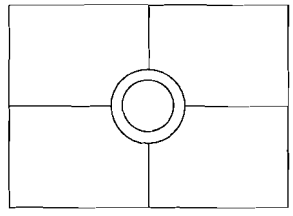

Figure 5.3: Overlay for video image.

Next a VGA video-adapter capable of 256 colours is required to maintain correct colour reproducing. Less colours are possible, but reduction of colour should take place with VidEdit, or already during capturing. Such reduction is not recommended, however. Decreasing the colordepth, the number of colours, results in lower resolution of the captured video. Although high-resolution VGA, such as SuperVGA (800x600 pixel) are common these days, standard VGA mode is used due to restrictions of the Video Blaster software drivers.

5.3.2 Video capture software

Video for Windows controls the capturing and supplies tools for editing and playing the captured video. The capturing software is VidCap. Frame by frame it stores the captured video on the harddisk. Frame rate and format of the image are adjustable. A tool for editing the sequence of video-frames and for compressing the videofile is VidEdit. For editing an image of a single frame BitEdit can be used. While with PalEdit the colourpalette can be controlled. MediaPlayer can play files of captured video.

5.3.3 Presentation software

Action! is a multimedia presentation program running under MS Windows 3.1. Captured video can be inserted in presentations with graphics, text and sound, although the latter is not of interest for us.

5.3.4 Supplemental software

Supplemental software is in the VideoKit-program of the Video Blaster. With this piece of software adjusting the Video Blaster on the video source is possible. This is necessary because each video source supplies the card with a slightly differently built video signal. The number of horizontal lines differs per type of source. So is the number of pixel of one line. Hence adjusting the capture-board on the video source is necessary.

5.4 Video capturing

Because the radiometer system offers measurements with 1 Hz sampling rate, frame rate of the captured video is chosen 1 Hz aswell. Experiments have been done with capturing video with several different video formats, i.e. the size of the image and the number of bits used to store colour information. Best result is achieved by a format of 400x300 pixel and 16-bit colour information. With this format the computer system still can store video frames without dropping anyone. The captured video frames are stored as full frames without compression, which can distort successive frames.

Distortion is unwanted because the recording already suffer distortion due to aliasing as a result of the pixel conversion. Also low contrast and patterns makes it difficult for the video capture board to process the digitized video to a representative image. This appears as even lower contrast and incorrect colours in the images. It is possible to enhance correct colour representation by applying an optimized colour palette during video capturing. In this palette are placed only those colours which occur on the video. But using an optimized palette did not improve the digitizing of the recorded sky view. This is probably due to the already mentioned low contrast and the occurrence of patterns.

After deleting unwanted frames with VidEdit editing of the video images is possible. The file format in which the video sequences are stored is the standard AVI-format of Video for Windows.

5.5 Video editing

Yet the size of the videos in the sequence is 400x300 pixel. For presentations with Action!, this is a good format. If only for example the center of the image, with the antenna beams projected on, is desired, 'cropping' of the video is possible. Cropping means that unwanted portions are deleted. Resizing (zooming in or out) of the video is possible too.

Say the center with a size of 280x210 pixel should be left over, while zooming in with a factor two. Than cropping is done by selecting the Video-menu of VidEdit, selecting the Crop-command and specifying X, Y, Width and Height values. For 400x300 ⇒ 280x210 these are respectively 130, 98, 140 and 105. So an video of 140x105 pixel is the result. Zooming is done by resizing the video to the 280x210 format. In the Video-menu the Resize-command is chosen after which Width (280) and Height (210) can be entered. The video is saved again and overlaying the video with the antenna beam outlines can be started.

Under Windows a macro is made which overlays the captured video with the outline of the antenna beams. Sequentially each frame is copied to the clipboard and pasted in an image editor overlaying by the antenna beam outlines. The esulting image is copied back to the clipboard and substitutes the original one in the video sequence.

5.5.1 Image editor

The image editor is PhotoLab 1.8a. Overlaying is performed by opening a DIB-(bitmap) file containing the antenna beam picture (filename is 'target.dib') and multiplying the picture with the clipboard. The antenna beam outlines are black lines on a white background. For each pixel of the picture the colour bit is multiplied with the corresponding one of the image on the clipboard. Because black is number 0, this always results in colour 0 (black). White is number 1, so the original colour of the video image is maintained.

Of course the picture of the antenna beams is of the same size as the digitized video is.

5.5.2 Provisions for running the macro

For correct operation of the macro some assumptions are made. First of all, PhotoLab is supposed to be active but minimized in the lower right corner of the screen. And its window covers the entire screen when it is opened. These provisions have to be made due to the way Windows handles programs. Next the Windows macro recorder, with which a macro is recorded, should be opened and running minimized while the file 'macro.rec' is loaded which contains the macro. The

macro-name is OverlayForVideoImage with as short-cut key Ctrl-Shift-Space. To execute macros this is default way in Windows. Of course VidEdit should be running with the appropriate AVI-file loaded. Now the macro may be executed by pressing Ctrl-Shift-Space. Because it is difficult to make the macro to detect the end of the video sequence, the macro has to be stopped manually. This is done by pressing Ctrl-Break and the macro is aborted.

5.5.3 Actions of the macro

Next point by point the actions the macro takes are described. These are also the commands executed while recording the macro.

Ctrl-C : Copies current frame to clipboard
Double-click on the PhotoLab icon maximizes the program
F(ile) : Opens the filemenu
O(pen) : Gives the opportunity to enter a filename.
d:\movies\target.dib
: This is the full pathname of the picture of the antenna beams.
I(mage) : Opens the image-menu
b(Combine) : Opens the combine-menu
↓↓↓ : Press down-cursor three times to go to multiply option.
↵ : Executes multiplying.
E(dit) : Opens editmenu
C(opy) : Copies resulting picture to clipboard
Click on Control-menu box in upper left corner of window.
M(inimize) : Minimizes the program to an icon in the lower right corner (makes VidEdit the active window).
Ctrl-V : Paste the clipboard into the videosequence (before the original image).
D(elete) : Deletes the original image

In Figure 5.4 an overview of the steps made is given. In Figure 5.5 a monitor-screendump is given, Note the place of the image editor in the lower right corner. The window of VidEdit is open at the left side. And the icon of the program Recorder is the fourth one from the left at the bottom row.

5.6 Plot of *LWC*

5.6.1 Radiometer data

For retrieving LWC out of the radiometer data, the DAPPER routine as given in §3.6 is used.

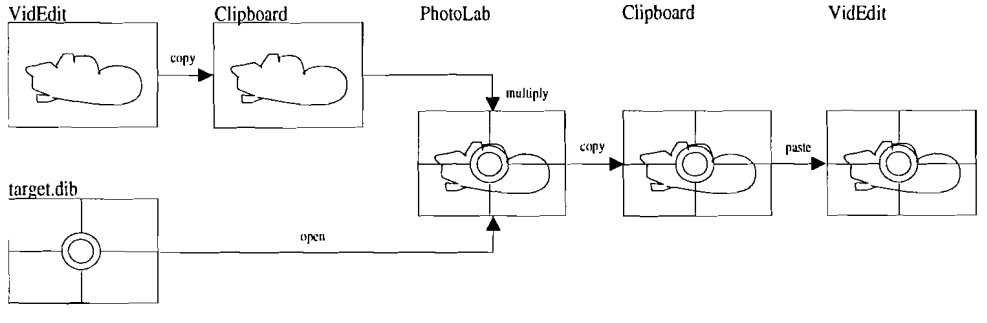

Figure 5.4: Editing the captured video.

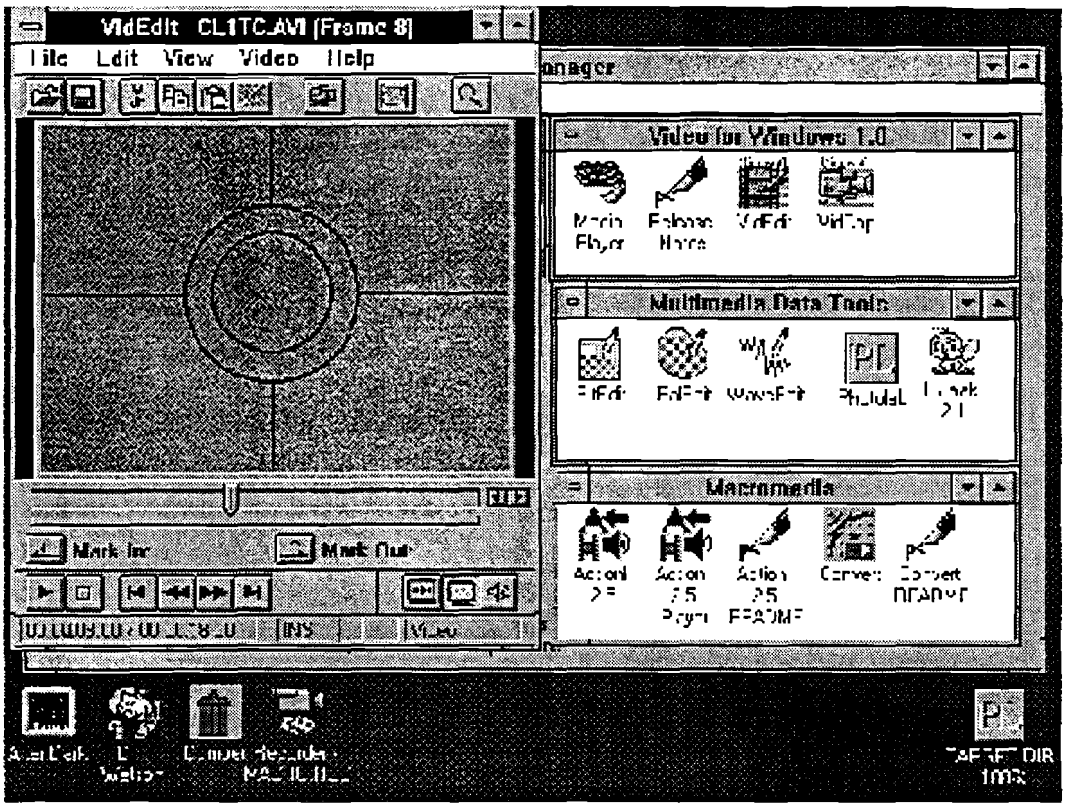

Figure 5.5: Screendump during video editting.

5.6.2 *LWC*-plot

For all plots uniform axis-scaling is used as in the next paragraph is described. Only if for a certain time period the *LWC* exceeds the bounds, scaling should be adjusted.

Because the plot is made with Matlab, conversion from Matlab's metafile-format to a format Action! uses has to be performed. Unfortunately the graphics preprocessor of Matlab (for DOS) has only one useful outputfileformat, that is HGPL. Action! can not read this file format, as a matter of fact it can only read graphics of the Windows file formats BMP, DIB and WMF. Conversion to the WMF-format is performed by HiJaak v2.1, a program specialized in format-conversions.

In HiJaak the options are set to:

File to be converted:	*.hpg
Destination file:	*.wmf
PGL source options:	Pen width: 1
	Fontname Trumbull
	[X] Trim surrounding whitespace
Set options:	Rotation: 90°
	Width: 3.3 inch (to be specified for own needs)

Rotation is required to get the graphic horizontally. When the new Matlab-release 4.0 is available conversion is not anymore necessary because this version operates under Windows 3.1. Than it is easy to exchange graphics between Matlab and Action!.

5.7 Including video in presentations

Action! v2.5 is a multimedia presentation software package capable of integrating sound, live and captured video, graphics and text in one presentation. For my purposes the basic presentation should play the captured (and edited) video while at the same time, synchronized, the inverted liquid water content is graphically shown.

The time-axis of the both video and *LWC*-plot will normally be a short time period less than one minute. This is varying over the whole day during the period of daylight. The vertical axis of the *LWC*-plot is common varying between -0.1 and 0.5 [cm] although values out of this bound are possible. So it is important that the time-axis can be adjusted easily.

Action! provides transitions (in time) of the graphics so image can be revealed in a certain direction during a time period. This makes it easy to show the time dependence of the *LWC*-plot. Normally left-to-right revealing is used. But right-to-left, up or down are also possible if the movement of the clouds in the video makes it necessary. It is more a personal choice.

Making a presentation with video and graphics is done at the following way in Action!:

Import captured and edited video sequence ('*.avi' format)
Double click on '*.wmf' to open the Edit Object window
Select Enter
Select in Transition: Reveal Left or Right (the first one if time axis is from right to left)
Change the duration to almost the maximum scene time
Select Hold and change its duration to a minimum of e.g. 1 sec.
Activate Timeline for synchronization purposes
Adjust duration times of all other objects to that of '*.wmf', because it is likely that they are all changed
Synchronize video to the appearance of '*.wmf' to make them start at the same time and/or adjust slightly Enter- and Hold-times of '*.wmf'

It should be noted that the use of colours in Action! is not always clear. Action! primarily uses the colour palette of the captured video. If a colour is used for text or graphic purposes in the presentation before a captured video is imported, it is likely that the colours of the text and the graphics are changed. There is one to prevent this, and that is first importing the video sequence and then making the text and graphic objects in the presentation. But care must be taken, because even that will not give hunderd percent guarantee that the colours will not change.

5.8 Including video in documents

Captured video sequences are generally not very practical to present results in paper documents. However, there are two possible ways to include some results in documents. First, every or selected frames are handled as independent images. These can be imported in documents and placed successively in the correct order (Figure 5.6). Major disadvantage is that it occupies a lot of

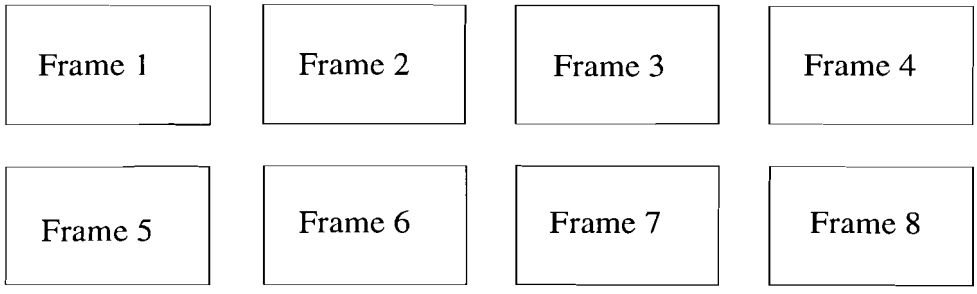

Figure 5.6: Video frames in sequence.

space and there is no clear overview in the path of the cloud. A second method is to cut out only the front of the cloud and paste them together in one picture, with a correct alignment in time (Figure 5.7). If the cutting out is carefully done, development of the cloud is clear.

Because the last method is more convenient this one will be used. With the programs available the following should be done:

Open VidEdit and load the appropriate '*.avi'-file
Go to the last frame
Copy this frame to clipboard
Open PhotoLab
Paste from clipboard
Convert to 256-colour (Adaptive palette)
Copy to clipboard
Open BitEdit (#1)
Paste from clipboard (this image will be target-image)
Open BitEdit (#2)

Label: Go to VidEdit
Go one (or more if desired) frame back
Copy to clipboard
Go to PhotoLab
Paste from clipboard
Convert to 256-colour (Adaptive palette)
Copy to clipboard
Goto BitEdit #2
Close previous bitmap (not saving, not when BitEdit is enter for the first time)
Paste form clipboard
Select area of interest with mouse

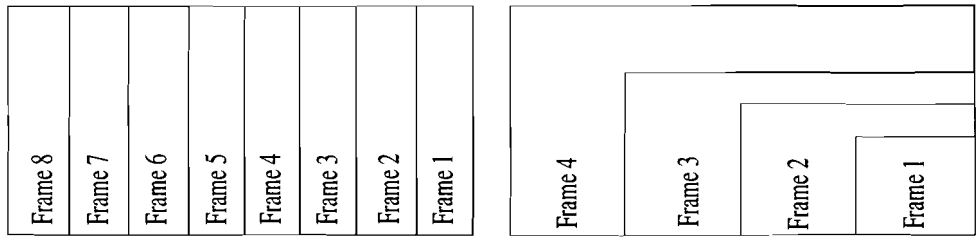

Figure 5.7: Video frames cut and pasted.

Copy to clipboard
Go to BitEdit #1
Paste from clipboard (Ok to map palettes)
Place area at correct position
Go to label if not all desired parts of the frames are placed in BitEdit #1.

At the end, BitEdit #1 contains the bitmap of the cloud development. Now saving and including it in a document is possible.

As described above PhotoLab is used to convert the 16-bit colour image to one of 256 colours. This is because BitEdit can only handle image with 256 or less colours. And BitEdit is the only image editor with which it is easy to cut and paste parts retaining the original size of the cut-out. It might seem a clumsy way, but again under Windows using the mouse every thing is easily done. And more over, there is no alternative. By lack of capabilities of the image editors (many have been examined) it is the only way such result can be obtained. But the main advantage is that this method of representing the development of clouds occupies much less space in documents than the one in Figure 5.6.

For a clear overview it is handy to maintain a constant time difference between the cut and pasted video frames. Placing the cloud development and the results of the retrieved *LWC* next to each other gives the same overview as Action!, the presentation program, does.

5.9 Conclusions

With a video camera events of clouds obscuring the radiometer antenna beam can be recorded. With the aid of a video capture board it is possible to store video on a computer harddisk, available for further editing and research.

With the known antenna beam width and the measured beam width of the camera lens an overlay for the video recordings has been made. In general a clear image of the captured video is obtained. But some distortion takes place under some circumstances.

The captured video can be included in presentations, run by the computer. With relevant parts of the video frames in one picture, a sample of the video can be included in documents.

Chapter six
Atmospheric observations

6.1 Radiometric scaling

6.1.1 Scaling of the radiometer

As mentioned in chapter three some defect occurred at the 29.8 [GHz] channel. In July 1993 the radiometer was dismantled and repaired. Therefore, after assembling the radiometer, new scaling factors for the radiometer had to be determined.

The radiometer system actually measures the antenna noise temperature T_{ant} and supplies it to the outer world as a voltage V_{out} , which can be processed with a computer acquisition system (in our case DAPPER). The noise temperature is linear related with the output voltage of the radiometer:

$$T_{ant} = k \cdot V_{out} + l \qquad [K] \ . \tag{6.1}$$

So with two different pairs (V_{out},T_{ant}) it is possible to determine the scaling factors k and l. This is done in two steps.

First the radiometer is pointed to zenith without the reflector system mounted. In this configuration contribution to noise due to the radiometer its surroundings is minimized. With surface temperature and the relative humidity or water vapour density known, and using the propagation models of the CCIR or *Liebe*, a theoretically brightness temperature is calculated. In an ideal case this value equals the measured brightness temperature, which is obtained in the form of V_{out} .

Next an absorber, a black box, is positioned over the feed of the radiometer. Now, only the 'radiation' of the absorber cause a V_{out}. This noise is the same as the physical temperature inside the black box. So now two pairs of (V_{out},T_{ant}), a high and a low, are known and k and l can be derived.

For the purpose of determining T_{ant} in the first step of the calibration, a diagram is plotted (in App. F) of T_{ant} versus ρ_0 , the water vapour density, with the surface temperature T_0 as parameter. In this way no difficult calculations have to be performed during calibration. An other method is to use a computer program to compute the brightness temperature as function of the meteorological parameters. Because calculation of the brightness temperature is time consuming, a program (READTB) is written that reads T_b out of a database. After entering the meteorological parameters, that is the relative humidity RH, the surface temperature T_0 and the surface pressure P_0 , T_b is retrieved from the database. As a matter of fact, the plots mentioned above were made utilizing this database. The database was computed with the CCIR propagation and atmospheric models [CCIR '90 respectively '88].

After installing the radiometer under the elevation angle $\theta_e = 26.8°$, the reflector system is mounted. As a control T_b is measured and compared with the theoretically expected value for this elevation angle. The program READTB can be used for this purpose aswell.

6.1.2 Changing parameters of radiometer

The correction factors ΔT_{20} and ΔT_{30} , as described in chapter three, were applied on radiometric data of before July 1993. Since the radiometer is repaired and hence has new scaling factors, it is likely that these factors are changed. It is quite easy to derive new ΔT_{20} and ΔT_{30} for this case. But unfortunately, since July 1993 another phenomena occurs. After correcting for extraterrestrial and ground noise, negative (!) values of T_{20} are found. Also the 12 [GHz] channel, although not used in the inversion algorithms, shows not correct operation. It seems that something is wrong in the radiometer system.

By placing a temperature sensor on the main reflector it was proved that heating of the reflector plates by the sun did influence the 12 [GHz] measurements. It is likely that by heating the main reflector deformates, which results in a broader beamwidth and therefore an other value for the antenna integration factor h. Deformation can occur because the reflector construction gives no room for extending reflector plates. Note that h is important to convert T_{ant} to brightness temperature (§ 3.3.4).

Broadening of the beamwidth especially degrades the performance of the lower frequency channels, because these have already a larger beamwidth than the higher frequency channels. In one way or the other, the 20 [GHz] channel is not operating good too. The measured values are for large time periods smaller than those of the 30 [GHz] channel and are sometimes even negative. As example Figure 6.1 illustrates this. Under normal conditions T_{20} should be higher than T_{30} .

Because of the time varying nature of the deviations it is very difficult to determine h, ΔT_{20} and ΔT_{30} . It might be even impossible. Only if a correct h is known, ΔT_{20} and ΔT_{30} can be derived. If only ΔT_{20} and ΔT_{30} are known still nothing can be said about h.

As a result inverting radiometric data has no sense at this time. If it is done *IWV* becomes negative and *LWC* is too high during clear sky periods. For further analysis the algorithm in eq. (3.20) is used to be able to do the analysis anyway.

6.2 Analysis of observations

6.2.1 Correlation of observations with radiometric data

With the observation setup given as in Figure 5.1, an image of the atmosphere is recorded on video tape. Events of interest are stored on the computer's harddisk in the way as described in chapter five. Now with the time plot of inverted *LWC* and the digitized video next to each other, comparing and hence checking the performance of the liquid water inversion can be started.

For a number of days, in Appendix D a short summary of weather circumstances and the time periods of recording and capturing is given. The list does not represents all days of observation. Some captured video events, stored on a data-tape to make space on the harddisks of the computer, were accidently overwritten by the tape-backup program. How this could happen is unknown. Because these files are not present anymore, it is of no use to put them on the list. These overwrit-

ten eventfiles, however, did subscribe the conclusions in the following part of this chapter.

What is left over are perhaps not so many days, but these are representative for three different cases to be determined. The small number of events is also partly due to the weather conditions during the period of observation. Days, cloudy during daylight, or on the opposite with clear sky, occurred frequently and were in majority. An early start of the winter caused long periods of days with stable weather conditions as mentioned above. This significantly reduced the number of available measurement days.

When a cloud is passing into the radiometer antenna beam and hence into the camera lens view, at first no reaction of the radiometric data is noticed. There is no correlation between video and radiometric data. This is illustrated by the video recording and the corresponding *LWC* for that time period shown in Figure 6.2. While the front of the cloud moves into the antenna beam, no response of the radiometer is noticed. Not only for this particular day this happens, or better said nothing happens, but also for other observed days.

In general for all days in the period of observation no "real" event as expected occurred. Sometimes the inverted *LWC* increased, but this happened when a cloud already covered the beams of the radiometer and the video camera for some period of time. In Figure 6.3 an example of such event is given. Because of the low contrast the digitizing of video results in a bad quality image. And because there is no front distinguishable the first method of including video in documents, as explained in paragraph 5.8 had to be used.

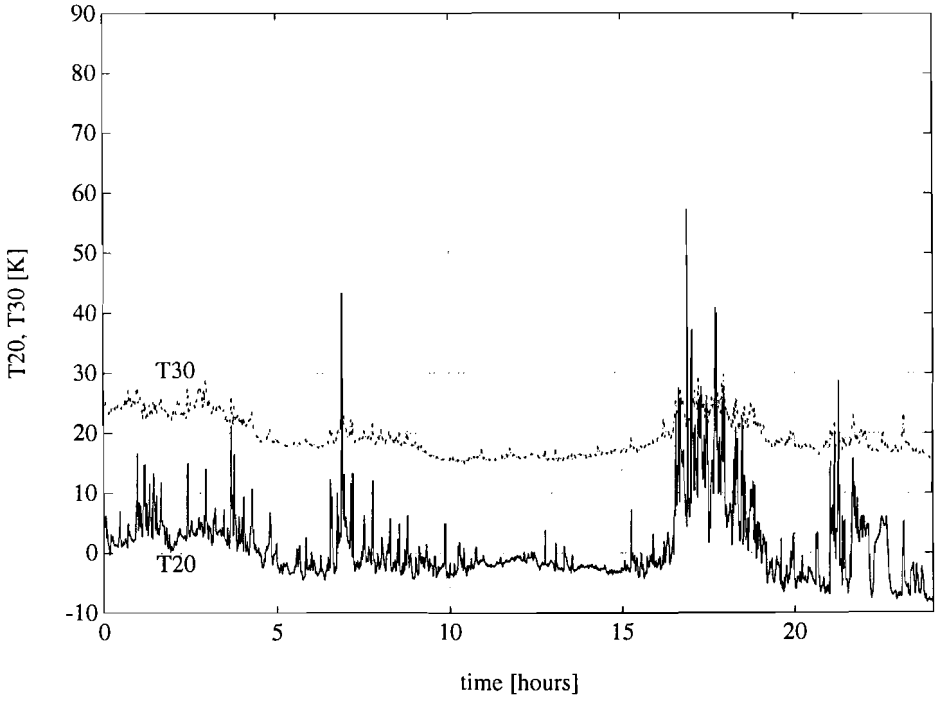

Figure 6.1:Brightness temperature T_{20} and T_{30} versus time. Note that for long periods T_{20} is negative.

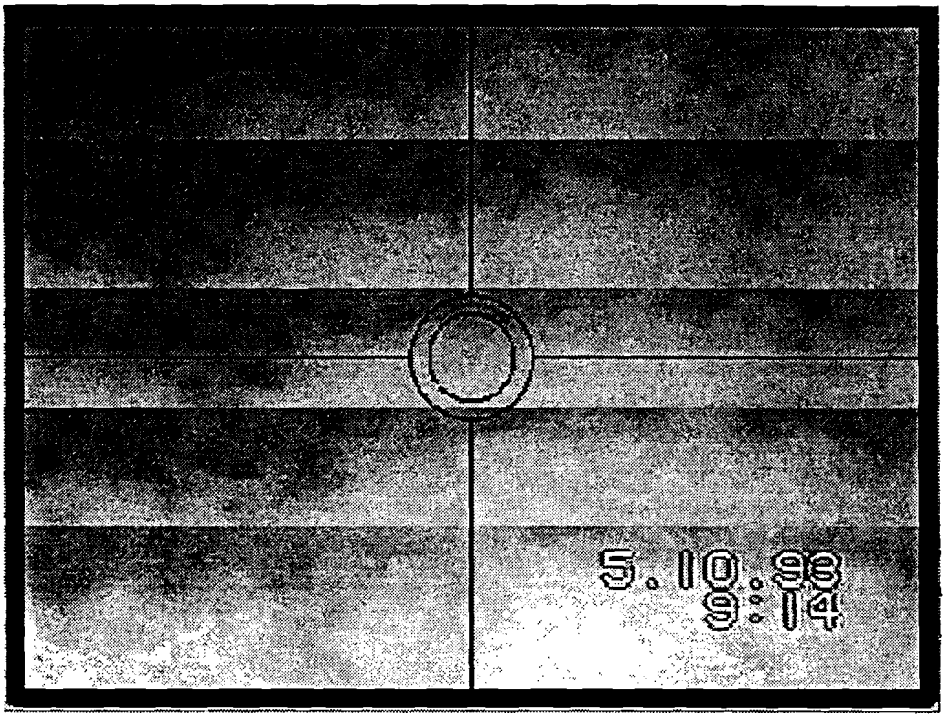

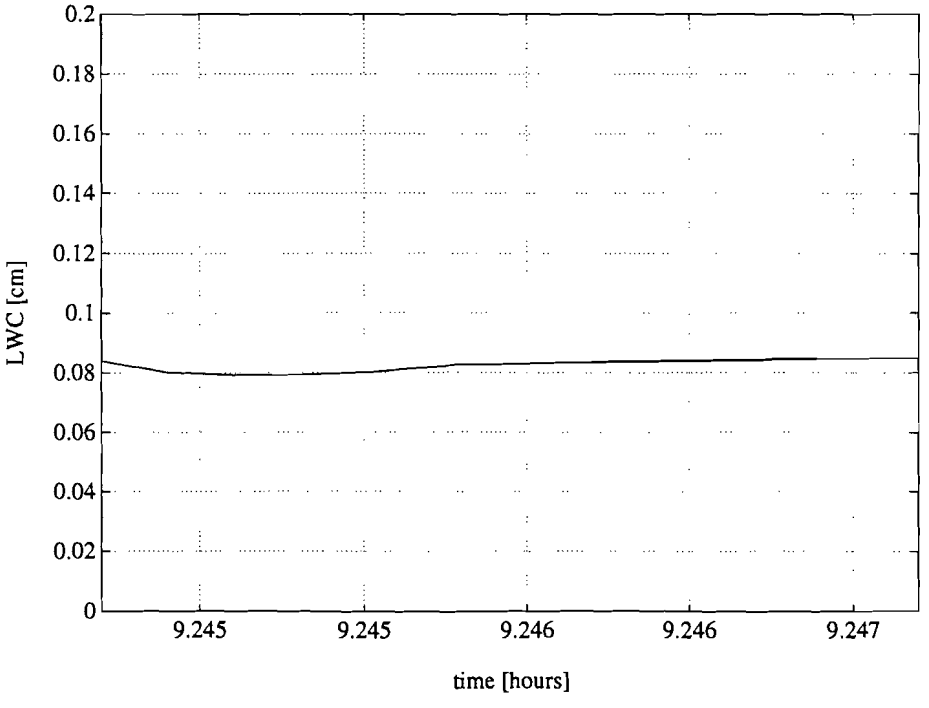

Figure 6.2: (Top) Oct 05, 1993, cloud is moving from bottom- to upperside and the frames are three seconds spaced, starting at 9:14:20 video time, 9:14:39 acquisition system time. (Bottom) Liquid water content for specified period.

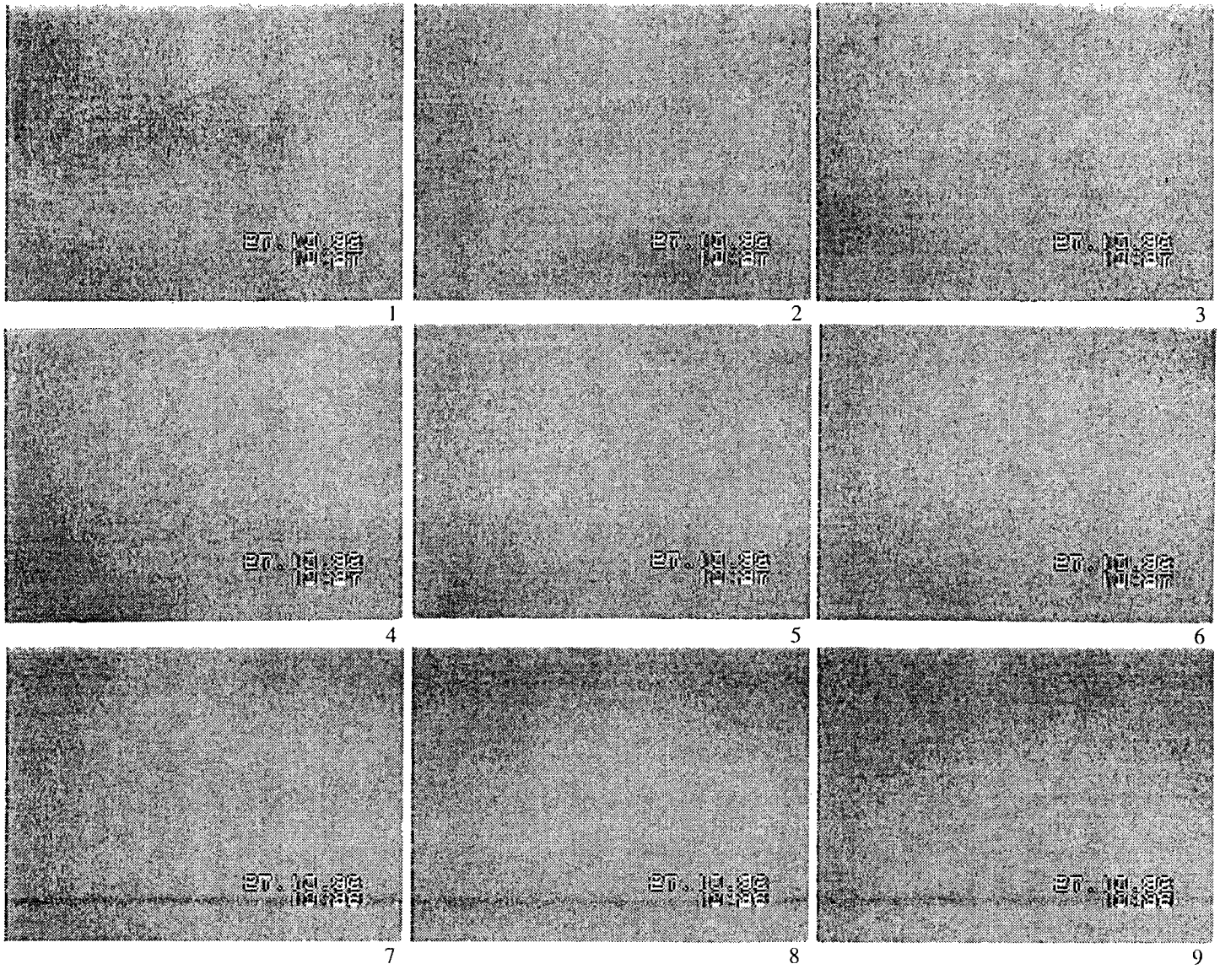

Figure 6.3a: Oct 27, 1993, cloud is moving from upper- to bottomside and the frames are ten seconds spaced, starting at 10:27:08 video time, 10:28:04 acquisition system time.

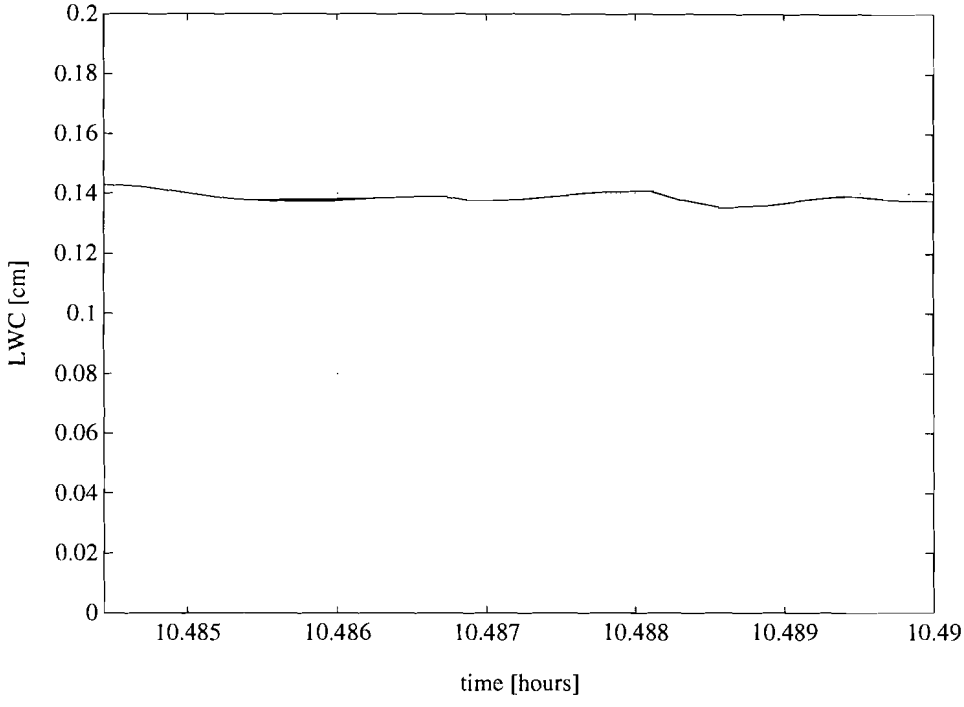

Figure 6.3b: Liquid water content for same period.

The most important reason that nothing happens when clouds were moving in the antenna beam, is the fact that the liquid water density at the edges of most clouds is not large enough. Only some cumulonimbus and some cumulus type clouds will give a desired radiometer response when the cloud edge is driving in the antenna beam. In these type clouds the sides can have a significant amount of liquid water as the inner part of the cloud has, due to the turbulence in those clouds. Other type clouds do not have a liquid water density in the side, high enough to contribute to the brightness temperature.

But as already mentioned comparing of video with radiometric data is not good to do because of the not well operating radiometer. The impact of this on the *LWC* and *IWV* is difficult to predict.

To be able to perform some reliable comparing anyway, some criterion had to be used. Of course only increasing *LWC* is marked as a radiometer event. A distinguish is made between real events and those caused by noise in the measured brightness temperatures. With the latter, only one of the frequency channels registrates a changing brightness temperature. Also events at which precipitation occurs are marked invalid.

6.2.2 Camera lens beam width increased

In chapter five it was stated that with an as small as possible camera lens beam width, so with maximum zoom of the camera lens, best recordings for further analysis is obtained. But after several recordings it was found that the observation equipment is not suitable for our purpose.

As mentioned before, with the current observation setup there is no correlation between video recordings of clouds moving into the radiometer antenna beam and the *LWC*. This is due to the low liquid water density in the sides of most clouds. As a consequence, decreasing camera lens beam width, to record more accurate, will not enhance the accuracy of the observation system. For the purpose of controlling the performance of the radiometer this system is therefore not well applicable.

Increasing the camera lens beam width, zooming out, may give some advantage. More information of the development of the cloud comes available. It might be possible e.g. to compare cloud forms with radiometer inversion or their velocity. But again for the main purpose of checking the inversion algorithm of liquid water inversion will be not usefull. In Figure 6.4 an example with increased camera lens beam width is shown. Instead of maximum zoom, the zoom is adjusted to minimum. Still focus remains on infinity. The image shown is slightly distored on the left side because the sun was starting there to enter the camera lens. For the presented time period in Fig 6.4 the LWC-plot is given too. The clouds observed in the images do not contribute to the brightness temperature and hence to the liquid water content.

Most clouds driven by and observed on video recordings give no or a neglectable increase in *LWC*, but it might be interesting to correlate increasing *LWC* with the observed cloud forms. Large extending and elongated clouds generally will give some response to the radiometer system. Note that the smaller the recorded area of the sky in the camera lens, the less information by visual analysis can be retrieved of it, unless some additional registration, or measurement, equipment are used.

If the camera lens beam width is increased, before the recording starts elevation and azimuth angle have to be set. For this purpose it is best to zoom in to maximum zoom first and set the angles. And after that, zooming out. At this way the alignment of the camera with the radiometer antenna is done most accurate.

6.2.3 Captured video quality

In all the Figures 6.2, 6.3 and 6.4 the contrast in the captured images is rather or very low. As already predicted in chapter three this is due to the low contrast, and the low number of colours, characteristic for clouds. When a broken cloud coverage is present as in Figure 6.4 the image is

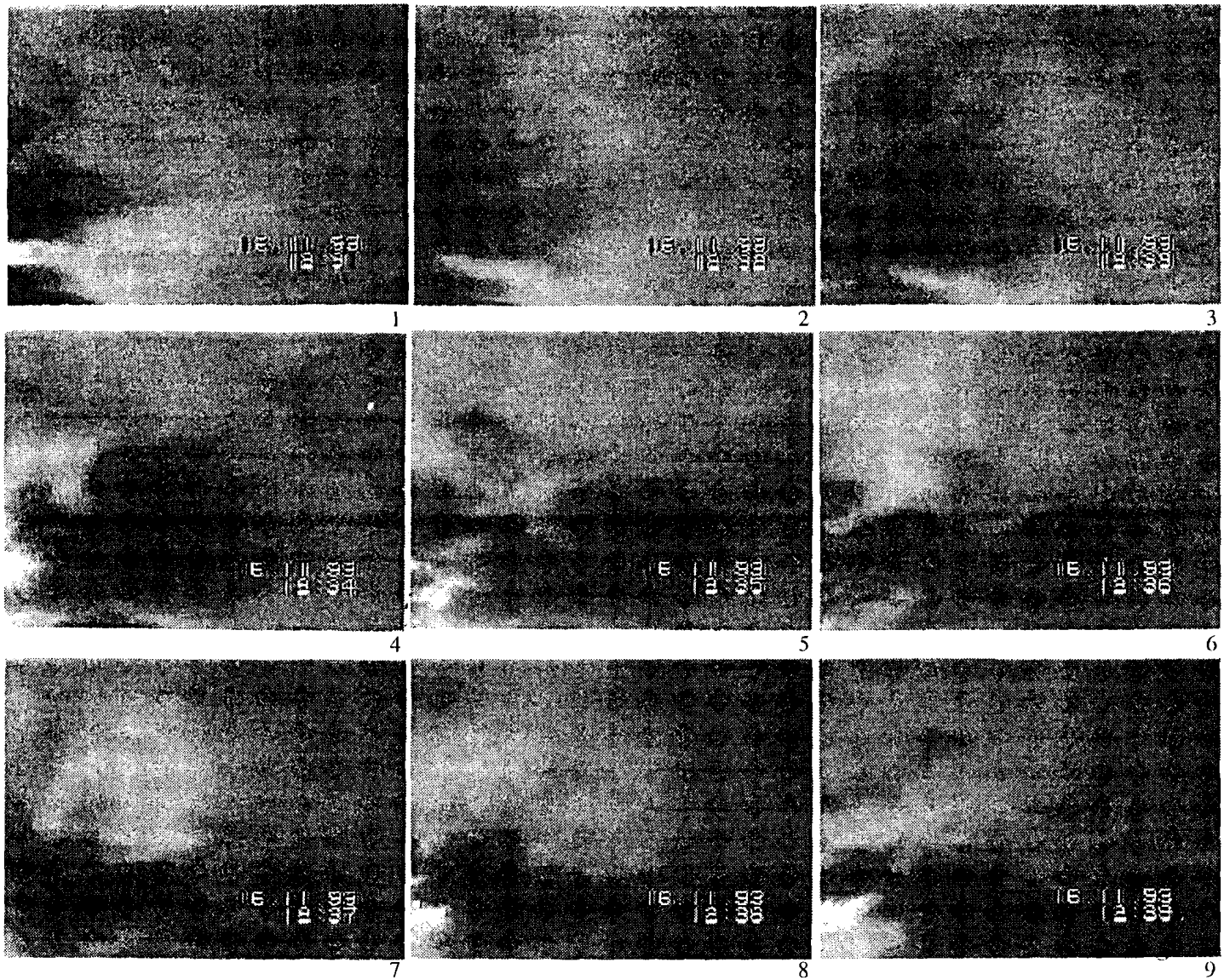

Figure 6.4a: Nov 16, 1993, clouds are moving from upper left- to lower rightside and the frames are sixty seconds spaced, starting at 12:31:00 video time, 12:32:58 acquisition system time.

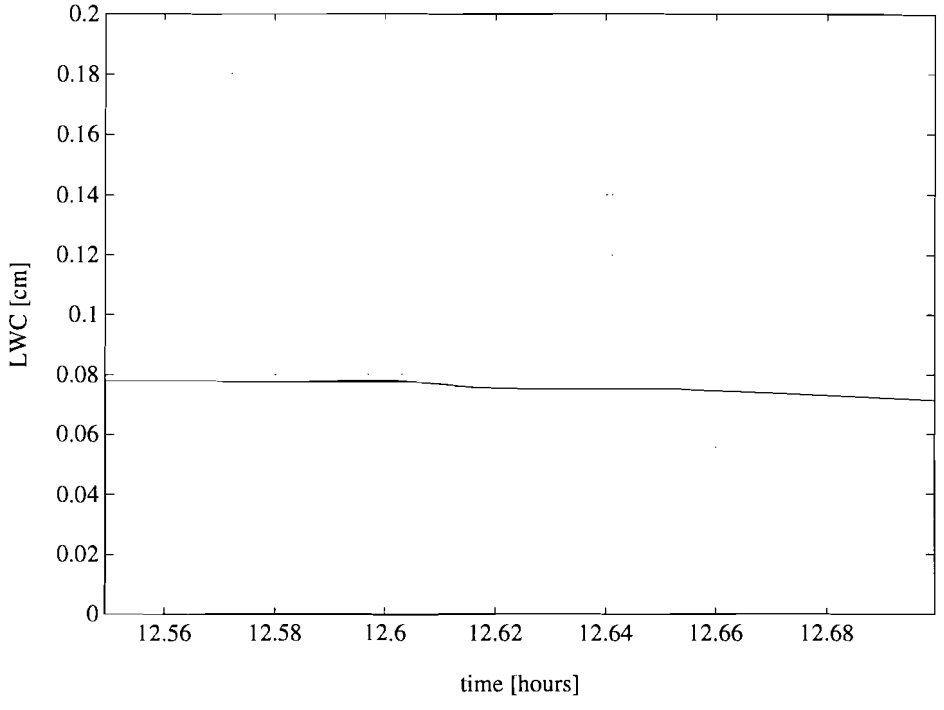

Figure 6.4b: Liquid water content for same period.

more distinctive. But the rather clear image is partly due to the shadowing effect of the sun nearby or behind the clouds. It gives a contrasting effect. So on the one hand a sun entering the camera lens distorse the image around the sun, on the other hand it improves the contrast in case of broken cloud coverage.

In Figure 6.2 a white cloud, actually a stratocumulus type cloud, on a blue sky background has a rather high contrast. It might be not visible in this image, but the more the cloud covers the image the contrast decreases. In Figure 6.3, where the cloud is covering the camera lens totally, there is hardly any contrast in the image, resulting in a poor quality of the captured video.

Note that although only three days are treated, these are only examples for three types of observations examined. First when a cloud front is moving through the image, second when a cloud is already covering the whole image and third for the case of minimum zoom of the lens.

In Figure 6.5 a screendump is shown of the presentation program Action!. At the left side a captured video is placed, while at the right side the corresponding *LWC*-plot. This plot is only visible partly. The rest is not revealed yet. The *LWC*-plot and video are synchronized. With this, when playing the video and hence revealing the *LWC*-plot, it is easy to compare *LWC* and video at each time-sample.

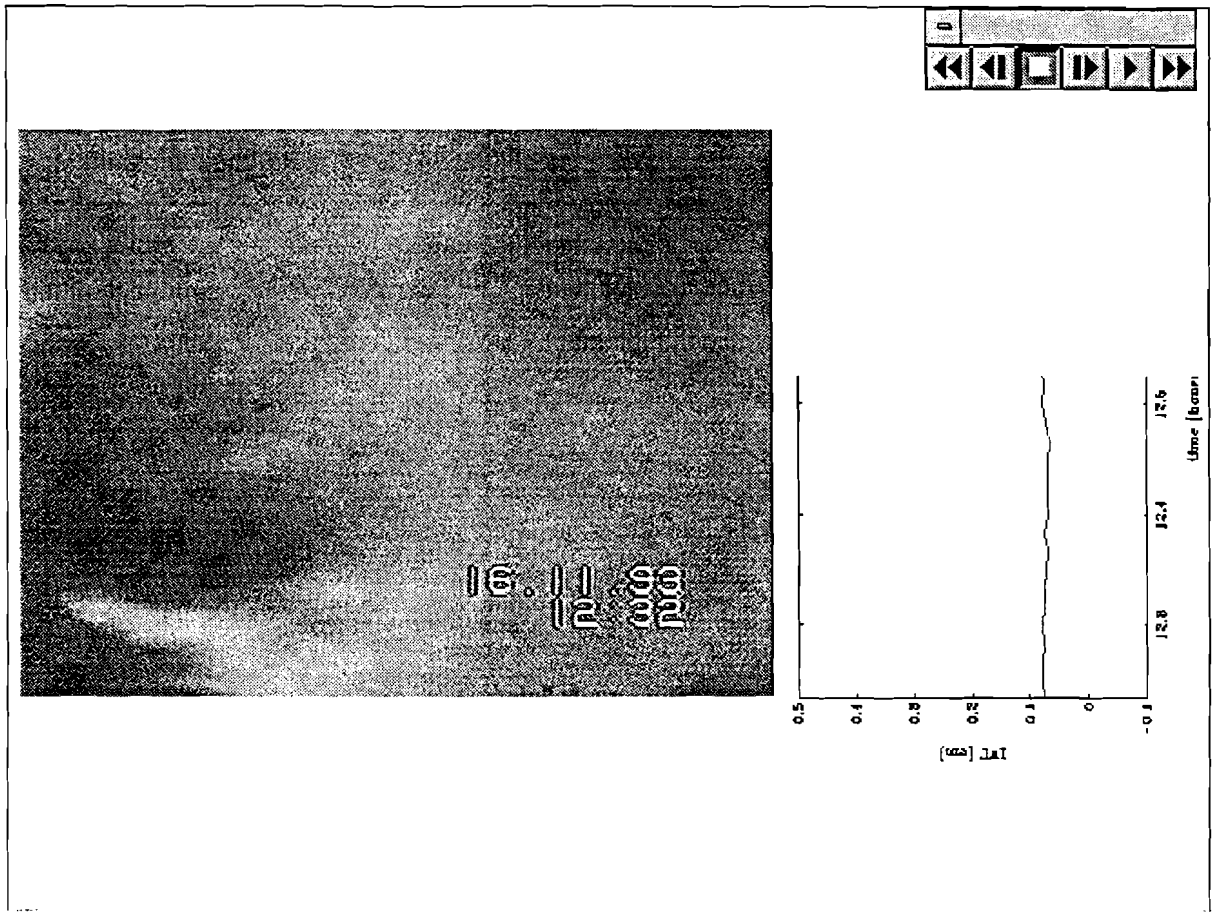

Figure 6.5: Screendump of presentation of video.

6.3 Conclusions

During the observtion period, inversion of radiometric data was not accurate. It was not possible to derive new correction factors ΔT_{20} and ΔT_{30} for the inversion algorithms during this period.

Comparing video observations with the inverted *LWC* gave no correlation. Little information could be retrieved from video observation of the clouds with maximum zoom of the camera lens. To obtain more cloud information zooming out is possible. In the latter case the quality of the digitized video is improved. But most times poor quality of the image was obtained.

Chapter seven
Conclusions and recommendations

7.1 Conclusions

An EUT inversion algorithm to retrieve both integrated water vapour and liquid water content from measured brightness temperatures at two frequencies was presented. In the computer programs used to compute the coefficients for this algorithm some errors were found. After optimizing the coefficients, correction factors were derived for the measures brightness temperatures to enhance the performance of the inversion algorithms. But these factors are only valid for radiometric data of the time before July 1993.

For three inversion algorithms correction factors were derived. This made clear that the EUT algorithm was not the best one. Most consistent results showed the DAPPER inversion algorithm. An algorithm of *Lavergnat* showed poor and inconsistent results for these correction factors. Because of the good results the DAPPER algorithm was used during further analysis.

The most important inaccuracy due in the used propagation models, is the cloud temperature. Also the antenna pattern should be known accurately.

The liquid water content inverted from radiometric data is due to the occurence of clouds. An overview showed the highly varying nature of clouds. To compare the inversion with actual atmospheric conditions a video observations were carried out. However, experiments showed no appreciable correlation between observations and liquid water content.

The digitized video of these observations were of moderate quality. The comparison was further complicated by inaccurate operation of the radiometer system. It was impossible to derive new correction factors to eliminate inaccuracies in the measured brightness temperatures.

With an increased camera lens view more information about the nature of the clouds observed can be obtained. It will generally improve the quality of the captured video.

7.2 Recommendations

The observations suffered from the fact that at the edges of most clouds the liquid water density is rather low and difficult to determine with the radiometer. When liquid water was detected, the video recordings gave no information, just a grey image.

More observations, however, may give a more satisfying result. Because of the weather conditions during the observations, there was a low number of possible events. Because of the weather, in the summer more clouds of interest occur. Using filters for the camera lens, it should be possible to enhance the contrast of the recorded images.

One of the factors of importance for correct inversion is the antenna factor h of both frequency channels. These factors are not known accurate. Well determined value will certainly improve the conversion of antenna noise temperature to sky noise temperature.

A more senstive radiometer, sensitive espacially for liquid water, is another possibility to improve the accuracy of the inversion. But note that optimal sets of frequencies for *IWV* retrieval are in general different from the optimal ones for *LWC* retrieval. With a frequency channel around 40/50 [GHz], the temperature profile can be estimated. [*Schiavon*] proved that the inclusion of meteorological data at ground level into the inversion algorithm yields only a moderate improvement in the performance of a dual-channel radiometer. The improvement is lower than the one attainable by the addition of an appropriate third radiometric channel in the oxygen complex frequency region.

Perhaps a statistical approach is a better method to analyse the performance of the inversion of liquid water. Statistics of the occurrence of cloud types and their base and top heights, may give more reliable information. Video observations with a large camera lens beam width can be used to determine actual dimensions (estimated) and cloud type, to be used with the statistics. As a consequence the quality of the captured video will be improved. For this purpose it is recommended also to use an even more powerful (faster) computer system if really a large number of events are captured. At this moment during the capturing, the capturing program (VidCap) uses all available capacity of the computer. Saving and compressing captured video frames takes very much computation time and harddisk space. A reliable backup system is necessary too, as it did not operated correct.

References

Action! v2.5 User Guide, San Francisco (Ca.): Macromedia, 1992, 1st ed.

Byers, H.R., *General meteorology*. 4th ed., New york: McGraw-Hill, 1974.

CCIR Report 563-4, *Radiometeorological data*, Reports of the CCIR, ITU, Vol. 5, 1988.

CCIR Report 719-3, *Attenuation by atmospheric gases*, Reports of the CCIR, ITU, Annex to Vol. 5, 1990.

Cotton, R.C. and R.A. Anthes, *Storm and cloud dynamics*. San Diego: Academic Press ,1989. International Geophysic series: 44.

Derr, V.E. et al, *A parameterization for the shortwave transmittivity of stratiform water clouds based on empirical data and radiative transfer theory*. Journal of the Atmospheric Sciences, Vol. 47 (1990), no. 23, p. 2774-2783.

Dijk, J. et al., *The Olympus radiometer for 12/20/30 GHz at Eindhoven University of Technology*. Proc. of European Microwave Conference 1991, Stutgart, p. 974-979.

Elgered, J. et al., *Measurements of atmospheric water vapor with microwave radiometry*. Radio Science, Vol. 17 (1982), no. 5, p. 1258-1264.

Explorer Camcorders Operating instructions for the VKR9000, Philips.

Franssen, L.J.J.C., *Linear inversion methods in radiometry*. Eindhoven University of Technology, Faculty of Electrical Engineering, Telecommunications Division, Sept. 1992, M. Sc. Thesis.

Guiraud, F.O. et al., *A dual channel microwave radiometer for measurements of precipitable water vapor and liquid*. IEEE Transactions on Geoscience Electronics, Vol. 17 (1979), no. 4, p. 129-136.

Können, G.P. et al., *Het weer in Nederland* (in Dutch). Zutphen: W.J. Thieme, 1983.

Lavergnat, J. et al., *Retrieval of atmospheric water from ground-based radiometry*, Proc. of Olympus Utilisation Conference 1993, Sevilla, p. 595-602.

Liebe, H.J., *Mpm - an atmospheric millimeter-wave propagation model*. International Journal of Infrared and Millimeter Waves, Vol. 10 (1989), no. 6, p. 631-650.

Slobin, S.D., *Microwave noise temperature and attenuation of clouds: Statistics of these effects at various sites in the United States, Alaska, and Hawaii*. Radio Science, Vol. 17 (1982), no. 6, p. 1443-1454.

Schaefer, V.J. et al, *A field guide to the atmosphere.* Boston: Houghton Mifflin, 1981. The Peterson field guide series: 26.

Schiavon, G. and D. Solimini, *Performance analysis of a multifrequency radiometer for predicting atmospheric propagation parameters*, Radio Science, Vol. 28 (1993), no.1, p. 63-76.

Staelin, D.H., *Measurements and interpretation of the microwave spectrum of the terrestrial atmosphere near 1-centimeter wavelength.* Journal of Geophysical Research, Vol. 71 (1966), no. 12, p. 2875-2881.

Video for Windows v1.0 User's Guide, Microsoft, 1992.

VideoBlaster User Reference Manual, Creative Labs, 1992.

Westwater, E.R., *The accuracy of water vapor and liquid water determination by dual-frequency ground-based microwave radiometry.* Radio Science, Vol. 13 (1978), no. 4, p. 677-685.

Westwater, E.R. et al, *Ground-based radiometric observations of atmospheric emission and attenuation at 20.6, 31.65, and 90.0 GHz: A comparison of measurements and theory.* IEEE Transactions on Antennas and Propagation, Vol. 38 (1990), no. 10, p. 1569-1579.

Wu, S.C., *Optimum frequencies of a passive microwave radiometer for tropospheric path-length correction.* IEEE Transactions on Antennas and Propagation, Vol. AP-27 (1979), no. 2, p. 233-239.

Appendix A
The CCIR atmospheric model

A.1 Temperature and pressure

In the reference standard atmosphere, the temperature profile is divided into seven successive layers, given by the linear equation

$$T(h) = T_i + L_i \cdot (h - H_i) \qquad [K] \ , \tag{A.1}$$

where L_i is the temperature gradient of layer i starting at altitude H_i (Table A.1).

Table A.1: Temperature gradients, L_i.

i	H_i [km]	L_i [K/km]
0	0	-6.5
1	11	0.0
2	20	+1.0
3	32	+2.8
4	47	0.0
5	51	-2.8
6	71	-2.0
7	85	

When the temperature gradient $L_i \neq 0$, pressure is given by the equation

$$P(h) = P_i \cdot \left(\frac{T_i}{T_i + L_i \cdot (h - H_i)} \right)^{\left(\frac{34.163}{L_i} \right)} \qquad [hPa] \ . \tag{A.2}$$

When the temperature gradient $L_i = 0$, pressure is obtained from

$$P(h) = P_i \cdot \left(\frac{-34.163 \cdot (h - H_i)}{T_i} \right) \qquad [hPa] \ . \tag{A.3}$$

The ground-level standard temperature and pressure are:

$$\begin{aligned} T_0 &= 288.15 \quad [K] \\ P_0 &= 1013.25 \quad [hPa] \end{aligned} \tag{A.4}$$

A.2 Partial water vapour pressure

The distribution of water vapour in the atmosphere is generally highly variable, but might be approximated by

$$v(h) = v_0 \cdot e^{-\frac{h}{h_{sc}}} \tag{A.5}$$

and the standard ground-level water vapour density is v_0 = 7.5 [g/m^3]. The partial water vapour pressure is obtained from the density using

$$e(h) = \frac{v(h) \cdot T(h)}{216.7} \quad . \tag{A.6}$$

Water vapour density decreases exponentially with increasing altitude, up to an altitude where the mixing ratio $e(h)/P(h) = 2 \cdot 10^{-6}$, and is constant at that value at higher altitude.

With a scale height of 2 [km] for the water vapour distribution and integrating (A.5) up to 30 [km] the integrated water vapour can be approximated. For zenith angle:

$$IWV = \frac{1}{a_w} \int_0^{30} v(h) \cdot e^{-\frac{h}{h_{sc}}} dh \quad , \tag{A.7}$$

where $v(h)$ is in [kg/m^2] and a_w is the specific weight of water, =10^6 [g/m^3]. So it follows for the integrated water vapour, with respect to unit area,

$$\begin{aligned} IWV &= \frac{1}{a_w} \cdot (-2 \cdot v_0) \cdot (e^{-\frac{30}{2}} - 1) \\ &\approx 2 \cdot 10^{-3} \cdot v_0 \quad [m] \\ &= 0.2 \cdot v_0 \quad [cm] \quad . \end{aligned} \tag{A.8}$$

A.3 Liquid water content

A similar expression as (A.8) can be derived for the liquid water content (zenith angle):

$$LWC = \frac{1}{a_w}\int_{h_b}^{h_t} l(h)\,dh$$
$$= 0.1 \cdot l \cdot (h_t - h_b) \qquad [cm] \ , \tag{A.9}$$

where a uniform cloud distribution ($l(h) = l = constant$ [g/m^3]) is assumed. h_t and h_b are the cloud top and cloud bottom heights in [km].

A.4 Other meteorological quantities[A1)]

The water vapour saturation pressure e_s, the pressure at which water vapour will be saturated at a certain temperature, is expressed as

$$e_s = 6.1121 \cdot \exp\left(\frac{17.502 \cdot t}{t + 240.97}\right) \qquad [mbar] \ , \tag{A.10}$$

where t is the temperature in [°C]. The relative humidity RH can be expressed as a function of both e and e_s:

$$RH = 100 \cdot \frac{e}{e_s} \qquad [\%].$$

Another usefull quantity is the water vapour density extracted from the water vapour pressure and the temperature

$$v = 216.7 \cdot \frac{e}{T} \qquad [g/m^3] \ ,$$

where T in [K].

[A1)] [CCIR, 1988].

Appendix B
Cloud types overview

B.1 Classification according to WMO

Meteorologists all over the world organized in the WMO (World Meteorological Organization) have drawn up an uniform system of cloud classification. The atmosphere is devided in three 'étages', defined by the height where the clouds are present. The three types are:

1: Cirrus, Cirrocumulus, Cirrostratus; upper étage.
2: Altocumulus; middle étage.
3: Stratocumulus, Stratus; lowest étage.

Altostatus resides usually at the middle étage, but occurs often at higher altitudes. Nimbostratus resides at the middle étage, but generally extends to the other étages. Cumulus and cumulonimbus have their base at the lowest étage, but the top is often in one of the other étages. The altitude of the étages are given in Table B.1 for different sites.

Table B.1: Étages definition.

	Polar region	Mid.-latitude	Tropics
upper	3-8 km.	5-13 km.	6-18 km.
middle	2-4 km.	2-7 km.	2-8 km.
lower	0-2 km.	0-2 km.	0-2 km.

WMO based the classification on ten main groups, genera. Some of these genera are divided in sub-groups, species, based on the shape of the clouds or their internal structure. Following is a summary of the ten genera type of clouds. For each type of cloud first the definitions of the 1956 World Meteorological Organization International Reduced Cloud Atlas is given. Further for each cloud type some additional information is given.

Only the species of cumulus type clouds are of interest. This cloud type frequently occur and has a significant liquid water content. At the end of the paragraph these species are given.

Cirrus (Ci)

Detached clouds in the form of white, delicate filaments or white or mostly white patches or narrow bands. These clouds have a fibrous (hair-like) appearance, or a silky sheen, or both.

Cirrus clouds exists at great heights and are mostly bright. They are composed of ice crystals. A variety of forms is seen. Tufts, delicate lines across blue sky, curved lines ending in tufts, branching plumes and just unshaded white smears against blue sky. Cirrus elements are sometimes ordened in wide parallel bands, appearing to converge to one point at the horizon. The sun is shining through the cirrus clouds most times, but obscurence of the sun is possible.

Cirrocumulus (Cc)

Thin, white patch, sheet or layer of cloud without shading, composed of very small elements in the form of grains, ripples, etc., merged or seperated, and more or less regularly arranged; most of the elements have an apparent width of less than one degree[B1)].

Cirrocumulus is mostly composed of ice crystals. Some strongly undercooled liquid water droplets may exist, but they usually transform to ice. Cirrocumulus is often connected to cirrus or cirrostratus, but often less frequently than those clouds. They looklike small flakes or very small globular masses. Usually cirrocumulus appear in more or less wide fields of very small elements in the form of grains, ripples, etc. Sometimes these fields have fibrous-like edges. Banks of cirrocumulus occur in the form of lenses or almonds, mostly sharp-edged and elongated. Cirrocumulus is thin enough to determine the place of the sun.

Cirrostratus (Cs)

Transparent, whitish cloud veil of fibrous (hair-like) or smooth appearance, totally or partly covering the sky, and generally producing halo phenomena.

Cirrostratus is composed mainly of ice crystals. Cirrostratus does have larger horizontal extend then cirrus. The border of the sheet of cirrostratus is usually indefinite, some times ending in patches of cirrus or cirrocumulus. No characteristic forms are noted as with altocumulus. Sometimes the cirrostratus is so thin that it is hardly visual, only a slightly whitens of the blue sky is noted. Or its presence can only be determined by halo-phenomena. At other times it has the appearance of a heavy white sheet.

Altocumulus (Ac)

White or grey, or both white and grey, patch, sheet or layer of cloud, generally with shading composed of laminae, rounded masses, rolls, etc., which are sometimes partly fibrous or diffuse and which may or may not be merged; most of the regularly arranged small elements usual have an apparent width of between one and five degrees[B2)].

B1) This can be approximated by the apparent thickness of the little finger at one armlength.

B2) This is approximated by the apparent thickness of three fingers at one armlength.

Altocumulus clouds are often composed of liquid droplets undercooled to temperatures below freezing. At even lower temperatures ice crystals may occur. Altocumulus appears most times as a layer or as extended banks, composed of a regularly arranged cloud elements. At the edges of the cloud elements bright plays of colors may be observed, specific for this type of clouds. Because altocumulus cloud elements have shading underneath and are larger than cirrocumulus, they are distinguishable from each other. The shapes of both cloud-types are quite similar. Often altocumulus occurs at two or more levels at the same time. The transparancy of altocumulusclouds variates widely. Sometimes the place of the sun can be detected, at other times not at all. The base of altocumulus clouds has often a regular relief. Altocumulus may represent a dissipating stage of altostratus.

Altostratus (As)

Greyish or bluish cloud sheet or layer of striated, fibrous, or uniform appearance, totally or partly covering the sky, and having parts thin enough to reveal the sun at least vaguely as through ground glass. Altostratus does not produce halo phenomena.

Altostratus is composed of liquid water droplets, ice crystals, rain drops and snowflakes. Altostratus is characterized by both large horizontal and vertical extend, hundreds of kilometers respectively a few thousand meters. As altocumulus altostratus can exists at two or more layers. Altostratus does never show definite configurations, but it is sometimes thin in light patches between very dark parts. Shadows of objects on the ground are not visible if altostratus is present. Lower altostratus may be distinguished from stratus or nimbostratus by the more darker, more uniform gray of the cloud and the fibrous structure with whitish gleam. If the sun is totally obscured, i.e. the position can not be defined, it is likely that the sheet is stratus or nimbostratus. Altostratus clouds do have precipitation, which does not have to reach ground level.

Nimbostratus (Nb)

Gray cloud layer, often dark, the appearance of which is rendered diffuse by more or less continuously falling rain or snow, which in most cases reaches the ground. It is thick enough to completely obscure the sun. Low, ragged clouds frequently occur below the layer.

Nimbostratus is composed of liquid water droplets (sometimes undercooled) and raindrops, snow-crystals and -flakes, or a composition of liquid and solid water elements. By evaporating in the air, the precipitation does not have to reach the ground. This causes the cloud to be wet-look. In storms scud clouds underneath nimbostratus are often present. Nimbostratus is most often at low altitudes. Because it has no discrete or somewhat regular cloud elements it is distinguishable from stratocumulus and from stratus because it is darker, showing most times precipitation.

Stratocumulus (Sc)

Gray or whitish, or both gray and whitish, patch, sheet or layer of cloud which almost always has dark parts, composed of crenellations, rounded masses, rolls, etc., which are non-fibrous and which may or may not be merged; most of the regularly arranged small elements have an apparent width of more than five degrees.

Stratocumulus clouds are composed of water droplets, sometimes with raindrops or snowgrains. Most times stratocumulus has the form of a layer or a bank, composed of elements like those of altocumulus, but at lower levels. Thereby they seem to be larger. The arrangement of stratocumulus cloud elements are in groups, lines or waves, aligned in one or two directions. Stratocumulus in

general cause a large extended cloud cover. Often several stratocumulus layers are observed at two or more levels. Sometimes stratocumulus has some precipitation in the form of rain, snow or snowgrains.

Stratus (St)

Generally gray cloud layer with a fairly uniform base, which may gave drizzle, ice prisms or snow grains. If the sun is visible through the cloud, its outline is clearly discernible. Stratus does not produce halo phenomena except, possibly, at very low temperatures. Sometimes stratus appears in the form of ragged patches.

Stratus is usually composed of liquid water droplets. At lower temperatures little ice parts may exist in the cloud. Densed stratus clouds contain often droplets of drizzle and sometimes ice prisms or snowgrains. In his most general form stratus occur as a misty greyish and rather regular layer. The clouds base is at such low altitudes that the top of buildings and hills are in the cloud. Stratus has always a uniform top, usually marked by a temperature inversion or another thermally stable layer. Stratus can have the same characteristics as fog, but it does not occur on the ground. The cloud could be so thin that sun or moon may be visible, sharp-edged. But it is more likely that they are not visible at all due to the cloud. Precipitation of stratus clouds which reach the ground level is falling in the form of drizzle, ice prisms or snow grains.

Cumulus (Cu)

Detached clouds, in general dense and sharp edged, which develope vertically in forms of mounds, domes or towers of which the upper bulging part often looklikes a cauliflower. The sunlighted parts of these clouds are most times dazzling white; their base is relatively dark and practically horizontal. Sometimes cumulus are ragged.

Cumulus is mainly composed of lquid water droplets. In those parts of the cloud where the temperature is definite below 0°C ice crystals may be present. By their vertical extend cumulus can be devided in three classes (species). The clouds with the smallest dimensions look flattened or do have strongly frayed edges and a continuously changing outline. Clouds of the middle class have smaller bulges, while clouds with the largest dimensions have a strongly bulging top which looklikes a cauliflower. These three cumulus cloud forms can exist at the same time. Cumulus clouds with considerable vertical extend may show sometimes some precipitation.

Cumulonimbus (Cb)

Heavy, dense cloud with a considerable vertical extend, in the form of a mountian or huge towers. Its upperside is usually, at least partly, striated or fibrous-like or uniform appearance, and is almost always flattened; this part spreads out in the form of an anvil or a wide plume. Underneath the base of the cloud, which is generally very dark, frequently low ragged clouds occur, which may or may not merge, and sometimes virga are noted.

Cumulonimbus is composed of liquid water droplets and, mainly in the upper part, of ice crystals. Also large raindrops occur and often snowflocs, snow grains, hail grains and hail. The liquid water droplets and raindrops may be strongly undercooled. Because the horizontal and vertical dimensions of the cloud are that large, the characteristic form of cumulonimbus can only be observed at large distances. Cumulonimbus clouds may occur isolated or in a sequence, which look like a very long wall. Sometimes cumulonimbus is situated totally inside a cloud mass of altostratus or nimbostratus. The

dark, threatening or even terrifying impression which cumulonimbus can give, is usually enlarged by the thunder and lightning, heavy rain and hail and by blasts of wind.

Species of Cumulus

Cumulus humilis: Cumulus clouds of only a slight vertical extent. They generally appear flattened.

Cumulus mediocris: Cumulus clouds of moderate vertical extent. the tops of which show fairly small protuburances.

Cumulus congestus: Cumulus clouds which exhibit markedly vertical developments and are often of great vertical extent. Their bulging upper part frequently resembles a cauliflower.

B.2 Classification by way of formation

Another way of classification is to devide the clouds by the way of formation of the cloud. Several kind of clouds dissolve in the course of day, like stratus and stratocumulus. Others preferably are formed afternoon, like cumulus and cumulonimbus do. [*Können*] devided the above discussed clouds by way of formation.

A: Cirrostratus, altostratus, nimbostratus:
Weak upward movement of air over a large area.

B: Cirrocumulus,altocumulus,stratocumulus:
Weak upward movement of air in thin layers, which will order in isolated areas with alternately upwards and downwards air current.

C: Cumulus:
Strong upward movement over small areas in thick layers.

D: Cumulonimbus:
Very strong upward movement over a small area in very thick layers, often extending to the tropopause.

E: Cirrus, altocumulus:
By turbulence due to friction of the wind against the earth surface.

F: Stratocumulus, stratus, fog:
By mixing of moist air layers with different temperatures.

G: Altocumulus in the morning:
By nightly cooling of the higher air layers due to radiation.

H: Fog, stratus, stratocumulus:
By cooling of the lowest air layer from the ground.

B.3 Determination

In Figures B.1, B.2 and B.3 for the three étages a way for determinations of what cloud is present is given. The étages are indicated by C_L, C_M and C_H, respectively the lower, the middle and the higher étage. Figure B.4 illustrates a plot of several cloud types in altitude.

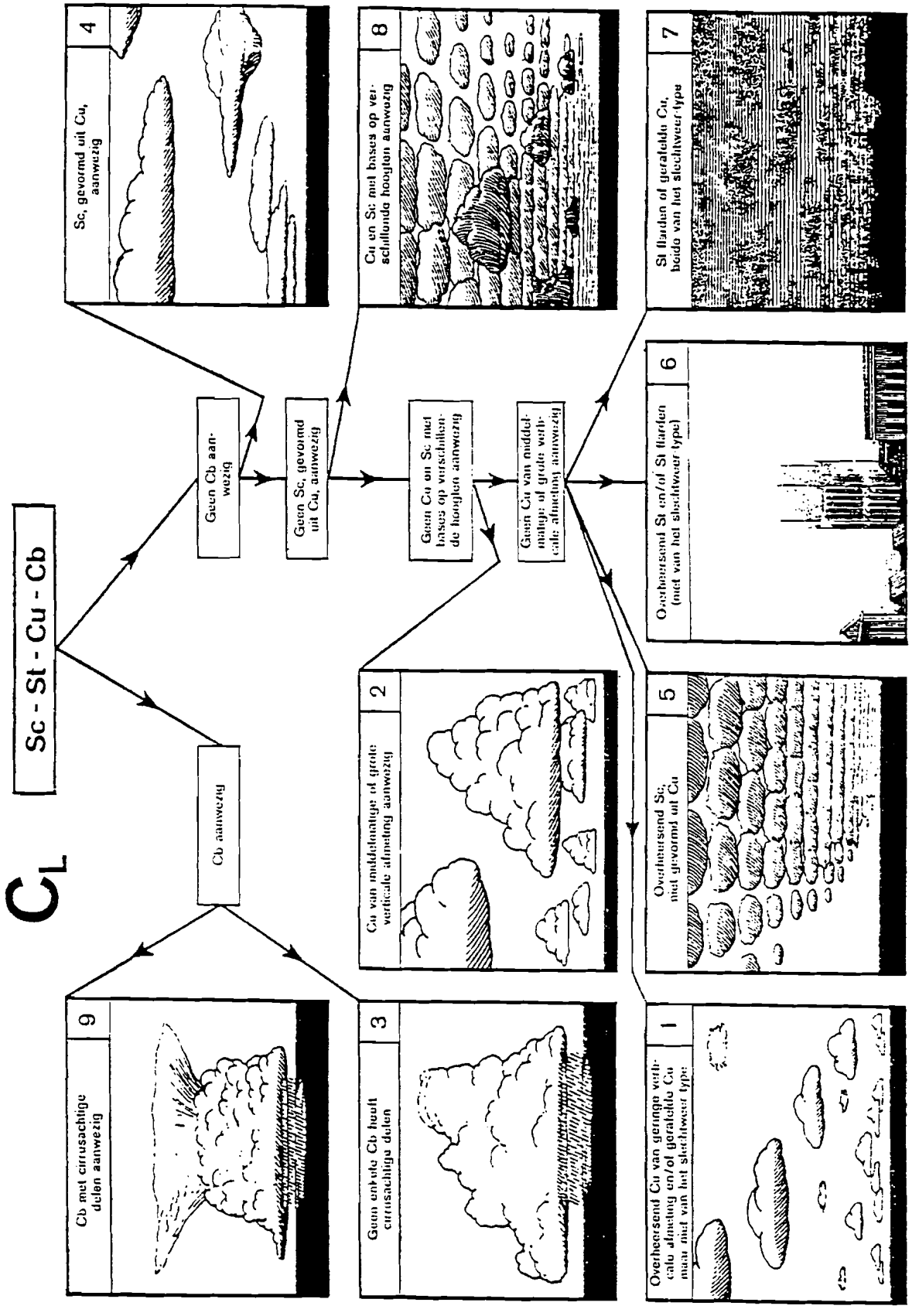

Figure B.1: Cloud determination, lower étage.

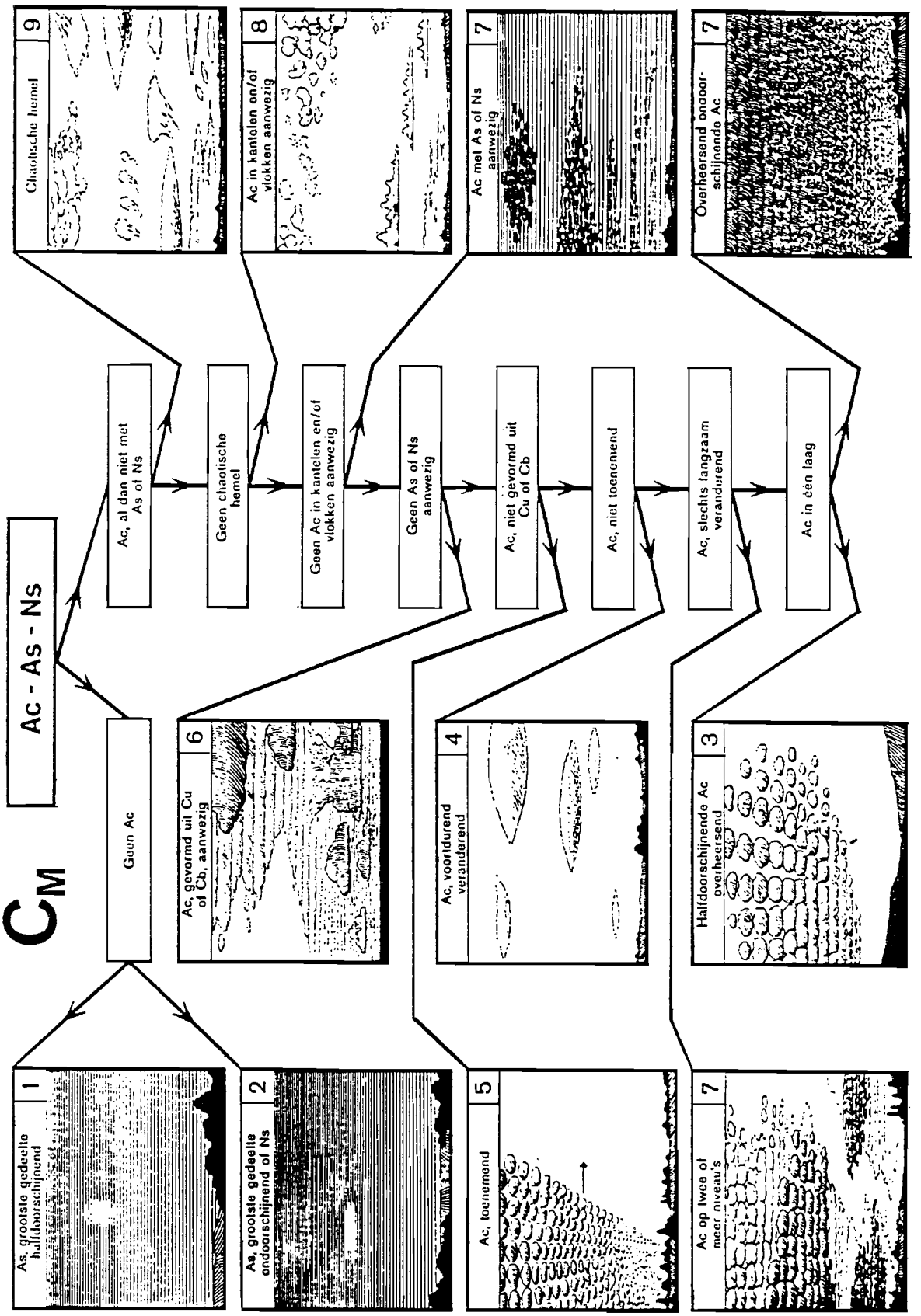

Figure B.2: Cloud determination, middle étage.

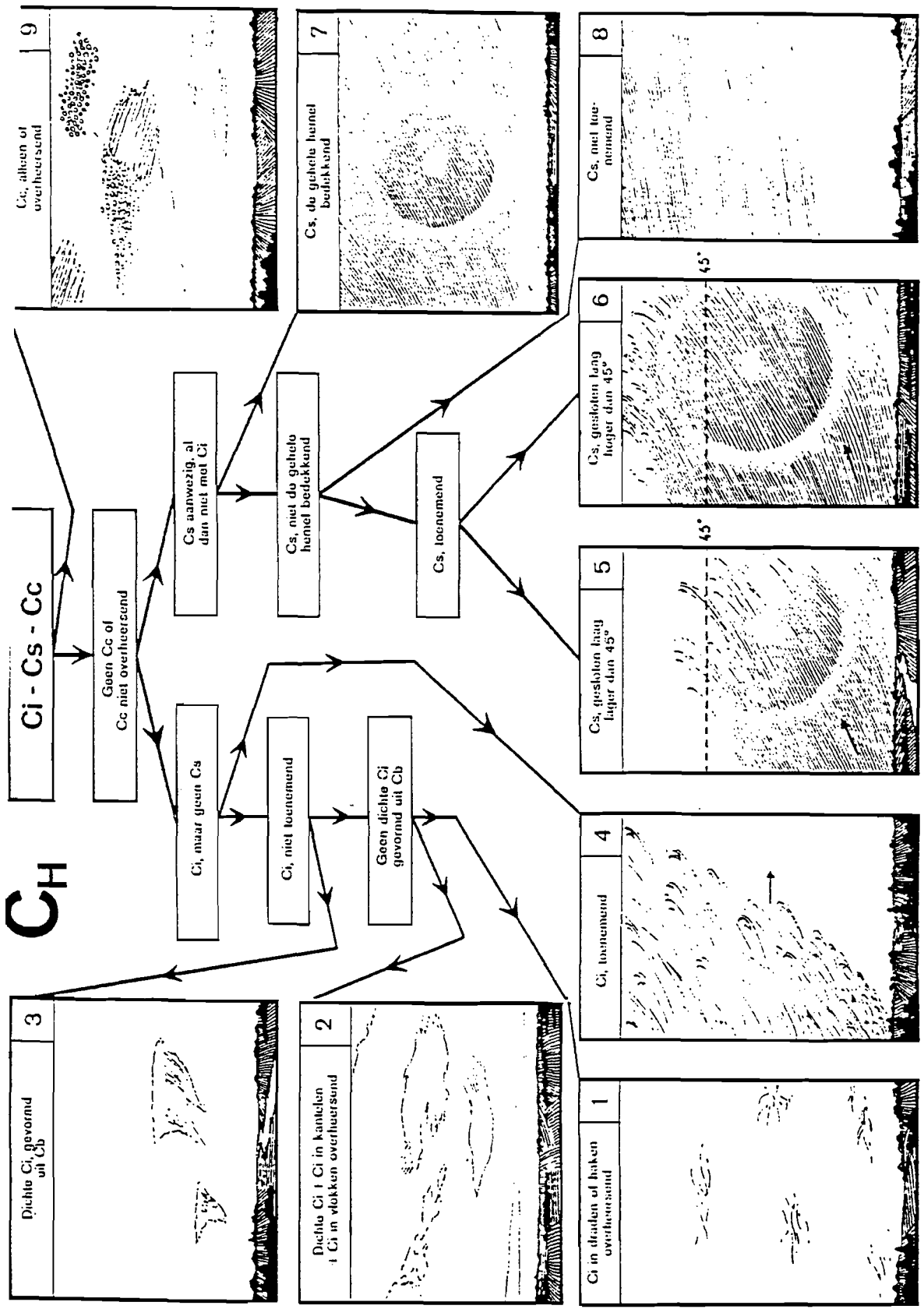

Figure B.3: Cloud determination, higher étage.

Figure B.4: Height overview of clouds.

Appendix C
Coefficients of eq. (3.18)

Table C.1: Coefficients c and d for winter period.

	EUT		DAPPER	
Day	c	d	c	d
Jan 03, 1992	0.3418	34.49	0.8194	17.08
Jan 07, 1992	0.3418	35.07	0.8182	18.36
Jan 10, 1992	0.3418	36.30	0.8218	18.01
Jan 11, 1992	0.3418	38.05	0.8138	16.89
Jan 14, 1992	0.3418	28.76	0.8280	16.85
Jan 17, 1992	0.3418	34.39	0.8169	17.01
Jan 21, 1992	0.3418	44.15	0.8163	25.46
Jan 22, 1992	0.3418	43.10	0.8182	25.39
Dec 24, 1991	0.3418	34.08	0.8176	17.28
Dec 26, 1991	0.3418	31.11	0.8241	17.46
Dec 31, 1991	0.3418	23.77	0.8247	12.06

Table C.2: Coefficients c and d for summer period.

	EUT		DAPPER	
Day	c	d	c	d
Jun 18, 1991	0.4901	21.47	0.8241	15.12
Jun 22, 1991	0.4901	22.12	0.8285	17.95
Jul 07, 1991	0.4901	15.31	0.8398	16.06
Jul 28, 1991	0.4901	26.37	0.8259	20.25
Jul 29, 1991	0.4901	25.04	0.8316	22.12
Jul 30, 1991	0.4901	21.49	0.8324	19.44

Appendix D
Event list

Next a list of events will be in a short form presented. After the date first four points concerning the recorded video are given. Than a point about the radiometer events followed by meteorological information. At last some remarks may be made. Explaination of meteorological codes and abbreviations used in this list are given in Appendix E.

Rec. time:	Total time of recording.
Time difference:	DAPPER time minus video camera time.
Video-events:	Time intervals in which a events takes place, at least on the video.
Captured-events:	Time interval of digitized video in which or video or radiometer events take place.
DAPPER-events:	Time intervals in which radiometer events take place.
Meteo:	Meteorological information distributed by the KNMI by teletext.
Remarks:	Points of interest.

Oct 05, 1993

Rec.time:	9:05:??-9:39:??
Time difference:	18 sec.
Video-events:	9:14-9:16 (wtc[D1)])
Captured events:	(oct0593.avi) 9:14:15-9:15:00
DAPPER-events:	9:26:35-9:27:49-9:29:11, 9:31:13-9:32:46
Meteo:	Dry, stratus-stratocumulus.
Remarks:	No correlation between Video and DAPPER, DAPPER events occur when clouds already cover the beam => cloud becomes thicker.

Oct 21, 1993

Rec.time:	9:07:??-9:27:??
Time difference:	40 sec.
Video-events:	9:07-9:10, 9:24-9:25 (wtc)
Captured events:	(oct2193a.avi) 9:07:59-9:10:00; (oct2193b.avi) 9:24:28-9:25:23
DAPPER-events:	
Meteo:	9:25:00, bewolking: sct035 sct050 bkn100 (3/8 Cu 2000feet locally 5/8 3000feet or higher. During showers 3/8 CB 1500feet, locally 3/8 around 800feet)
Remarks:	Now and then showers, recording stopped due to showers. No interesting events. Events a: no increase in LWC; event b: LWC decreases, but nothing happens on video.

[D1)] wtc = Without Time Correction.

Oct 25, 1993

Rec.time:	-
Time difference:	-
Video-events:	-
Captured events:	-
DAPPER-events:	
Meteo:	The whole day cloudy, but no precipitation. Cloud-type: strato-cumulus. (15:00-21:00, 2/8 2500ft and 7/8 3000ft or higher. South Limburg 3/8 1000ft and 5/8 around 1500ft. zero degree level: 4000ft, in the east above 8000ft. 1000ft: +8°; 2000ft: +5°; 5000ft: -1° (in the east +4°))
Remarks:	Because the whole day was cloudy of the same type no video recordings are made.

Oct 27, 1993

Rec.time:	10:03-10:34
Time difference:	56 sec.
Video-events:	10:06-10:09, 10:27-10:28, 10:30-10:31
Captured events:	(a): 10:27:08-10:28:33; (b): 10:30:38-10:31:28; (c): 10:06:49-10:08:44
DAPPER-events:	10:07-10:08; 10:27-10:28
Meteo:	Cloudy, now and then a piece of blue sky, and sometimes drizzle.
Remarks:	

Nov 02, 1993

Rec.time:	-
Time difference:	-
Video-events:	-
Captured events:	-
DAPPER-events:	
Meteo:	(sct065 sct070) At 1000vt inversion, stratus at 500-800vt. The whole day was a bit foggy or low stratus.
Remarks:	Because the whole day was cloudy of the same type no video recordings are made.

Nov 04, 1993

Rec.time:	-
Time difference:	-
Video-events:	-
Captured events:	-
DAPPER-events:	
Meteo:	sct120, clear sky (At 1000ft inversion, warm, moist air with some field of middle clouds. 1000ft: +13°, 2000ft: +11°, 5000ft: +9°)
Remarks:	Use as a reference event.

Nov 05, 1993

Rec.time:	-
Time difference:	-
Video-events:	-
Captured events:	-
DAPPER-events:	
Meteo:	skc, clear sky, moist air (1000ft: +12°, 2000ft: +10°, 5000ft: +5°)
Remarks:	Use as a reference event.

Nov 16, 1993

Rec.time:	12:14-12:45
Time difference:	1.58 min.
Video-events:	12:30-12:31
Captured events:	(a): 12:29:52-12:33:00; (b): 12:15-12:45 (1 min. samples)
DAPPER-events:	Non that reliable
Meteo:	bkn028 (2-8/8 sc above 2000ft. further locally 7/8 cirrus, 0°C level on 1200ft. 1000 ft: +0°C, 2000ft: -3°C, 5000ft: +0°C.)
Remarks:	

Nov 17, 1993

Rec.time:	
Video-events:	
Captured events:	
DAPPER-events:	
Meteo:	bkn220 (In South-East locally 6/8 around 3500ft, middle or higher cloud cover, 0°C level on 1500ft, between 3500 and 6500ft abovc zero. 1000ft: +1°C, 2000ft: -1°C, 5000ft: +2°C.)
Remarks:	Sun is almost shining in the camera lens, zoom was set to minimum, focus on infinity.

Appendix E
Meteorological codes

Next is a summary of the codes used by the KNMI and in the event list of Appendix D.

sct	scattered
bkn	broken
ovn	overcast
sct	1/8 - 4/8 [E1)]
bkn	5/8 - 7/8
ovn	8/8
cb	Cumulonimbus
tcu	Towering Cumulonimbus

base in hundreds of feets

000	<	100 ft
001		100 ft
002		200 ft
etc.		
050		5000 ft
060		6000 ft
etc.		
100		10000 ft
110		11000 ft
etc.		

VV...	vertical visibility in hundreds of feet
skc	sky clear
nsc	no significant clouds

[E1)] The sky covering by a certain cloud type is expressed in eights of the total visible hemisphere. 0/8 : no covering of sky by clouds; 8/8: sky totally covered by clouds

Appendix F
Brightness temperature versus water vapour density

Next, for both zenith looking and an elevation angle of 26.8° brightness temperature versus the water vapour density is plotted. The data is computed with the CCIR line-by-line propagation model.

Parameter *To* is the ground temperature. The groundtemperature is ranging from 35 [°C] decreasing with the in the Figures indicated stepsize.

F.1 For zenith looking

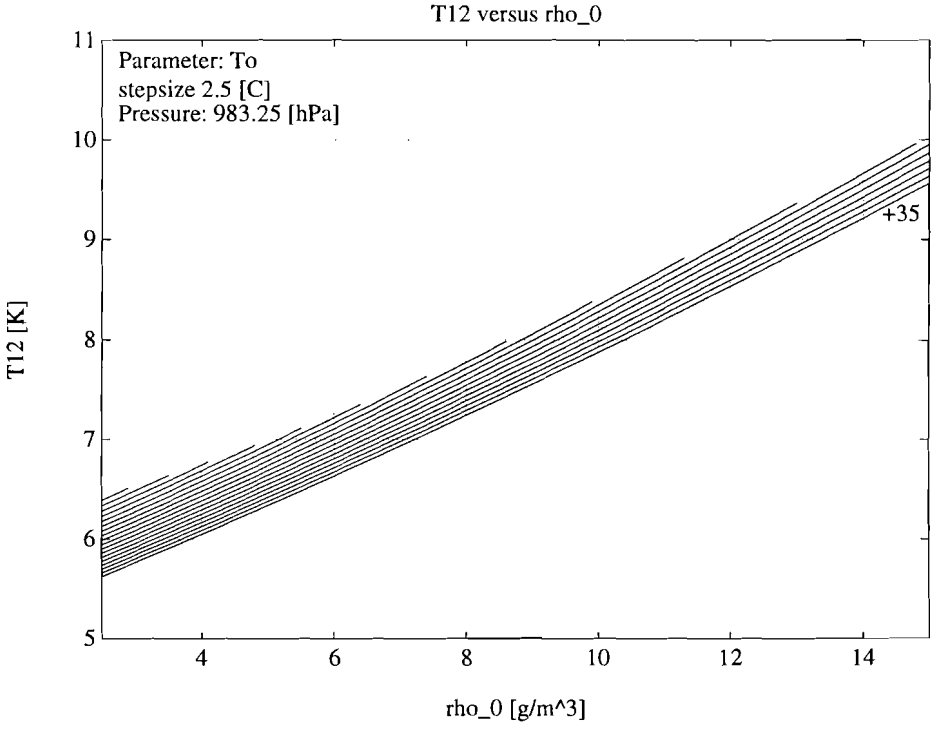

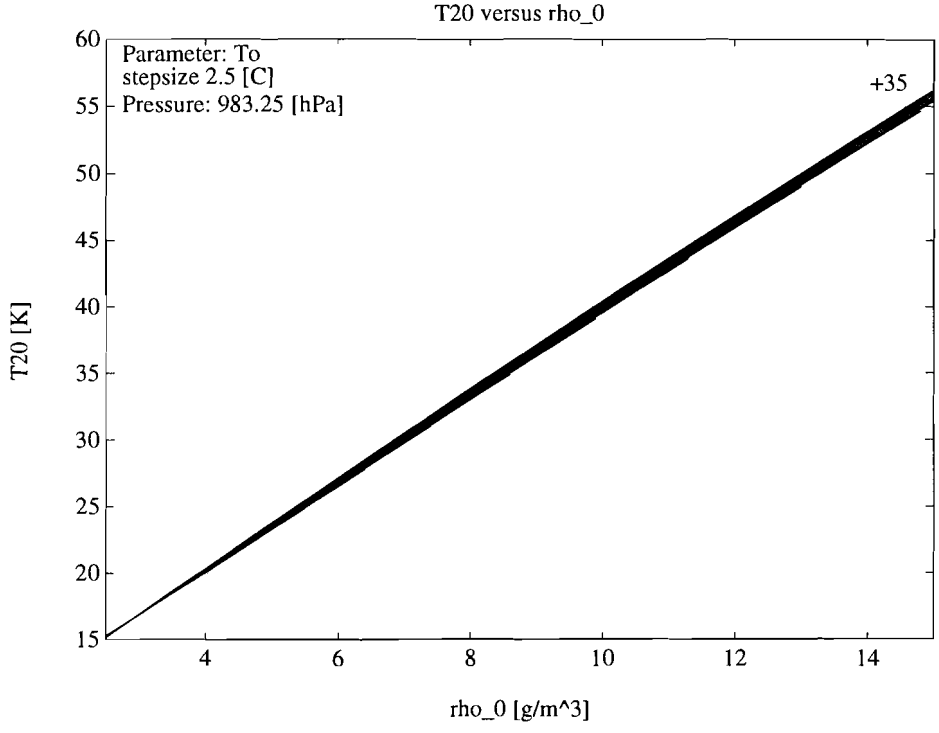
T20 versus rho_0
Parameter: To
stepsize 2.5 [C]
Pressure: 983.25 [hPa]
+35
T20 [K]
rho_0 [g/m^3]
60
55
50
45
40
35
30
25
20
15
4
6
8
10
12
14

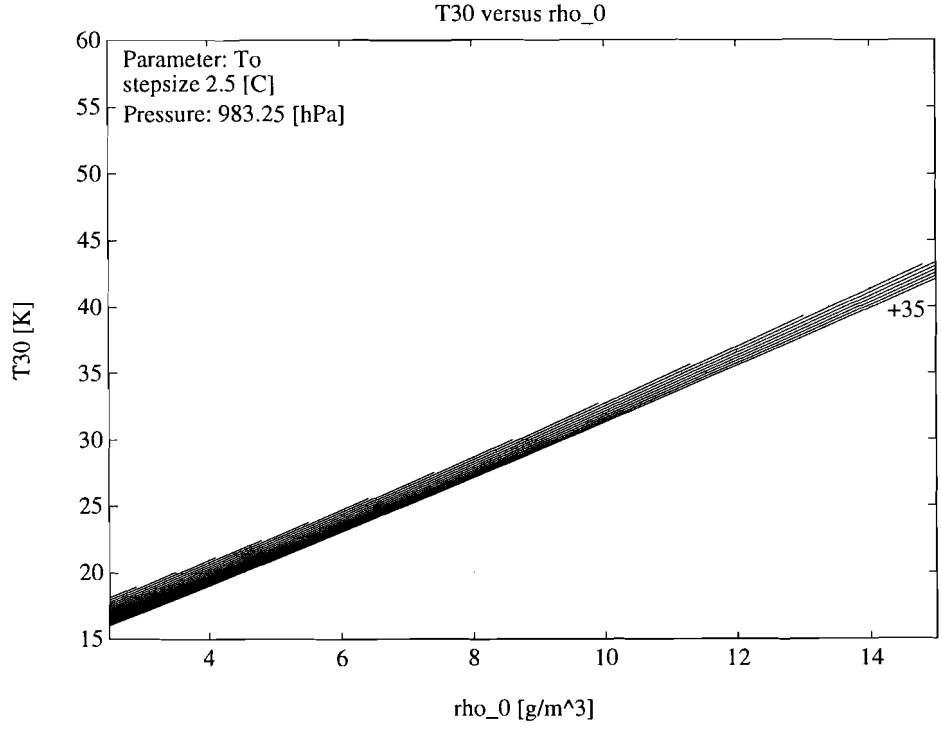
T30 versus rho_0
Parameter: To
stepsize 2.5 [C]
Pressure: 983.25 [hPa]
+35
T30 [K]
rho_0 [g/m^3]
60
55
50
45
40
35
30
25
20
15
4
6
8
10
12
14

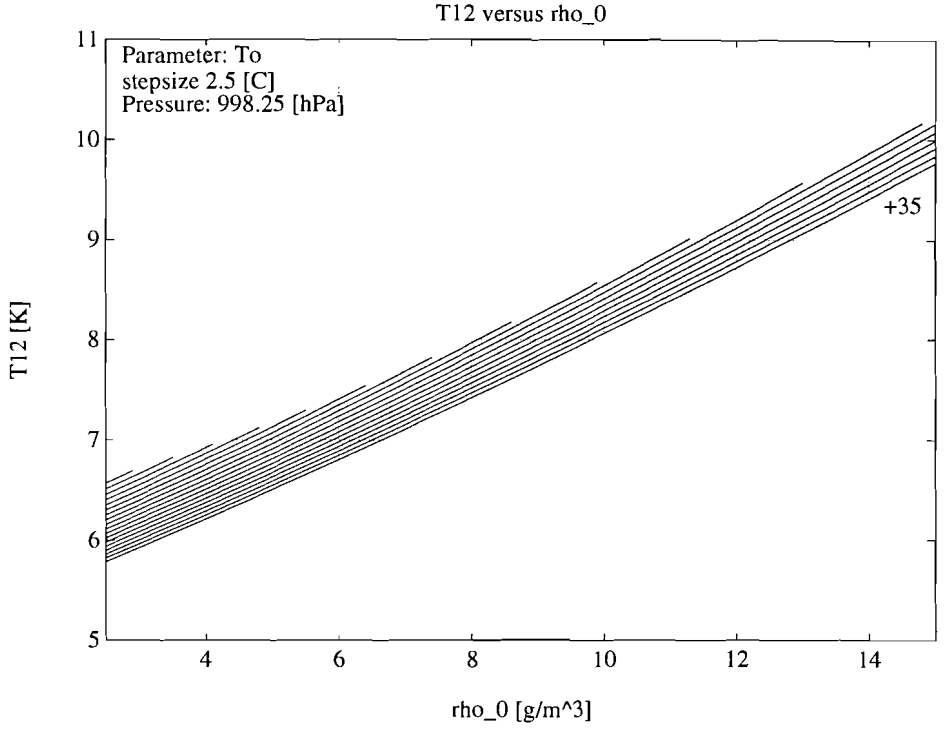
T12 versus rho_0
Parameter: To
stepsize 2.5 [C]
Pressure: 998.25 [hPa]
+35
T12 [K]
rho_0 [g/m^3]
11
10
9
8
7
6
5
4
6
8
10
12
14

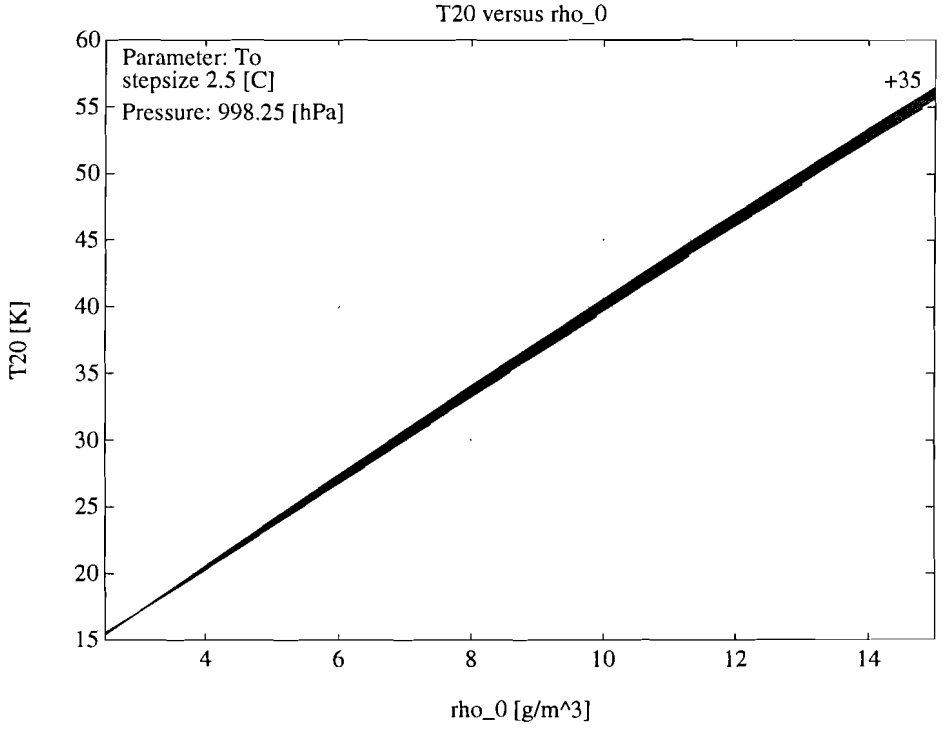
T20 versus rho_0
Parameter: To
stepsize 2.5 [C]
Pressure: 998.25 [hPa]
+35
T20 [K]
rho_0 [g/m^3]
60
55
50
45
40
35
30
25
20
15
4
6
8
10
12
14

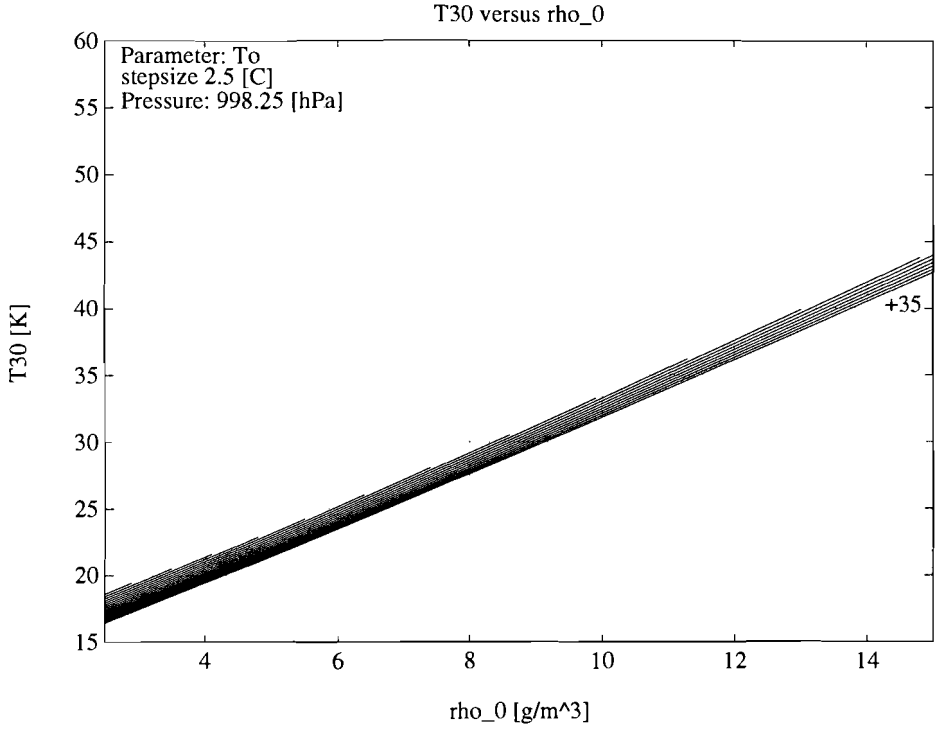
T30 versus rho_0
Parameter: To
stepsize 2.5 [C]
Pressure: 998.25 [hPa]
+35
T30 [K]
rho_0 [g/m^3]
60
55
50
45
40
35
30
25
20
15
4
6
8
10
12
14

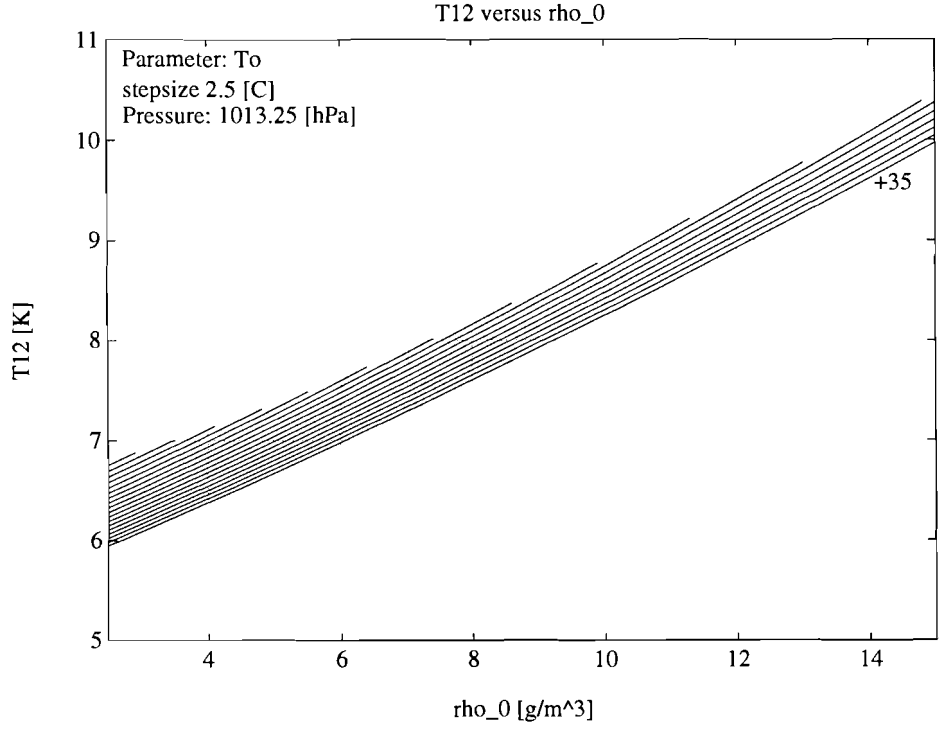
T12 versus rho_0
Parameter: To
stepsize 2.5 [C]
Pressure: 1013.25 [hPa]
+35
T12 [K]
rho_0 [g/m^3]
11
10
9
8
7
6
5
4
6
8
10
12
14

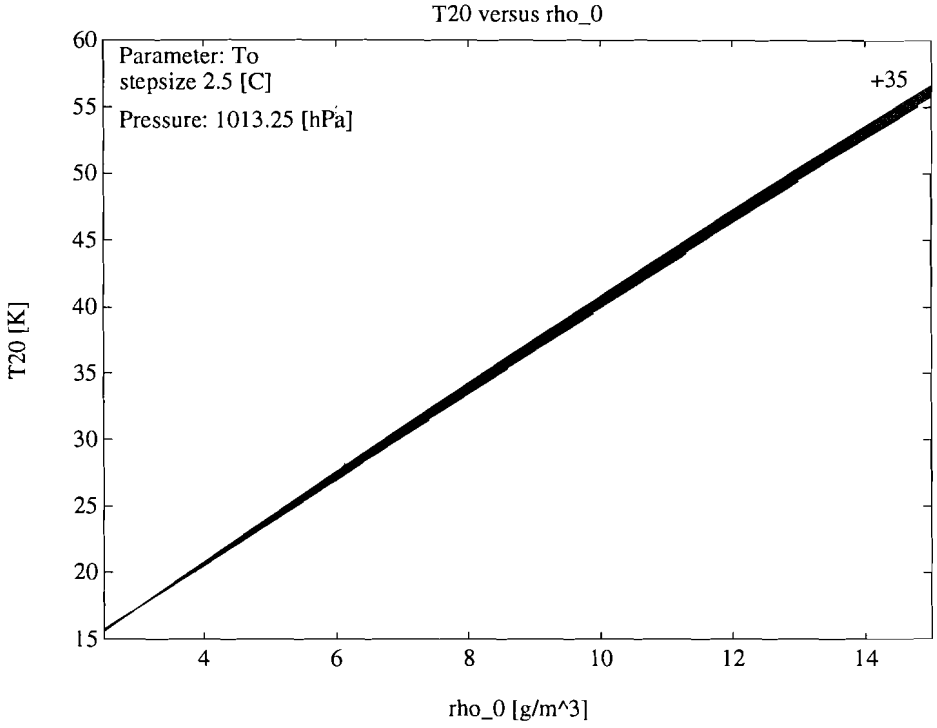
T20 versus rho_0
Parameter: To
stepsize 2.5 [C]
Pressure: 1013.25 [hPa]
+35
T20 [K]
rho_0 [g/m^3]
60
55
50
45
40
35
30
25
20
15
4
6
8
10
12
14

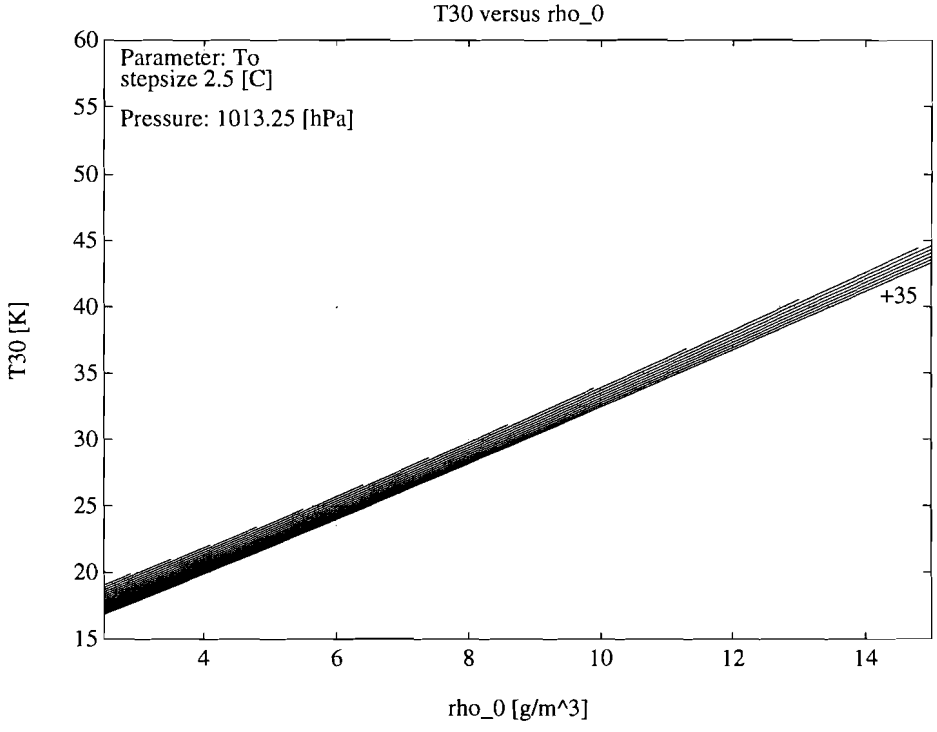
T30 versus rho_0
Parameter: To
stepsize 2.5 [C]
Pressure: 1013.25 [hPa]
+35
T30 [K]
rho_0 [g/m^3]
60
55
50
45
40
35
30
25
20
15
4
6
8
10
12
14

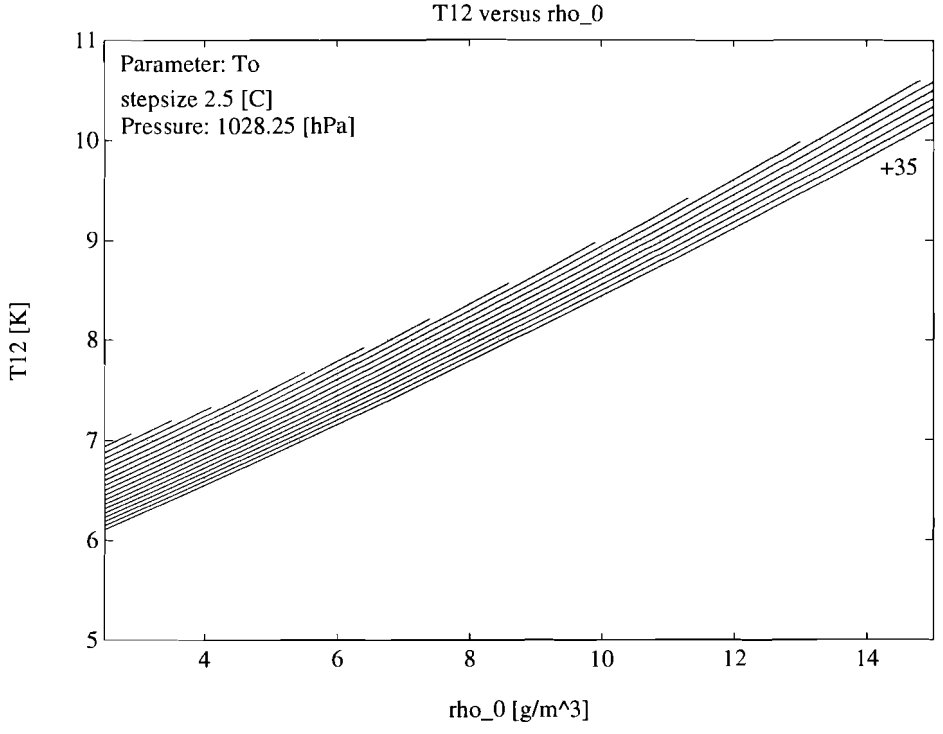
T12 versus rho_0
Parameter: To
stepsize 2.5 [C]
Pressure: 1028.25 [hPa]
+35
T12 [K]
rho_0 [g/m^3]
11
10
9
8
7
6
5
4
6
8
10
12
14

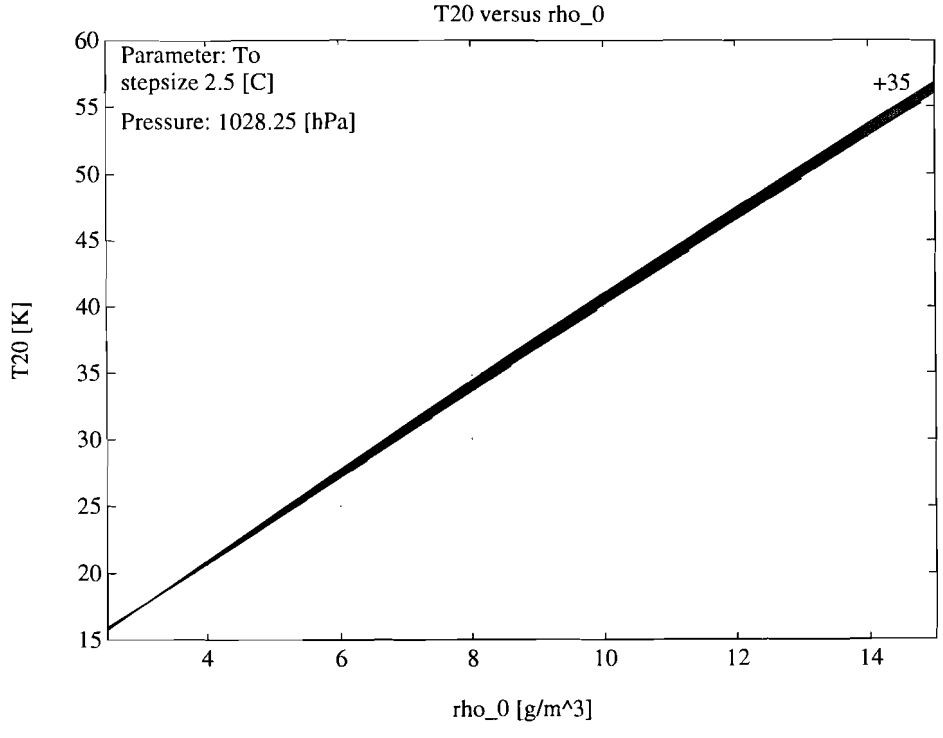
T20 versus rho_0
Parameter: To
stepsize 2.5 [C]
Pressure: 1028.25 [hPa]
+35
T20 [K]
rho_0 [g/m^3]
60
55
50
45
40
35
30
25
20
15
4
6
8
10
12
14

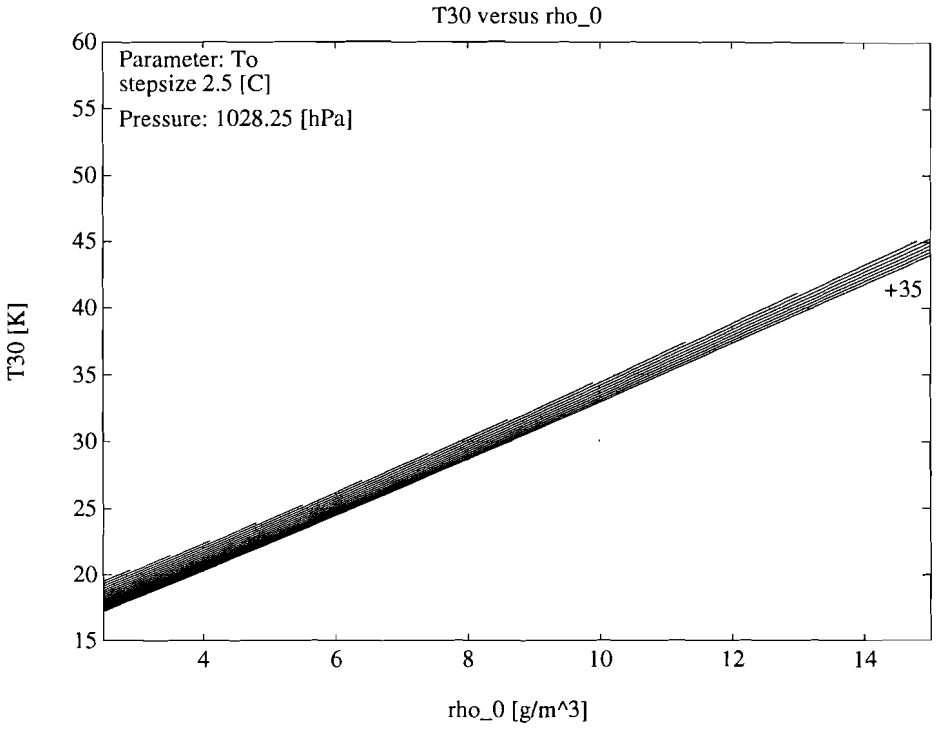
T30 versus rho_0
Parameter: To
stepsize 2.5 [C]
Pressure: 1028.25 [hPa]
+35
T30 [K]
rho_0 [g/m^3]
60
55
50
45
40
35
30
25
20
15
4
6
8
10
12
14

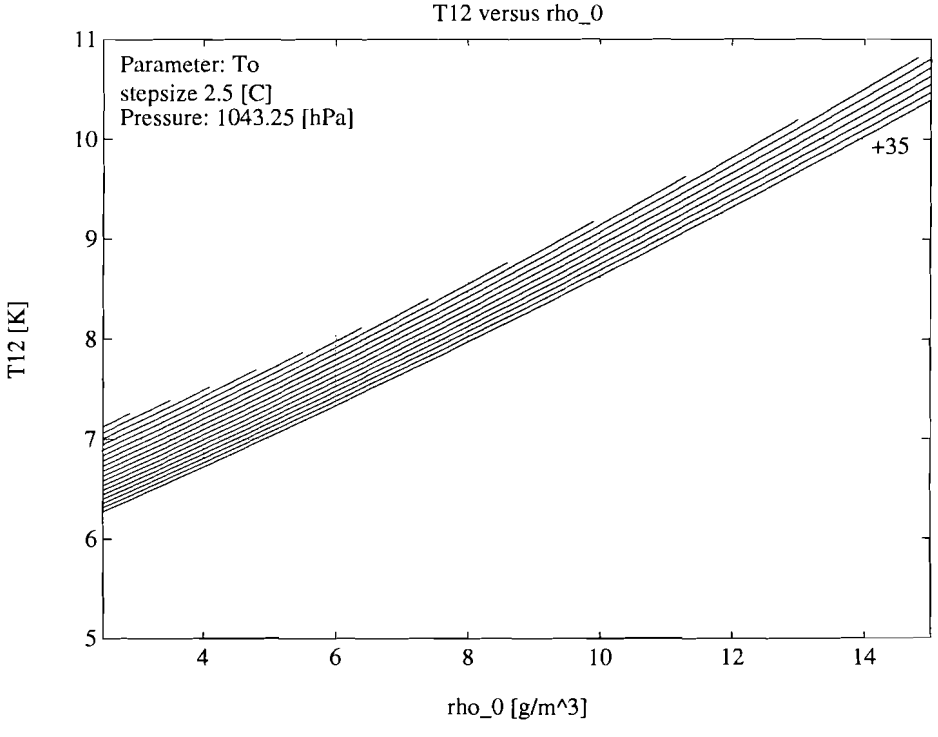
T12 versus rho_0
Parameter: To
stepsize 2.5 [C]
Pressure: 1043.25 [hPa]
+35
T12 [K]
rho_0 [g/m^3]
11
10
9
8
7
6
5
4
6
8
10
12
14

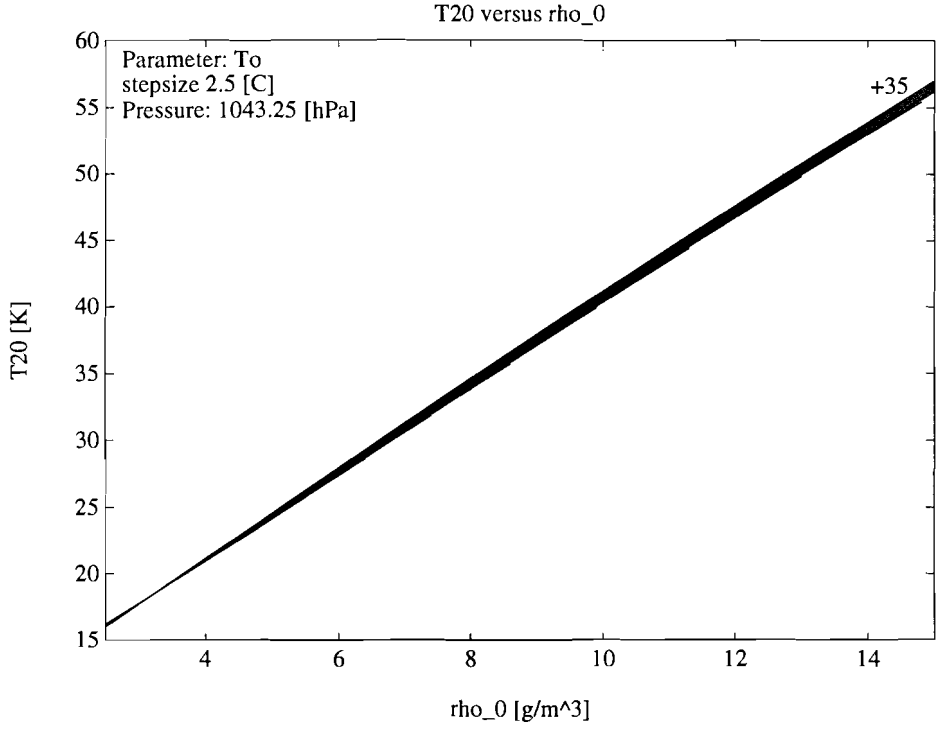
T20 versus rho_0
Parameter: To
stepsize 2.5 [C]
Pressure: 1043.25 [hPa]
+35
T20 [K]
rho_0 [g/m^3]
60
55
50
45
40
35
30
25
20
15
4
6
8
10
12
14

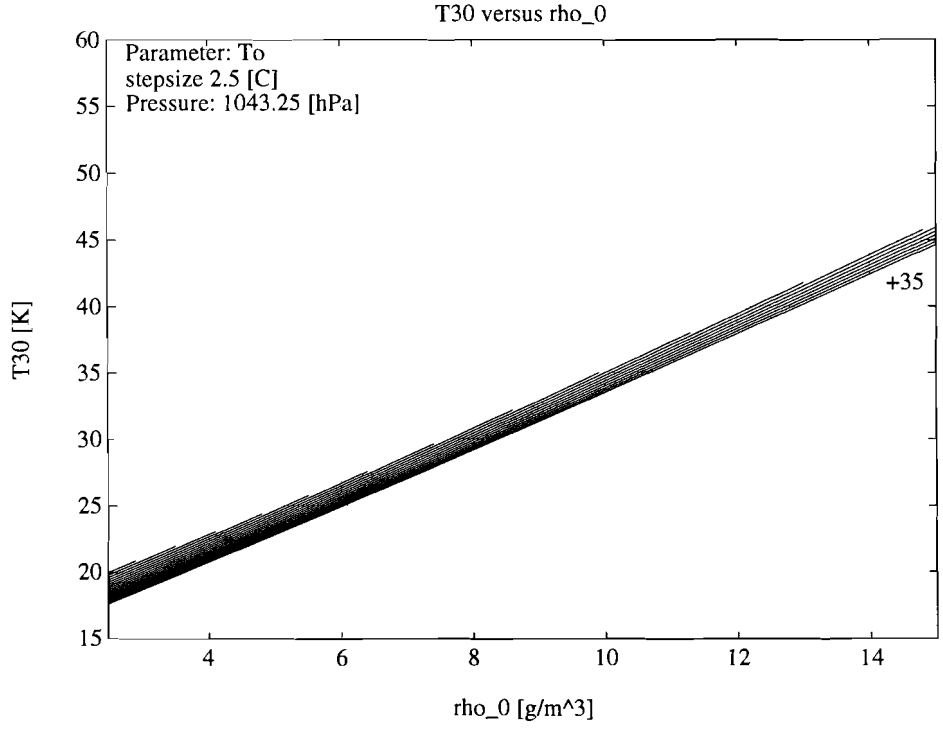
T30 versus rho_0
Parameter: To
stepsize 2.5 [C]
Pressure: 1043.25 [hPa]
+35
T30 [K]
rho_0 [g/m^3]
60
55
50
45
40
35
30
25
20
15
4
6
8
10
12
14

F.2 Elevation angle 26.8°

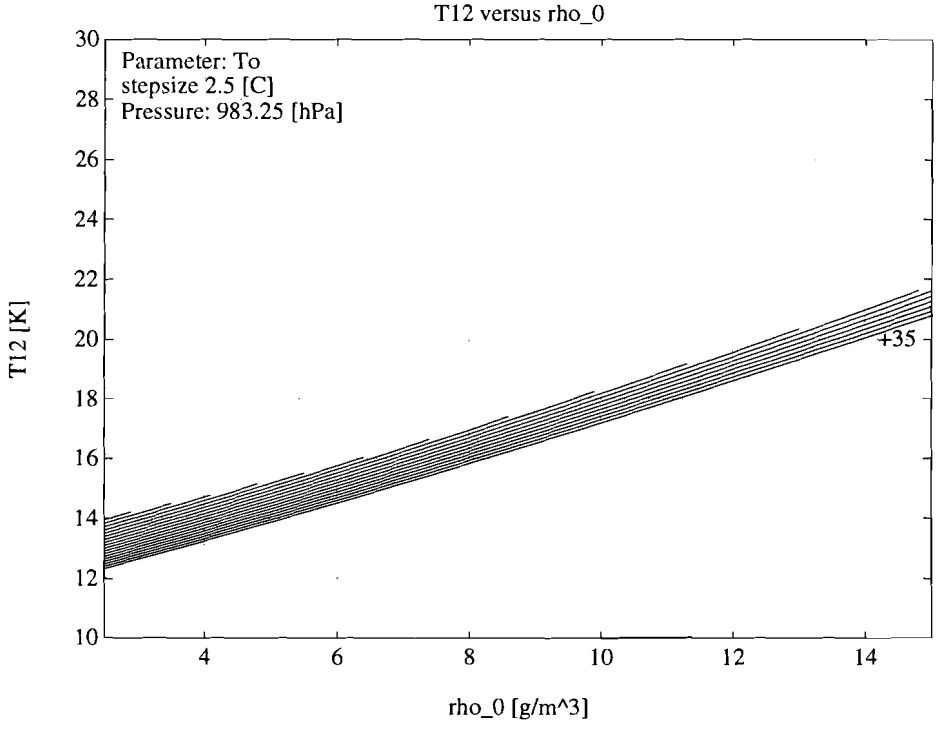

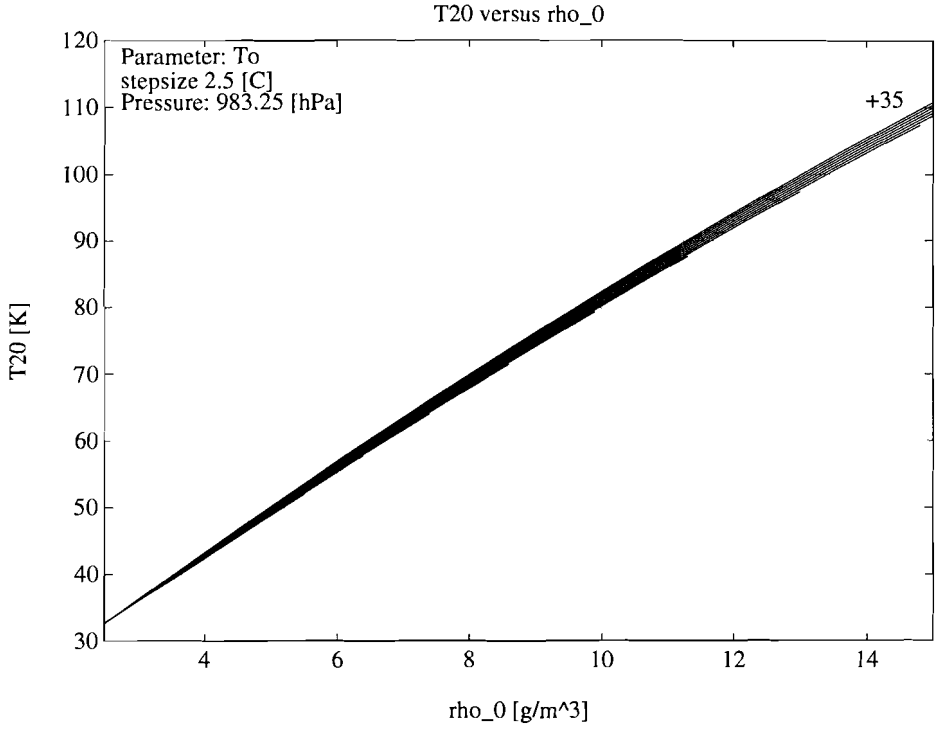
T20 versus rho_0
Parameter: To
stepsize 2.5 [C]
Pressure: 983.25 [hPa]
+35
T20 [K]
120
110
100
90
80
70
60
50
40
30
4
6
8
10
12
14
rho_0 [g/m^3]

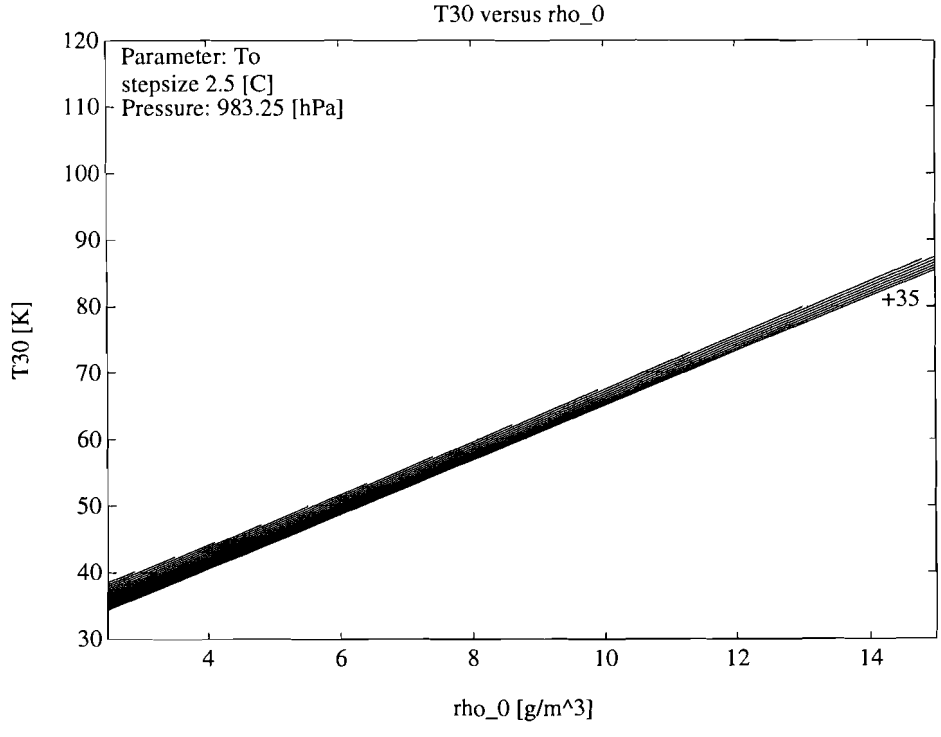
T30 versus rho_0
Parameter: To
stepsize 2.5 [C]
Pressure: 983.25 [hPa]
+35
T30 [K]
120
110
100
90
80
70
60
50
40
30
4
6
8
10
12
14
rho_0 [g/m^3]

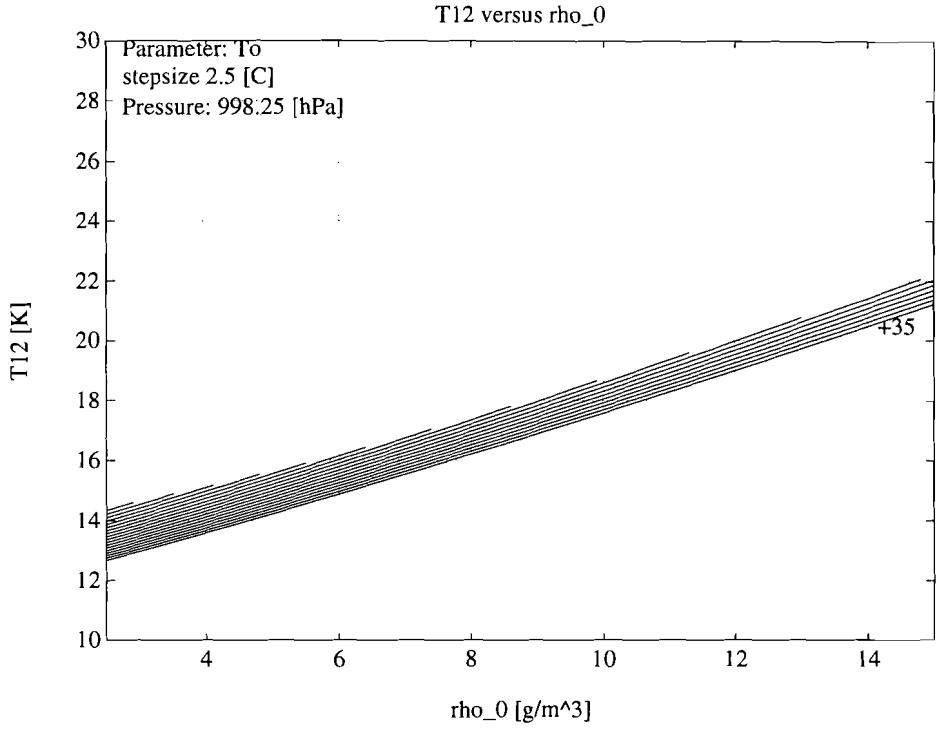
T12 versus rho_0
Parameter: To
stepsize 2.5 [C]
Pressure: 998.25 [hPa]
+35
T12 [K]
rho_0 [g/m^3]
30
28
26
24
22
20
18
16
14
12
10
4
6
8
10
12
14

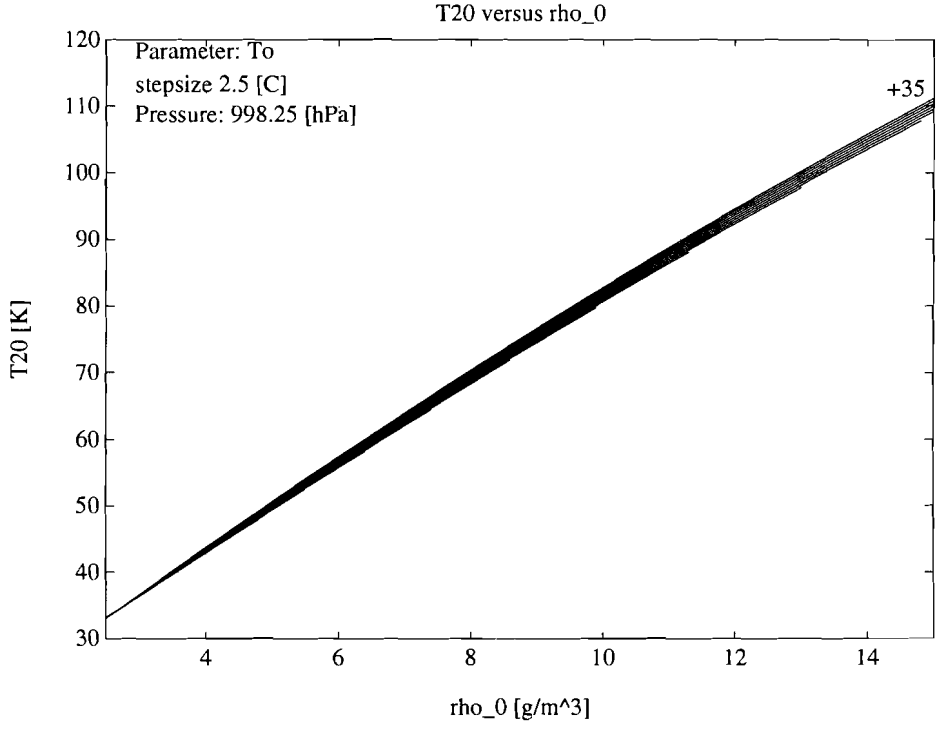
T20 versus rho_0
Parameter: To
stepsize 2.5 [C]
Pressure: 998.25 [hPa]
+35
T20 [K]
rho_0 [g/m^3]
120
110
100
90
80
70
60
50
40
30
4
6
8
10
12
14

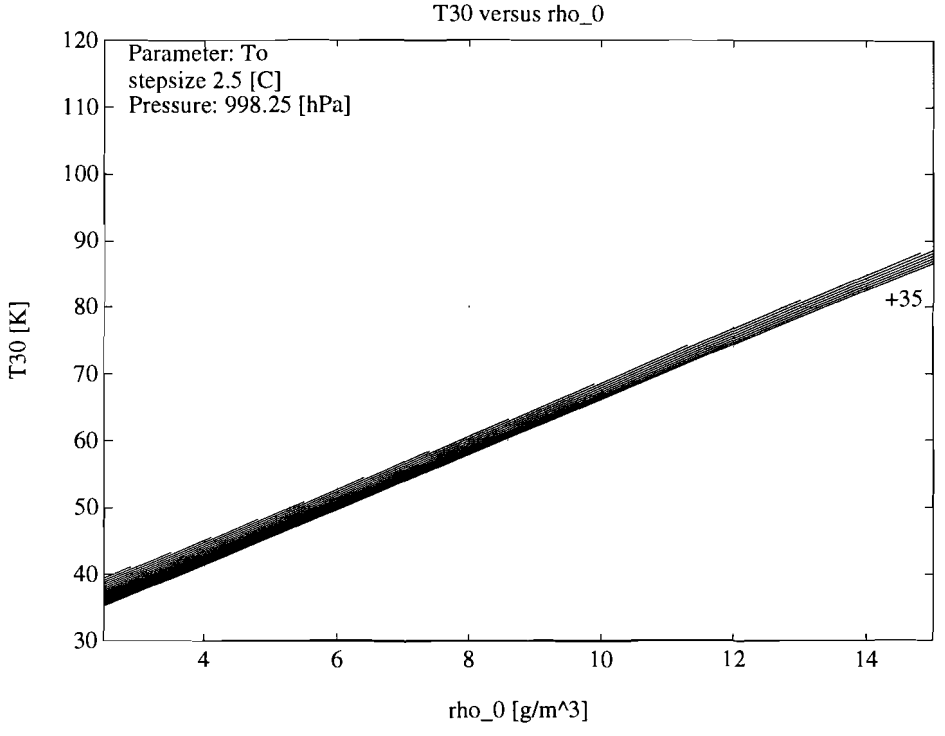
T30 versus rho_0
Parameter: To
stepsize 2.5 [C]
Pressure: 998.25 [hPa]
+35
T30 [K]
rho_0 [g/m^3]
120
110
100
90
80
70
60
50
40
30
4
6
8
10
12
14

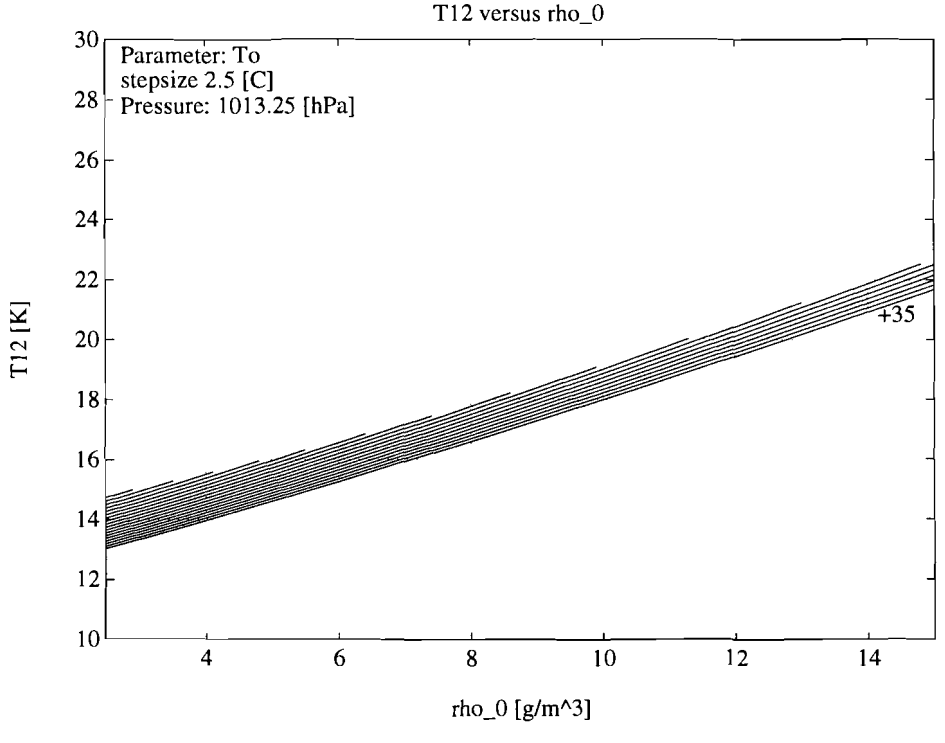
T12 versus rho_0
Parameter: To
stepsize 2.5 [C]
Pressure: 1013.25 [hPa]
+35
T12 [K]
rho_0 [g/m^3]
30
28
26
24
22
20
18
16
14
12
10
4
6
8
10
12
14

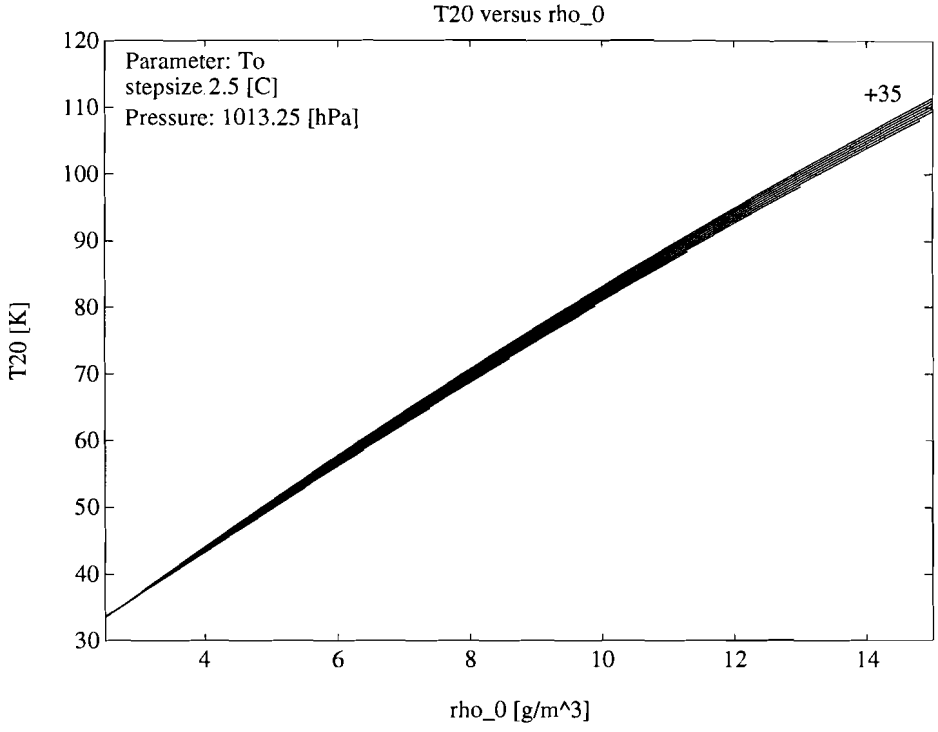
T20 versus rho_0
Parameter: To
stepsize 2.5 [C]
Pressure: 1013.25 [hPa]
+35
T20 [K]
rho_0 [g/m^3]
120
110
100
90
80
70
60
50
40
30
4
6
8
10
12
14

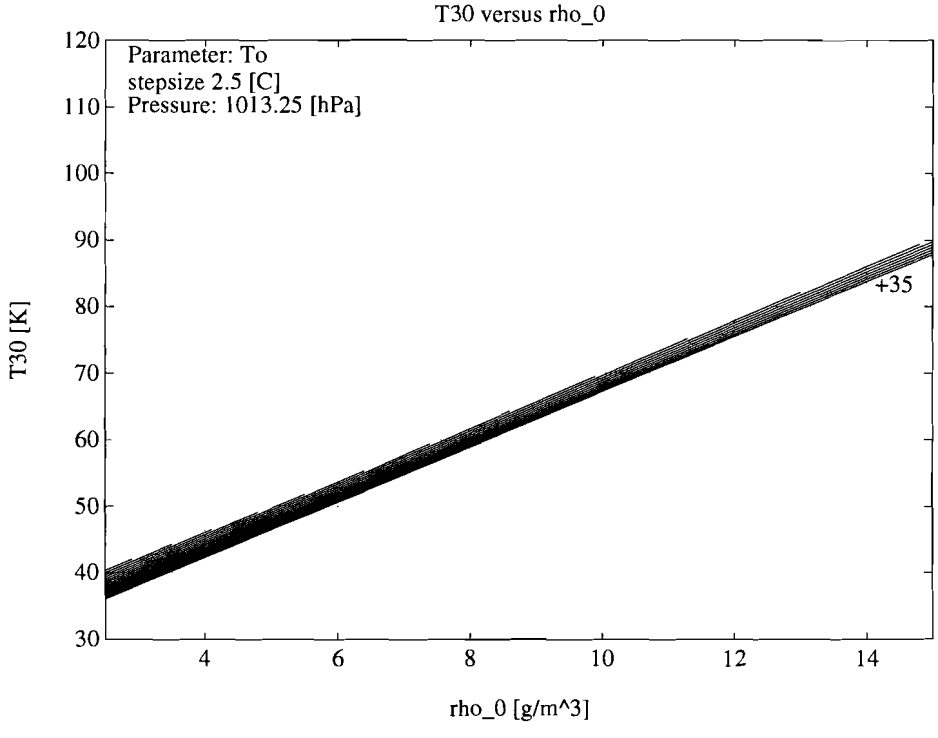
T30 versus rho_0
Parameter: To
stepsize 2.5 [C]
Pressure: 1013.25 [hPa]
+35
T30 [K]
rho_0 [g/m^3]
120
110
100
90
80
70
60
50
40
30
4
6
8
10
12
14

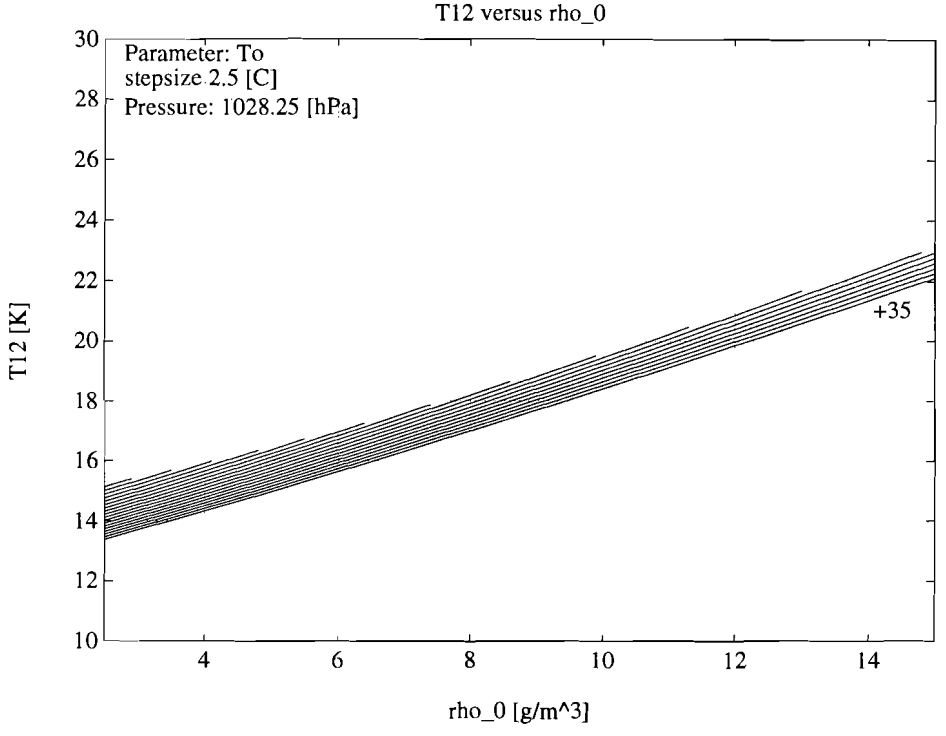
T12 versus rho_0
Parameter: To
stepsize 2.5 [C]
Pressure: 1028.25 [hPa]
+35
T12 [K]
rho_0 [g/m^3]
30
28
26
24
22
20
18
16
14
12
10
4
6
8
10
12
14

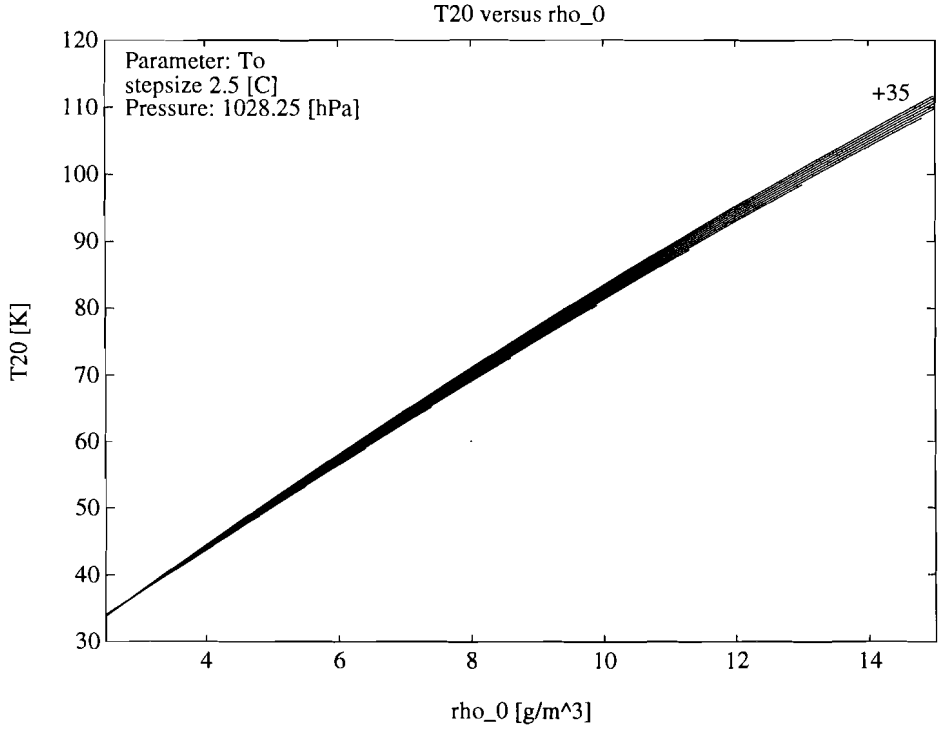
T20 versus rho_0
Parameter: To
stepsize 2.5 [C]
Pressure: 1028.25 [hPa]
+35
T20 [K]
rho_0 [g/m^3]
120
110
100
90
80
70
60
50
40
30
4
6
8
10
12
14

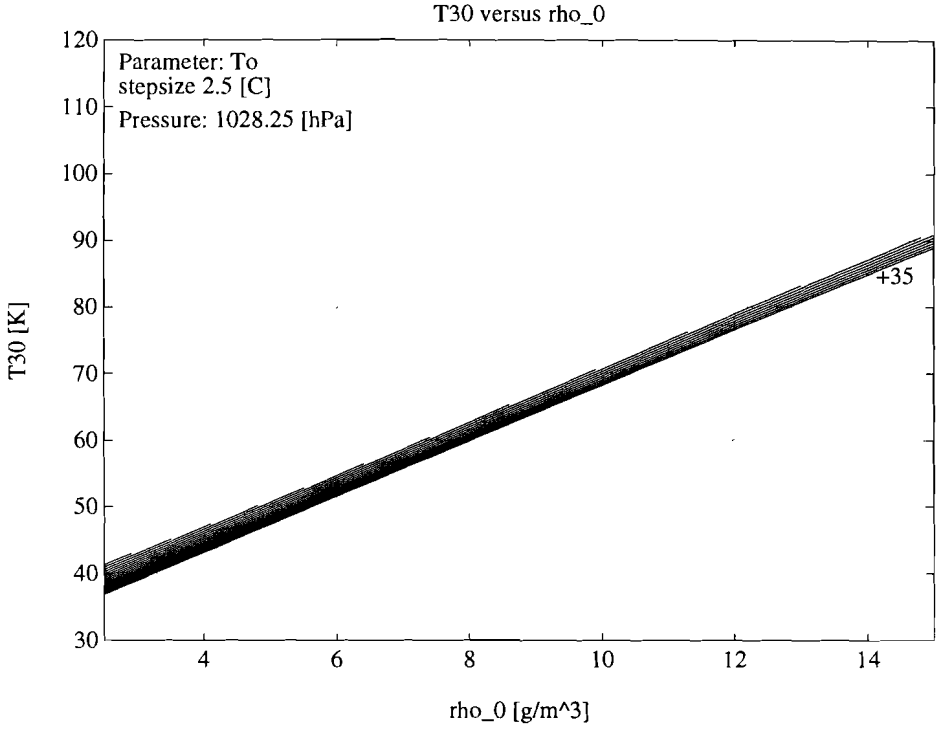
T30 versus rho_0
Parameter: To
stepsize 2.5 [C]
Pressure: 1028.25 [hPa]
+35
T30 [K]
rho_0 [g/m^3]
120
110
100
90
80
70
60
50
40
30
4
6
8
10
12
14

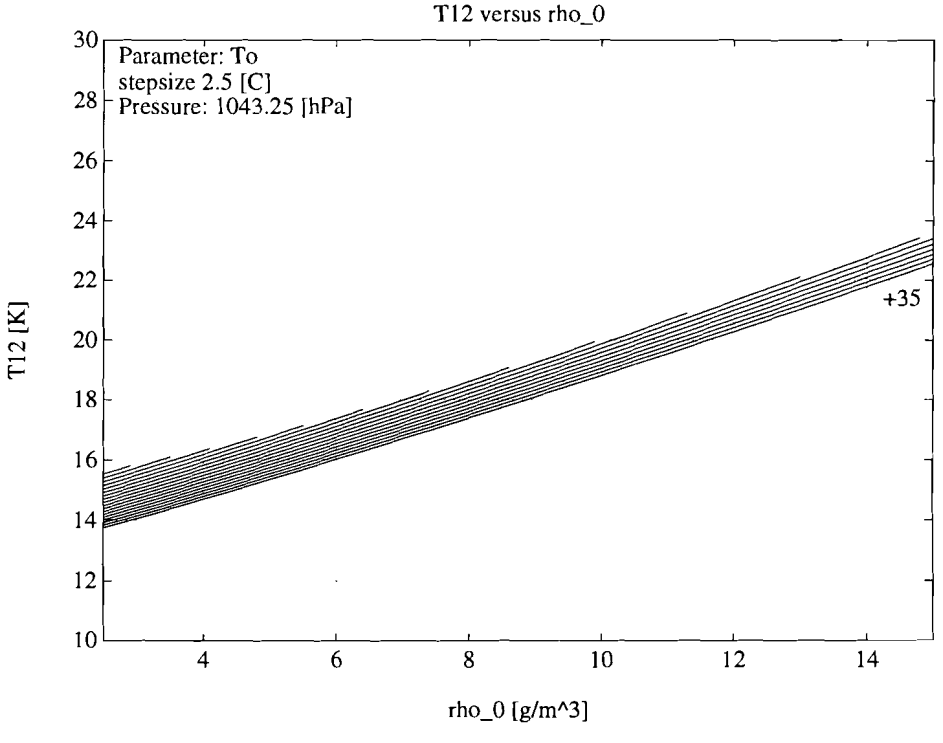
T12 versus rho_0
Parameter: To
stepsize 2.5 [C]
Pressure: 1043.25 [hPa]
+35
T12 [K]
rho_0 [g/m^3]
30
28
26
24
22
20
18
16
14
12
10
4
6
8
10
12
14

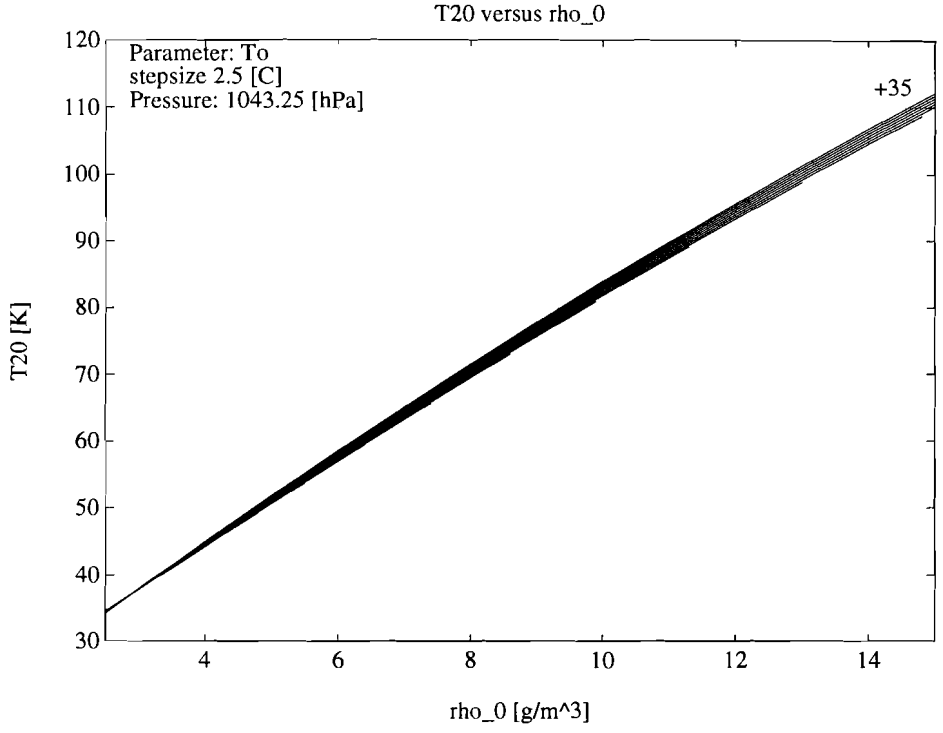
T20 versus rho_0
Parameter: To
stepsize 2.5 [C]
Pressure: 1043.25 [hPa]
+35
T20 [K]
120
110
100
90
80
70
60
50
40
30
4
6
8
10
12
14
rho_0 [g/m^3]

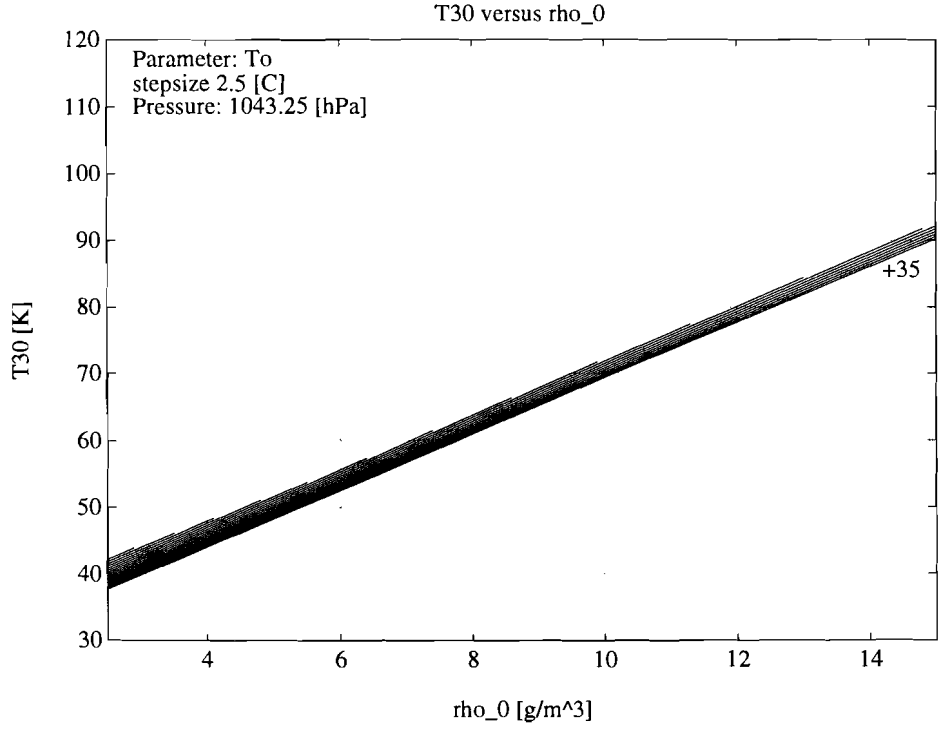
T30 versus rho_0
Parameter: To
stepsize 2.5 [C]
Pressure: 1043.25 [hPa]
+35
T30 [K]
120
110
100
90
80
70
60
50
40
30
4
6
8
10
12
14
rho_0 [g/m^3]